ABSTRACT

MEASUREMENT OF LIGHT PARTICLE-COMPLEX FRAGMENT COINCIDENCE CROSS SECTIONS

By

Bruce Earl Hasselquist

Light particle ($Z \leq 2$) inclusive and coincidence spectra have been measured for the reactions 92 MeV/A ^{40}Ar+Au and 30 MeV/A ^{12}C+Al,Au at angles from 45 to 90 degrees. Coincidence triggers for the light particle spectra were intermediate mass fragments ($3 \leq Z \leq 7$) at -30 degrees, near projectile velocity fragments ($3 \leq Z \leq 18$) at -13 degrees, and light particles ($Z \leq 2$) at -45 and -90 degrees. The Ar+Au inclusive spectra are compared to hydrodynamics and firestreak model calculations. A coalescence model calculation is used to extract coalescence radii for d,t,^{3}He, and ^{4}He from the Ar+Au spectra. Triple differential cross sections predicted by hydrodynamics are compared to the intermediate mass fragment triggered light particle spectra. A single moving source parameterization is employed throughout to depict the relevant trends in the data. Simple conservation laws are considered for the coincidence spectra in the context of a thermal moving source.

MEASUREMENT OF LIGHT PARTICLE-COMPLEX FRAGMENT COINCIDENCE CROSS SECTIONS

By

Bruce Earl Hasselquist

A DISSERTATION

Submitted to
Michigan State University
in partial fulfillment of the requirements
for the degree of

DOCTOR OF PHILOSOPHY

Department of Physics

1984

ACKNOWLEDGMENTS

I would like to thank Dr. Gary Crawley for taking me on as a graduate student and providing invaluable guidance throughout my graduate career. The freedom afforded me by Dr. Crawley made my time as a graduate student both enjoyable and profitable.

I am deeply indebted to Dr. Gary Westfall for his assistance in all aspects of this dissertation. He provided the motivation and the means for the experiments on which this dissertation is based. His assistance during the analysis of the data and his many insights into their physical meaning will always be appreciated.

I would like to recognize the staffs of the Michigan State University Cyclotron Laboratory and the Lawrence Berkeley Laboratory for their efforts at various stages of this dissertation.

The physics faculty at the University of Wisconsin - River Falls are thanked for their role in encouraging me to continue in physics. Special thanks go to Dr. Neal Prochnow who advised me in my undergraduate studies and continues to be a source of advise and encouragement for me.

I would like to thank fellow graduate students Barb Jacak and Zach Koenig for their innumerable contributions to this dissertation. Technical assistance by John Yurkon during the detector development stages is greatly appreciated.

All of my fellow graduate students are thanked for their friendship during my graduate career. Special thanks go to Joe Finck who helped me to get through prelims and both Joe and Jim Duffy who were most enjoyable officemates. Barb Jacak and Zach Koenig proved to be very special friends whose friendship and dedication will never be forgotten.

My parents, Earl and Joyce Hasselquist, and my wife's parents, Earl and Helen Woodbury, have been constant sources of support and inspiration throughout my undergraduate and graduate careers. Their many prayers on my behalf are appreciated. Above all, I would like to thank my wife, Jan, for her love and devotion over the last eight years. Her confidence in me has helped me to persevere through the hardest of trials. My son, Erik Earl, born during the first experiment at NSCL and whose second birthday coincided with my Ph. D. oral defense, is recognized for the joy which he has brought into our lives and the hope for the future which he represents.

TABLE OF CONTENTS

PAGE

APPENDIX

LIST OF TABLES

LIST OF FIGURES

CHAPTER I

INTRODUCTION

Much work has been done in the field of heavy ion nuclear physics, both experimental and theoretical. In the past decade, the interest has been concentrated in the projectile energy regimes below 20 MeV/nucleon and above 200 MeV/nucleon. As a result of studies in the lower energy regime, theories of compound nucleus production and mean field theories of the nucleus such as the Time Dependent Hartree-Fock theory (TDHF) have been developed. Theories such as hydrodynamics, cascade, and fireball/firestreak have been developed as a result of studies in the higher, relativistic energy regime. Theories developed for a particular energy regime tend to give agreement with the experimental data in that energy regime. But because of the differences in their underlying assumptions, none of them can be extrapolated into the other regime. It would seem that the projectile energy range from 20 to 200 MeV/nucleon should provide a transition region in which these disparate theories can be joined. Only recently, with the inauguration of the K500 superconducting cyclotron at NSCL and the availability of beams from the low energy beam line at Lawrence Berkeley Laboratory (LBL), has this transition region been open to experimental exploration. Other new facilities such as the GANIL national facility at Caen, France, the SARA accelerator in Grenoble, France, and the HHIRF at Oak Ridge are also beginning to produce results in this energy regime. The present study is a preliminary look at two energies in this region.

Most of the experimental work that has been done at intermediate energies with heavy ions has involved the measurement of inclusive double differential cross sections from carbon, oxygen, and argon induced reactions on Au or other heavy targets [Ab 83, Fi 84, Ja 81, Ja 83, We 82, and We 84]. Some work has also been done using more symmetric systems [Ab 83, Ja 81, and Jc 84]. In general, it has been found that, the resulting double differential cross sections for light particles with $1 \leq Z \leq 2$ and for intermediate mass fragments with $3 \leq Z \leq 10$ give indications of the existence of a thermalized region in the combined projectile-target system moving at a velocity near the velocity of the center of mass. Other reaction mechanisms are known to exist as shown, for example, by the results of projectile fragmentation experiments [Bo 83, Gu 84, Mo 81, Ra 84, Va 79, and Vi 79]. Borrel, et al. observed fragments of the projectile with $3 \leq Z \leq 16$ at laboratory angles less than 12 degrees from ^{40}Ar induced reactions on Au and Ni at 44 MeV/nucleon. The velocity distributions for these fragments were found to be gaussian in shape with centroids near the projectile velocity. The reaction mechanism is thought to be a fragmentation process whereby the projectile nucleus is excited by the target nucleus and subsequently breaks up into smaller fragments. Whether the breakup occurs almost immediately after the collision or only after a partial thermal equilibrium of the projectile is established, is a topic of current research. In order to better understand a given reaction mechanism, it is necessary to constrain the dynamics of the reaction under investigation. To this end, a number of investigators have undertaken complex coincidence measurements, each concentrating on a particular aspect of the reaction. A typical coincidence measurement is the detection of light charged particles with $Z \leq 2$ in coincidence with slow, heavy target-like fragments [Br 83, Me 80, Wa 83]. Examination of the fragment yields as a function of the light particle multiplicity indicates that the lighter fragments are associated with high multiplicity, while the heavier fragments are associated with low multiplicity. The high multiplicity events have in turn been identified as indicators of central collisions. The most ambitious coincidence experiments are the work of the "Plastic Ball" group at LBL . The "Plastic Ball" 4π detector allows detection of light charged particles with nearly a full 4π acceptance. Analysis of events based on a calculated energy flow tensor as a function of light particle multiplicity by Gustafsson, et al. [Gu 84] has given indications of what are termed non-trivial collective nuclear flow effects, namely, the bounceoff of the projectile fragments for peripheral collisions, and the side-splash of fragments from the disintegration of the projectile and target nuclei for central collisions. The reactions studied were Ca+Ca and Nb+Nb at 400 MeV/nucleon. The present work seeks to observe the dependence of the light particle spectra ($Z \leq 2$) on fragment production. Observed fragments are projectile-like fragments with $3 \leq Z \leq 18$ at forward angles and intermediate mass fragments with $3 \leq Z \leq 7$ at angles away from the projectile direction. An estimate of the direct knock out contribution to the light particle spectra, proposed for the higher energy regime,is also sought in coincidence measurements with other light particles ($Z \leq 2$).

Four models are widely accepted today-cascade, hydrodynamics, fireball/firestreak, and coalescence. These models all have their origins in the relativistic regime and have been applied in the intermediate energy regime with varying degrees of success. The cascade model [Cu 81, Cu 82, Ki 84, Kr 84, Ya 79] assumes that high energy heavy ion collisions proceed via individual nucleon-nucleon collisions within the overlap zone of the two nuclei. The nucleons follow straight-line trajectories between collisions. As the collisions continue, particles whose energy exceeds the binding energy are considered to be emitted, until a minimum collisional density is achieved or until a predetermined collision time is reached. Effects due to the Pauli principle and pion production have more recently been included [Ki 84, Kr 84]. A cascade calculation was unavailable for inclusion in this work. Most applications of the cascade model have been restricted to energies above 400 MeV/nucleon. Comparisons of the early cascade models with experimental data at these relativistic energies [Bc 84, Gu 84, St 68, St 82] show that the cascade model fails to reproduce the trends in the 400 MeV/A Nb+Nb data of Gustafsson, et al. [Gu 84]. A more recent cascade calculation by Kitazoe et al. [Ki 84], has had more success in describing the Nb+Nb data by including the effects due to Pauli blocking and pion production. It remains to be seen whether or not the cascade formulation can be successfully extended down into the intermediate energy region.

The hydrodynamic or nuclear fluid dynamic model [Bu 81, Bc 84, St 68, St 79, St 80, St 81, St 82, St 83] requires the assumption of a short mean free path relative to the size of the interaction region. This is in contrast to the necessary assumption of a long mean free path used in the cascade model. For peripheral collisions involving only a few interacting nucleons, the mean free path is likely to be long. Since inclusive measurements contain contributions from all impact parameters, it is likely that inclusive measurements are not a good test of hydrodynamics. Although hydrodynamics predicts regions of extreme temperature and density during the reaction, at later times in the reaction the density becomes so small that the nucleons rarely collide. At this point hydrodynamics no longer applies because of the requirement of a short mean free path and an evaporative model is employed in order to give cross sections directly comparable to experiment. Comparisons with the recently obtained results of Gustafsson et al. [Bc 84, Gu 84] show that hydrodynamics is capable of reproducing the trends in the high multiplicity selected Nb+Nb data at 400 MeV/A. A hydrodynamic calculation was available for this work and will be compared with the data for both inclusive and central impact parameter selected events.

The nuclear fireball model has been compared with heavy ion reaction data at relativistic energies greater than 200 MeV/nucleon [Go 77, Go 78, We 76, My 78] and also with data from ^{20}Ne induced reactions on Au at 100 and 150 MeV/nucleon [We 82]. The fireball model assumes that a highly excited interaction region is created by the projectile sweeping out the portion of the target which is in the overlap region of the two nuclei. This region, called the fireball or participant zone, moves forward in the laboratory frame with a velocity near half the projectile velocity. The fireball is treated as an equilibrated nonrotating ideal gas of nucleons characterized by a temperature. The fireball then expands isotropically in its center of mass frame with a Maxwellian distribution in energy. The laboratory distributions are obtained by transforming the fireball frame momentum distributions relativistically. The model incorporates the specific geometry for the colliding nuclei, the binding energy of the nucleons in the fireball, and composite particle production.

Of more importance for extreme relativistic collisions, the model also considers the creation of baryonic resonances in order to obtain a more accurate estimate of the temperature from the available energy in the center of mass of the fireball. The firestreak model is an extension of the fireball model, in which it is now assumed that chemical equilibrium is reached between the various hadronic species. This is described by a chemical potential. A critical "freeze out" density is introduced, below which the fragment momentum distributions no longer change. The other modification to the fireball is the use of a nuclear density distribution with a diffuse surface. The use of a diffuse surface leads to a temperature gradient across the participant zone according to the relative amounts of material coming from the target and the projectile. The firestreak has had its greatest success at energies above 1 GeV/nucleon [Go 78], although it seems to agree with the data at least as well as the fireball at energies down to 100 MeV/nucleon [We 82]. A firestreak calculation was available for the inclusive light particle spectra from 92 MeV/nucleon ^{40}Ar+Au and will be presented in Chapter V.

The models which have been discussed so far have all incorporated aspects of the dynamics of the collision process in heavy ion reactions to calculate proton cross sections as well as composite particle cross sections. The coalescence model [Aw 80, Gu 76, Le 79, Sa 81] uses a primary nucleon distribution, usually the experimental inclusive proton spectra, to determine the cross sections for composite fragments in the reaction. The model assumes that if a subset of the primary distribution of nucleons corresponding to a bound nucleus is localized in a region of phase space with a radius less than a "coalescence radius", the subset will coalesce and form a nucleus. The cross section in momentum space for the emission of a composite with A nucleons is then related to the Ath power of the single nucleon cross section at the same momentum per nucleon. A single free parameter, the coalescence radius, is used in the calculation of the composite cross section. The coalescence radius has been determined for a number of systems over a large range of projectile energies by fitting measured composite cross sections with spectra calculated from the measured proton cross sections [Ab 83, Aw 80, Aw 81, Go 78, Le 79, Sa 81]. In general, this radius is constant in magnitude from 20 MeV/nucleon to over 2000 MeV/nucleon. A coalescence model fit has been done for the Ar+Au reaction of the present work and coalescence radii have been extracted for d, t, ^{3}He, and ^{4}He. A more detailed discussion of the actual coalescence calculation performed will be presented in Chapter V.

Of the four models discussed, hydrodynamics and the fireball/firestreak models require the assumption of short mean free paths for the interacting nucleons. They also require the thermalization of at least a localized region of the interaction zone. The cascade model requires the assumption of long mean free paths compared to the length of the nuclear interaction. The nucleons are assumed to undergo only two body interactions. The coalescence model makes no assumptions as to the dynamics of the collision, but instead, uses a primary nucleon distribution to predict the cross sections of the heavier composite particles. All of these models have been shown to work at incident energies above 200 MeV/nucleon. Only the coalescence model has been shown to work at energies much below 100 MeV/nucleon.

Theoretical models developed for the energy regime below 20 MeV/nucleon have not been successfully extended up into the intermediate energy regime. Attempts to apply TDHF theory at energies of 30 and 85 MeV/nucleon [St 81, So 80] have shown that TDHF predicts too great a transparency for the colliding nuclei. Calculations directly comparable to experimental data could not be found in the literature for TDHF. Further discussions of these models, as well as a wealth of references to the literature, can be found in the excellent review articles of Scott and Boal [Sc 79, Sc 81, Bo 84].

Results from two experiments will be presented in this thesis. In the first, the ^{40}Ar+Au reaction was studied at 92 MeV/nucleon. Various inclusive or "singles" and coincidence measurements were made. Light particle, $Z \leq 2$, inclusive spectra were measured at angles from 45 to 90 degrees in the laboratory. Energy spectra were also measured for light particles ($Z \leq 2$) in coincidence with intermediate mass fragments with $3 \leq Z \leq 7$ at -30 degrees in the laboratory (180 degrees in azithmuth from the light particles) and with projectile velocity fragments with $3 \leq Z \leq 18$ at -13 degrees. Energy spectra were also measured for light particles in coincidence with other light particles at -90 degrees.

In the second experiment carried out using the K-500 cyclotron at the National Superconducting Cyclotron Laboratory, a 30 MeV/nucleon ^{12}C beam was used to bombard targets of Al and Au. Light particle inclusive spectra were measured at a number of angles from 45 to 90 degrees in the laboratory. Light particle coincidence spectra were measured for the intermediate mass fragment ($3 \leq Z \leq 6$), projectile velocity fragment ($3 \leq Z \leq 6$), and light particle triggers at -25, -13, and -45 degrees respectively.

The thesis is organized as follows. Chapter II deals with the development of the plastic scintillator array and multi-wire counter that were used in the two experiments. The setup of the experiments is presented in Chapter III. Chapter IV outlines some of the specifics of the data analysis performed. In particular, the methods used to make the corrections to the light particle spectra for reaction losses and scattering out of the detectors will be given. The data, along with a discussion of the observable trends will be presented in Chapter V. Fits to the available models will be shown and discussed. A summary of the findings of this thesis will be given in Chapter VI along with some possible avenues of future research. The

Appendix contains a detailed description of the momentum conservation calculation which is used for most of the coincidence data.

CHAPTER II

DETECTOR DEVELOPMENT

In order to accomplish the goals set forth in Chapter I, it was necessary to undertake the development of a detector array capable of detection of high multiplicity light particle events. The design of this detection system can be separated into two separate subsystems; an array of light particle telescopes capable of determining the energy and identity of light isotopes (p, d, t, ^{3}He, and ^{4}He), and a multiwire proportional counter capable of providing more precise position information on these same light isotopes positioned in front of the telescope array. We will discuss the telescope array first.

A. Telescope Array

The design of the telescope array is in many respects similar to the design employed by the Plastic Ball group at Lawrence Berkeley Laboratory [Ma 80, Ba 82]. There are, however, several aspects of our design that warrant its discussion here. The array consists of seven NE102 [Nu 80] plastic scintillator - CaF_2 "Phoswich" telescopes each of which uses a single photomultiplier tube to collect both the plastic scintillator and the CaF_2 signals. The two signals are distinguished by means of their extremely different decay times. The decay time for plastic scintillator is less than 10 nsec compared to 1 μsec for the CaF_2. Integration of the photomultiplier output in a charge integrating ADC for the first 80 nsec gives most of the plastic scintillator signal. A separate integration in another charge integrating ADC over a period of 2 μsec delayed by 240 nsec relative to the beginning of the first integration gives the CaF_2 signal (Figure II-1). There is a certain amount of each signal which is either lost or contained within the wrong integration due to the overlap of the two signals. This is, however, a fairly small effect in most instances and can be corrected offline. Discussion of the corrections will be deferred to Chapter IV.

In our design the plastic scintillator is 17 cm thick and functions as the stopping detector thus giving the E information. The CaF_2 is 2 mm thick and functions as the energy loss detector thus giving the ΔE information and enabling particle identification (Figure II-2) to be carried out. The telescopes were designed to close pack in a spherical geometry as six tapered hexagonal shaped detectors surrounding a seventh tapered hexagonal shaped detector. The design is in fact not correct for a 4π geometry in that a perfect design would be based on a truncated icosahedron, ie. a pentagonal detector surrounded by five hexagonal detectors. The discrepancies in the geometry at this scale were however outweighed by the advantages of having

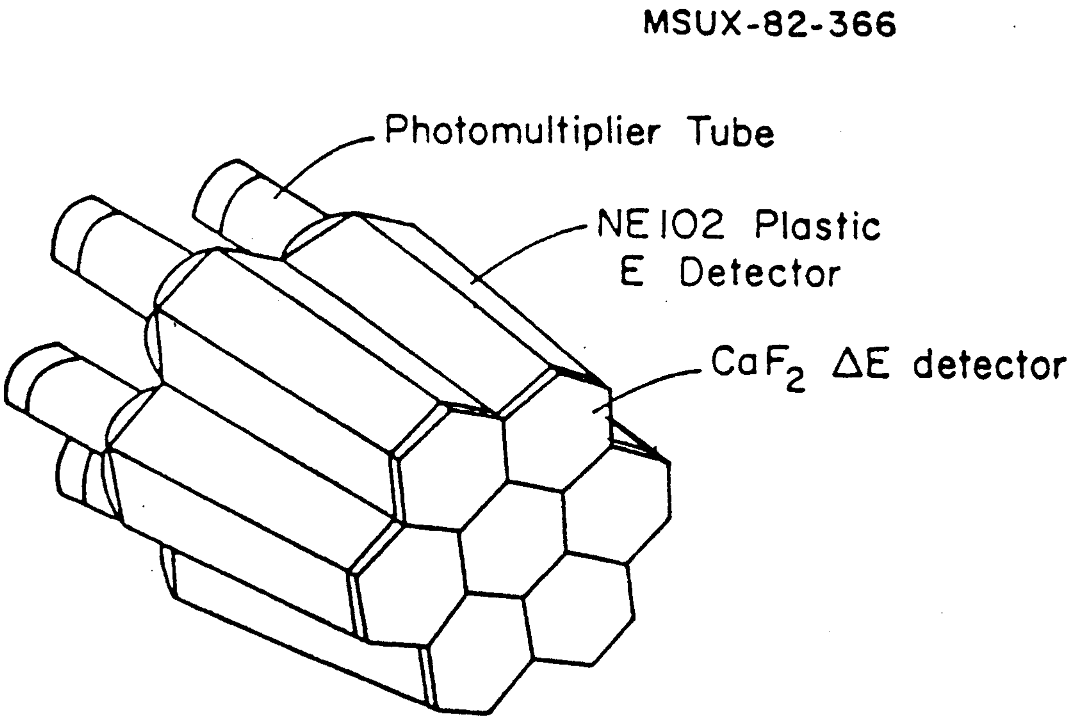

Figure II-1. Seven telescope scintillator array used at LBL and NSCL

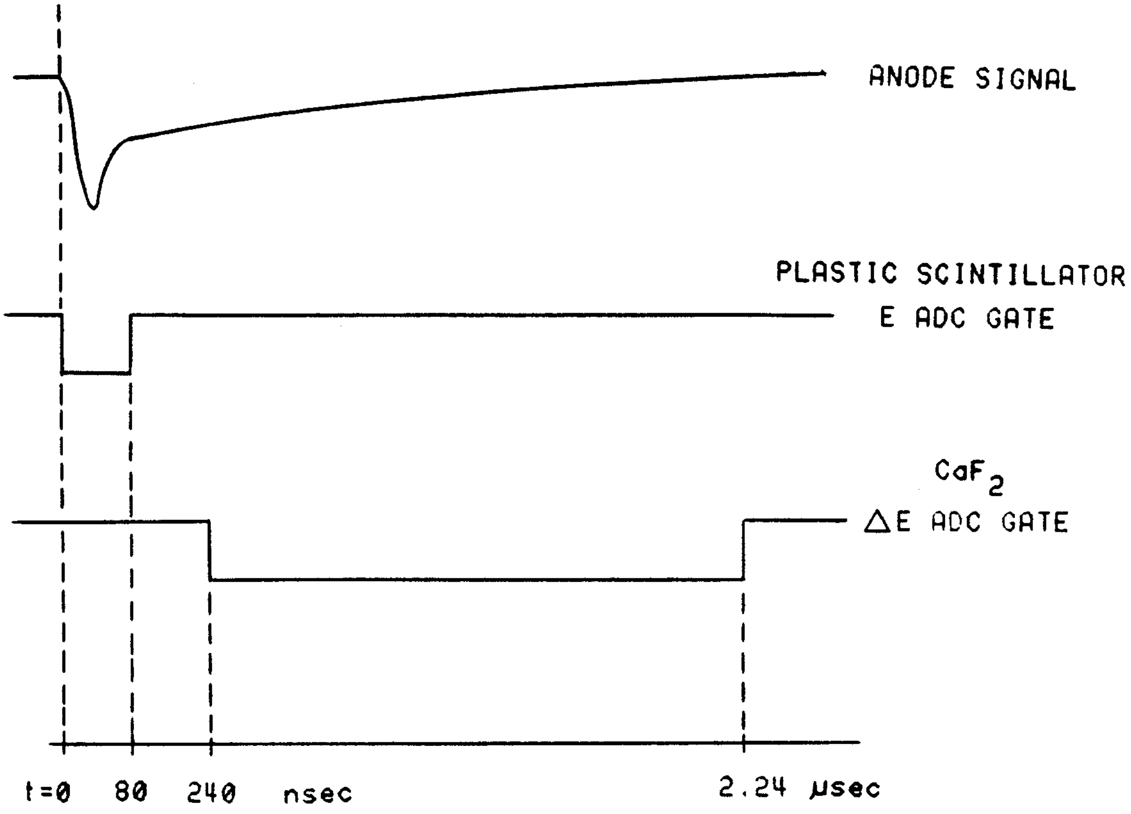

Figure II-2. Timing diagram for scintillator array telescopes. The anode signal is a sum of the fast plastic scintillator component and the slow CaF_2 component.

identical solid angles for the seven telescopes and a single geometry to machine.

Due to the low melting point of the plastic scintillator and its tendency to craze near regions exposed to high temperatures, care had to be taken in its machining and polishing. The finish cuts on the plastic were done with a fly cutter running at ≈ 1000 RPM, removing ≈ 10 mils of material per cut. The cutter was cooled using a continuous flow of a water soluble oil. The plastic scintillator was then sanded with #600 grade silicon carbide waterproof polishing paper immersed in water and finally polished with optical polishing alumina (particle size below 9 μm) slightly moistened with water on a cotton cloth. This procedure produced a highly polished surface on the plastic with no noticeable machining marks and no evidence of crazing. A clear lucite lightpipe was also machined to match the plastic scintillator to the photomultiplier tube.

In order to achieve optimum light collection efficiency and resolution, the plastic scintillator was painted with a TiO_2 water based reflective paint [Bi 67]. In addition, the light guide was also painted with TiO_2 paint but in a striped pattern loosely based on a Monte Carlo simulation of light collection efficiency and resolution by Schölermann and Klein [Kl 79, Sc 80]. This was predicted to give better energy resolution by more uniformly distributing the emitted light over the surface of the photomultiplier photocathode.

The photomultiplier tube used for the telescope array was an EMI model 9872, 3.81 cm diameter, 10 stage compact focused tube with beryllium copper secondary emitting dynode surfaces [Em 79]. The tube was chosen based on its compact size, a fast response time of 2.2 nsec risetime comparable to the 2.4 nsec decay time of the plastic scintillator, and its relatively low cost. The base containing the divider chains for the photomultiplier tube was an EMI active base design (Figure II-3) which incorporated high voltage transistors in the last four stages of the divider chain to maintain a constant voltage drop during periods of high count rate. The design also current limited above a certain maximum current to prevent destruction of the photomultiplier tube should the tube be exposed to excessive light accidentally [Hi 77, Ke 77].

The light particle telescope was completed by the addition of the CaF_2 element which was machined from a 5.1 cm diameter by 2 mm thick disk of CaF_2(Eu) using a 1/16 inch wide diamond wheel on a vertical grinder with a constant spray of water soluble coolant directed onto the material. The mounting procedure for the CaF_2 was similar to a procedure used in mounting Si wafers to be cut for solid state detectors using a wax substrate between the material and an aluminum mount. This procedure worked well and produced only one partially fractured crystal out of eight which were cut. It should be noted, however, that for crystals 12.5 cm in diameter, this procedure does not

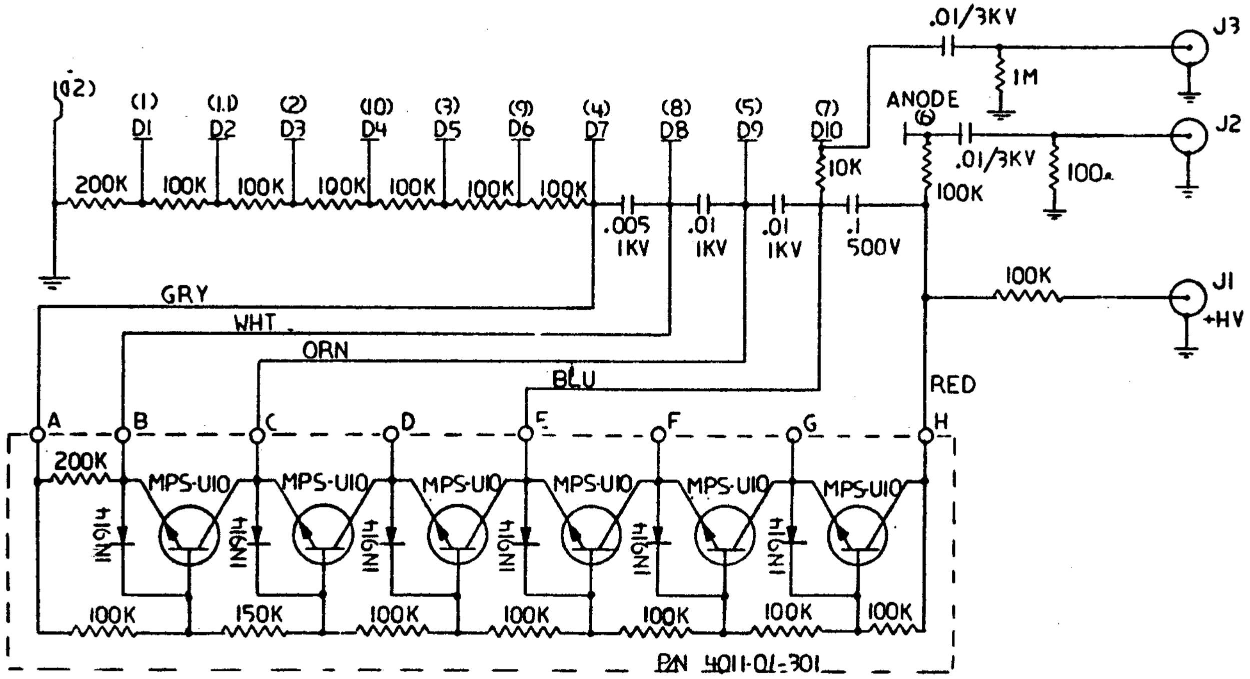

Figure II-3. Schematic for active PMT base design used with scintillator array telescopes [Em 79].

produce satisfactory results as the material tends to fracture severely.

The entire assembly of CaF_2, plastic scintillator, light guide, and photomultiplier tube was joined with a thin layer of optical epoxy at each interface and wrapped in a layer of aluminum foil to prevent light leakage into the detector. The entrance window to the detector was a 13 μm aluminum foil.

B. Plastic Scintillator Energy Calibration at IUCF

Before the CaF_2 elements were ready, six of the seven plastic elements were taken to IUCF to be calibrated for proton energy response from Ep=15 Mev to 120 Mev [Ha 82]. Protons of various energies were selected by the angular positioning of the detectors in the chamber and the use of the elastic scattering of 148.9 MeV protons from a 20 mg/cm^2 CH_2 target. A simple coincidence between the scattered proton and its recoil ^1H target provided a clean spectrum in the detectors (data in two detectors at a time). Because of the large $dE/d\theta$ a slit was fixed to the front of each detector. The slit was 0.25 cm x 1.27 cm slot in the center of a 0.890 cm thick copper disk. This gave an angular opening of 0.41°. The copper disk was sufficiently thick to stop up to ≈80 Mev protons. The coincidence spectrum, shown in Figure II-4, consisted of a peak for protons which passed through the slit and also a lower energy peak for protons which were degraded by penetration of the copper disk. The

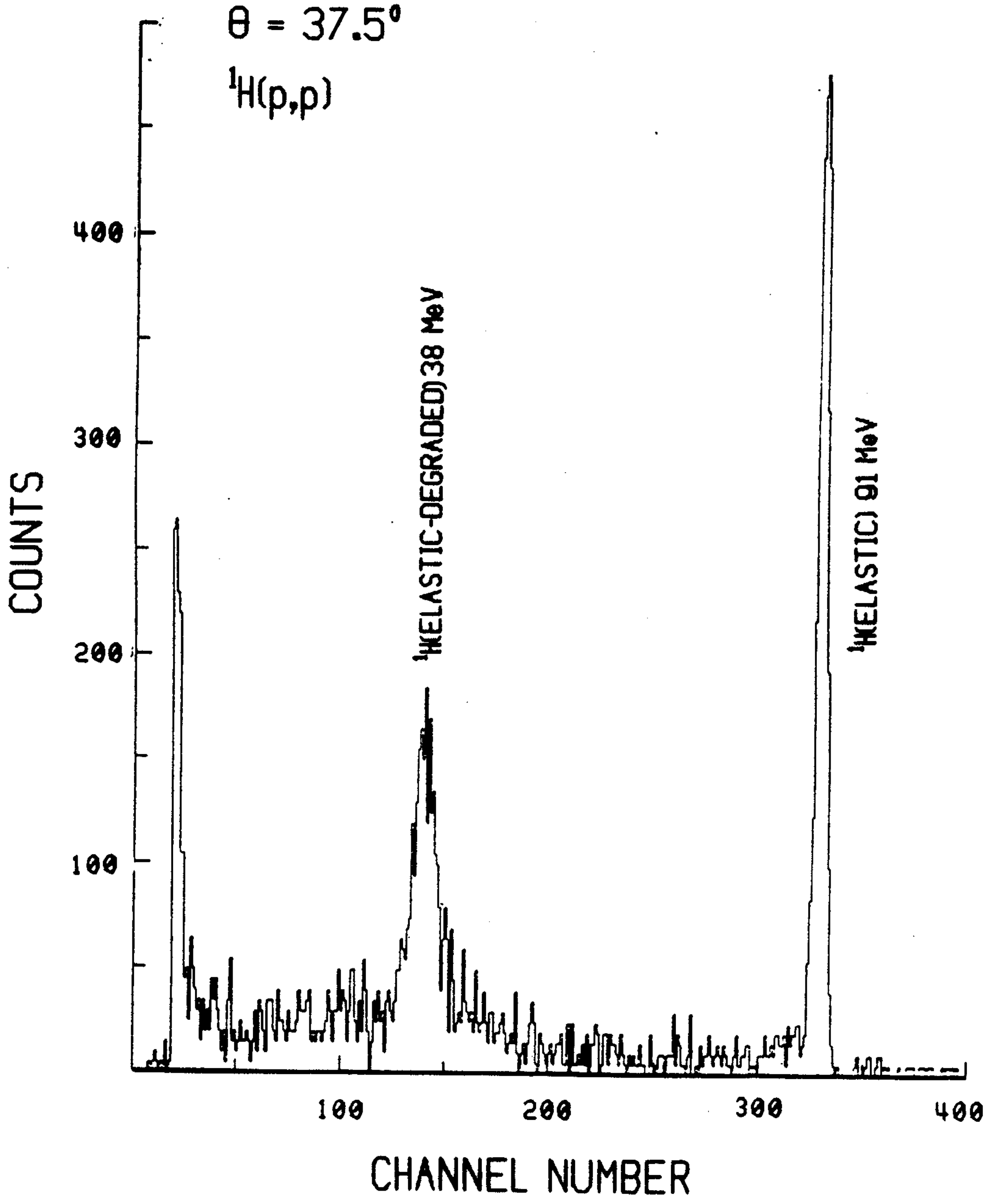

Figure II-4. Coincidence p-p spectrum from CH_2 target during IUCF plastic scintillator calibration.

proton beam energy of Ep=148.9 Mev was too low to allow both the incident and the recoil proton to penetrate the copper disks in front of the detectors. The energy of a proton penetrating the copper disk was determined from its energy loss in the disk using an initial energy given by kinematics and the angular position of the slit through which its coincident proton passed.

Singles data was also taken using the CH_2 target (Figure II-5). Peaks were found for the ^{12}C elastic and first (4.44 MeV) and third (9.64 MeV) excited states [Aj 75] for protons which were degraded by penetration of the copper disk. Protons passing through the slit did not appear in the spectrum because the amplifier gains were set too high. Elastic peaks for protons scattered from a Au target and from deuterium in the CH_2 target were also seen. Again, only the peaks for the scattered protons which were degraded in the copper disk appeared in the spectrum.

The detector angles were checked by comparing the position of a dip in the degraded singles p-p elastic scattering peak at angles of ± 30 degrees (Figure II-5). The dip was caused by the removal from the degraded peak of the elastically scattered protons which passed undegraded through the slit opening. The large magnitude of $dE/d\theta$ for p-p scattering gave a large spread of energies across the 7 degree width of the detector. This spread in energies, which can be seen in the large width of the dominant peak in Figure II-5, combined with the relatively small spread

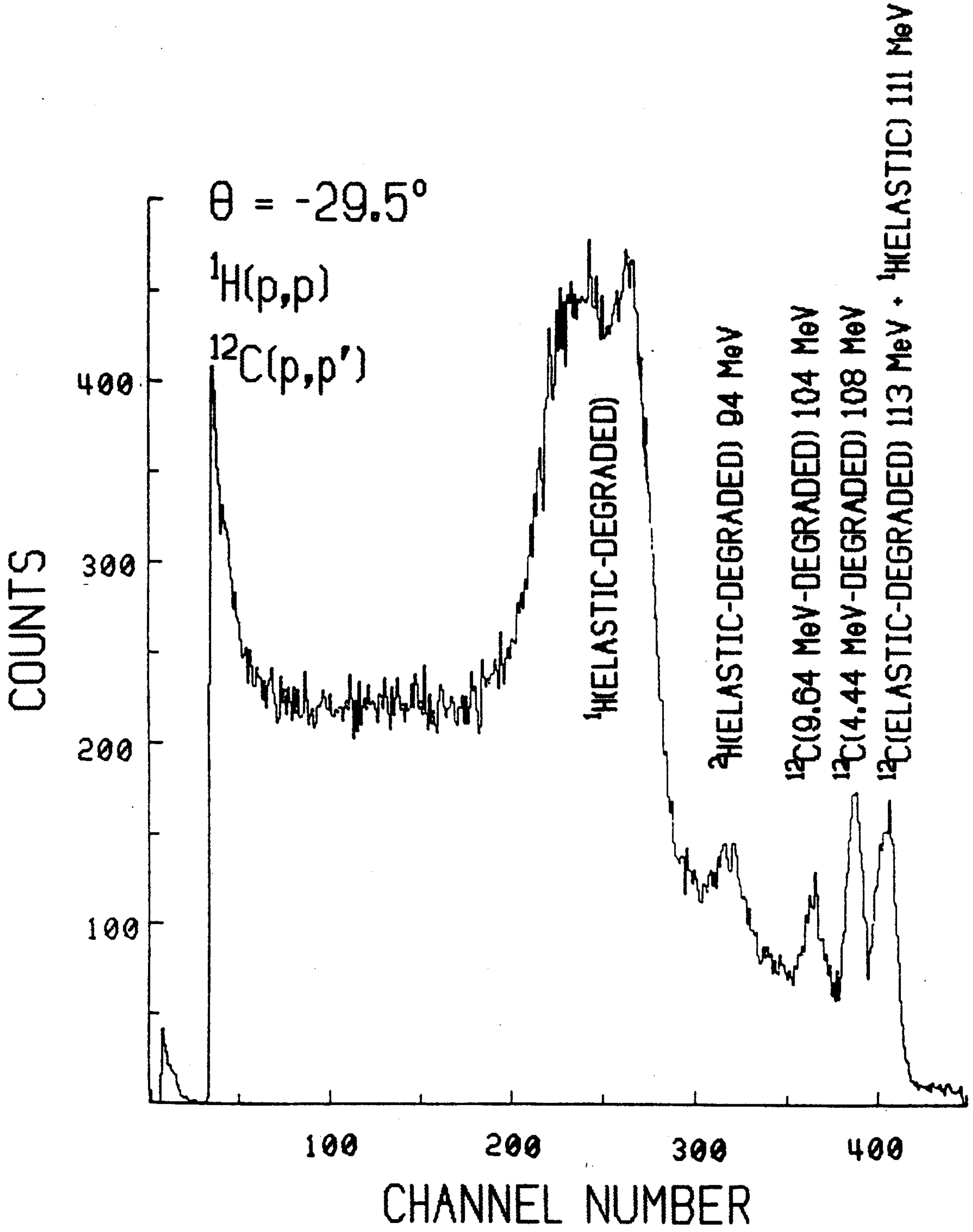

Figure II-5. Singles proton spectrum from CH_2 target during IUCF plastic scintillator calibration.

across the slit opening gave a well defined minimum in the spectra. From this it was found that there was a misalignment of the zero angle of 1.28 degrees. The misalignment was verified by the observation that opposite curvatures of the calibrations for detectors on the two mounting arms in the chamber were eliminated when the correction of 1.28 degrees was applied.

Four of the six detectors calibrated at IUCF were found to have essentially the same calibration, the slopes being very nearly linear and the intercepts being close to zero. A representative calibration curve is shown in Figure II-6. A fifth detector experienced a gain shift throughout the calibration, which was later found to be due to the separation of the phototube from the lightguide. The sixth detector had a somewhat different slope but about the same intercept as the other detectors indicating a different gain characteristic of the base.

The resolution of the plastic scintillator detector was also determined during the IUCF calibration run. The intrinsic resolution of the detector was unfolded from the fwhm of the coincident calibration peaks and the effect of $dE/d\theta$ on the proton energy across the slit opening. The effects of energy straggling for coincident protons which penetrated the Cu slit material and the 13 μm Al foil entrance window, the finite beam spot size, and straggling in the CH_2 target were not taken into account. These are relatively small contributions to the overall resolution and

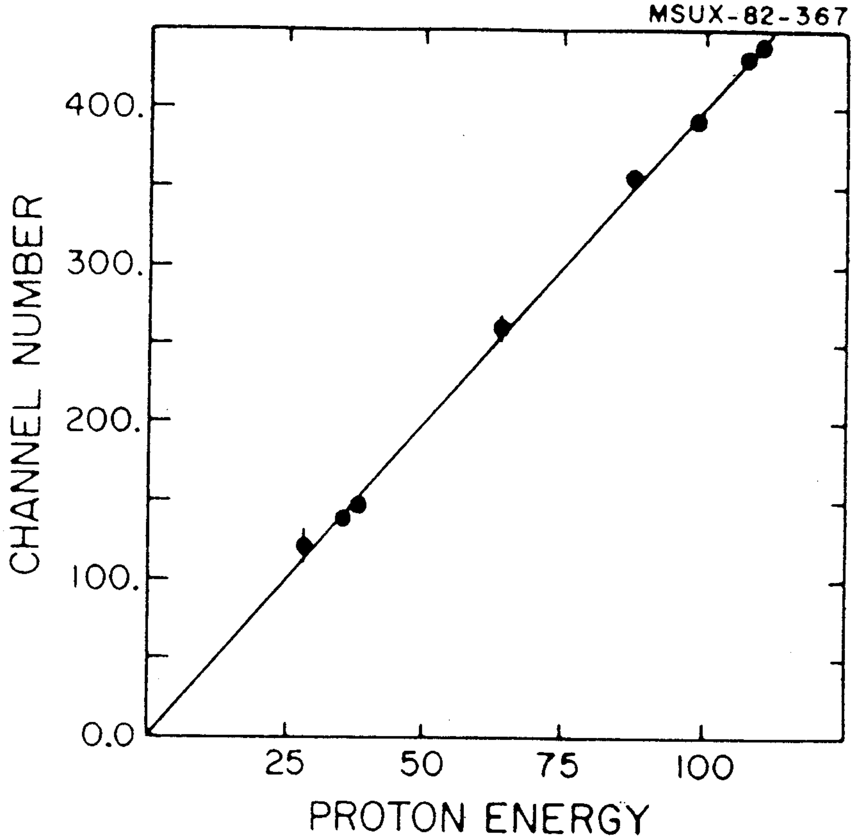

Figure II-6. Proton energy calibration of a plastic scintillator detector from IUCF calibration. The line is a least squares fit.

would only serve to slightly decrease the calculated intrinsic resolution. The calculated intrinsic resolution for five of the plastic scintillator detectors is shown in Figure II-7 along with a plot of the root inverse range in the plastic as a function of the particle energy. The curve has been arbitrarily normalized to 2 percent at 100 MeV. The resolution is seen to vary smoothly from greater than 10 percent below 20 MeV to approximately 2 percent above 100 MeV. From the statistics of photon counting and the range energy relationship, the intrinsic detector resolution should be proportional to $(\mathrm{Range})^{-.25}$. This can be considered as a lower limit to the resolution. The departure from the lower limit at low energies is seen as an indication of less efficient light collection for particles which stop farthest from the photomultiplier tube.

The proton beam energy at IUCF was determined from the beam optics and an NMR reading and is estimated to be correct to better than 1%.

C. CaF_2 Thickness

The choice of thickness for the CaF_2 element of the light particle telescope was based on a calculation of the energy loss in the two elements of the telescope. Figure II-8 shows the calculation for a CaF_2 thickness of 2 mm. Assuming that the resolution obtainable with the combined elements of the telescope would not be much different from that obtained in the IUCF calibration run for the plastic

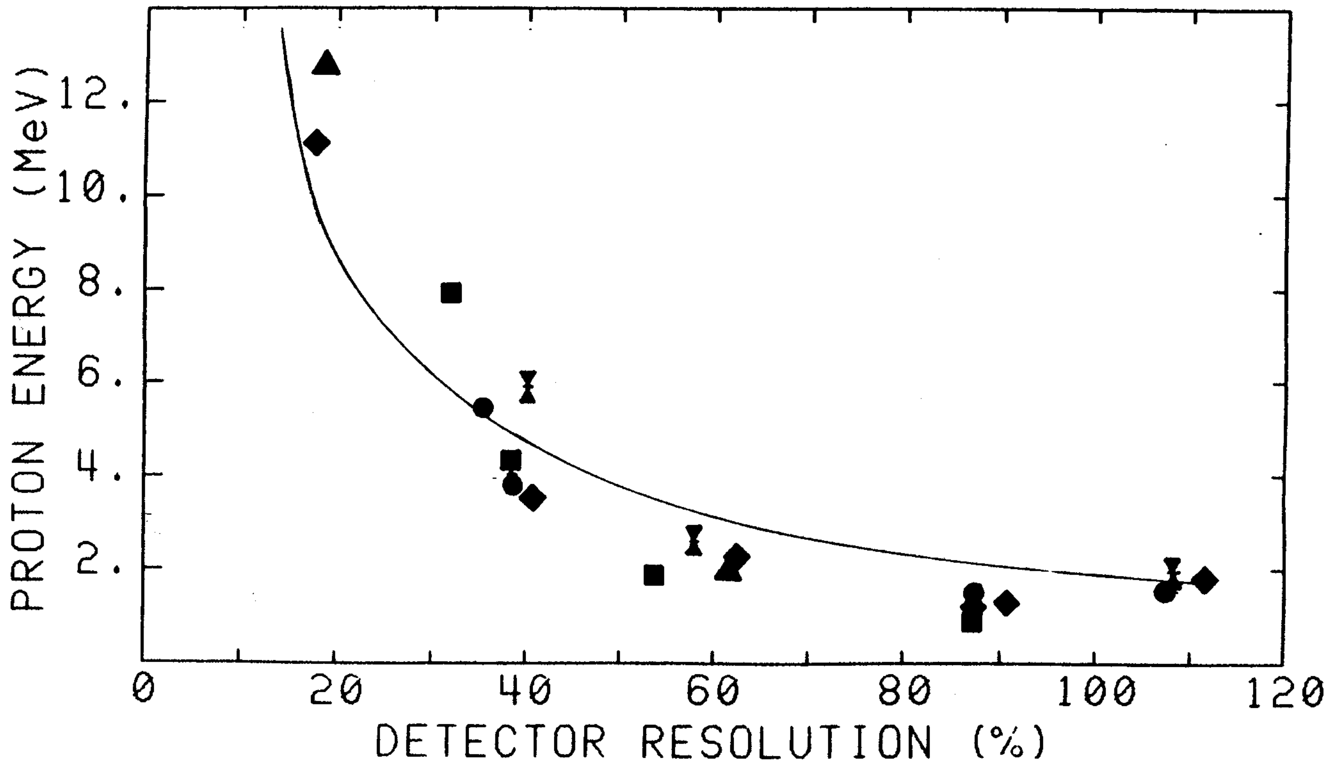

Figure II-7. Plastic scintillator resolution in percent for protons from IUCF calibration. The solid curve is the inverse of the square root of the proton range normalized to 2 percent at 100 MeV.

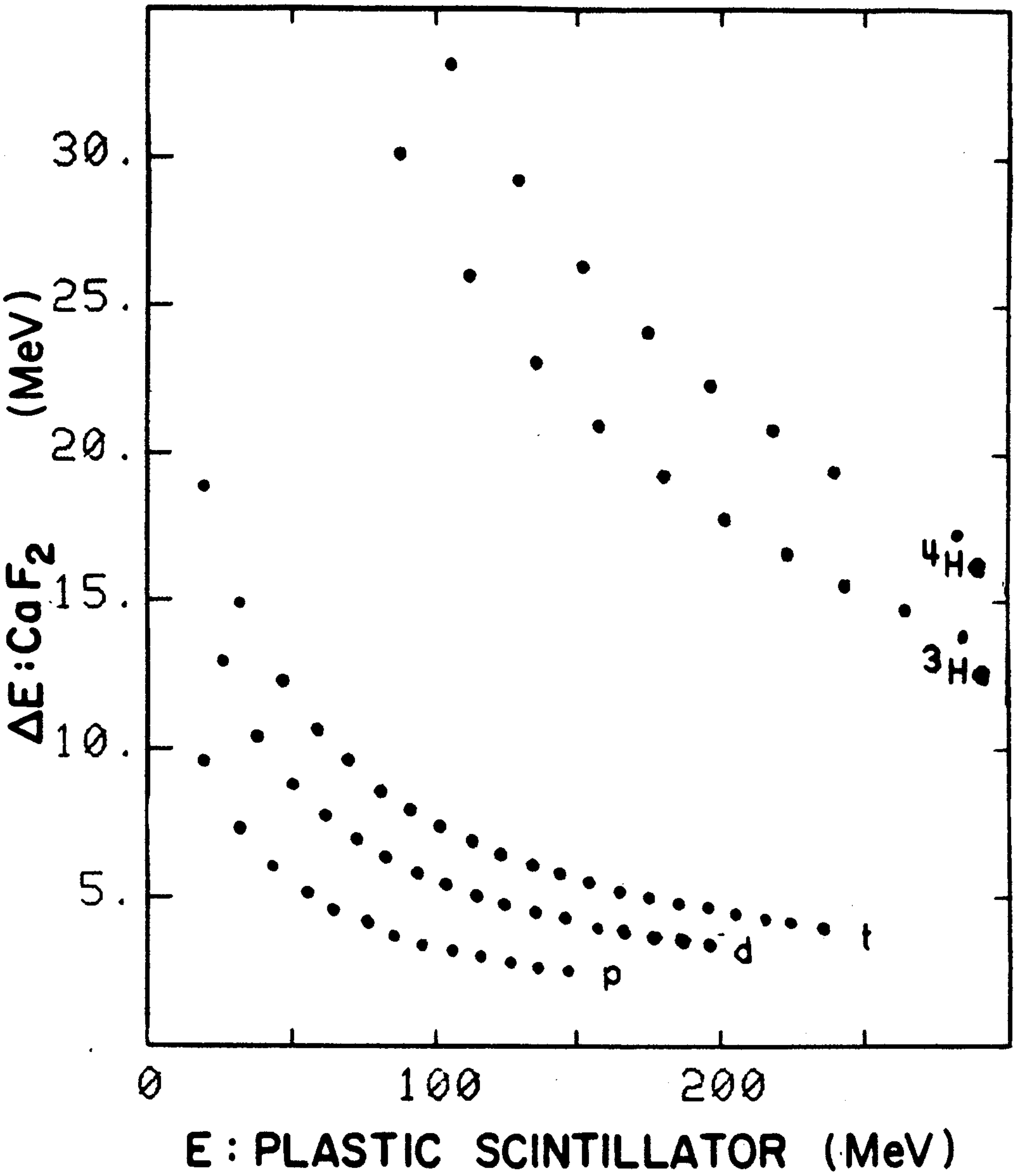

Figure II-8. Calculated ΔE-E isotope separation for p, d, t, ^{3}He, and ^{4}He for a CaF_2 ΔE thickness of 2 mm.

scintillator, it was apparent that a 2 mm thickness would give both sufficient energy loss and isotope separation for the range of particles and energies anticipated. Another important consideration was the low energy cutoff imposed by the relatively thick CaF_2 front element. Calculated cutoffs are given in Table II-1 for the hydrogen and helium isotopes for CaF_2 thickness of 2, 3, and 4 mm. The cutoffs imposed by the 2 mm thickness were considered to be sufficiently low for the beam energies at MSU and quite sufficient for LBL Low Energy Beam Line energies.

D. Multiwire Proportional Chamber

Small angle light particle correlations have been shown to yield information about the size of the emitting system in nucleus-nucleus collisions [Ly 83, Gu 84]. In order to extract this information one needs to be able to determine the relative momenta of two coincident light particles to better than ≈ 2 MeV/c. For two protons of 50 MeV this translates into an angle resolution of the order of 1 degree. One way to achieve this level of spatial resolution is through the use of a Multiwire Proportional Chamber or MWPC [Ch 70]. The principal behind the operation of an MWPC is that the electrons liberated by ions traversing the chamber drift (typically 20-40 nsec/mm) to the positively charged anode wire. Close to the wire (within a few diameters), the electric field is very strong. Here the electrons experience inelastic ionizing collisions, giving rise to a multiplicative avalanche. The positive ions produced in the avalanche drift toward the cathodes. An important point is that the pulses detected on the anode are mainly produced by the motion of positive ions. Negative signals are induced on the central anode wire while positive signals appear on the adjacent anode wires.

In this design [Ti 81, Ti 82], the MWPC contains 3 anode planes, two of which provide horizontal and vertical position information, while the third plane is positioned at 45° with respect to the first two planes and is used to resolve the position ambiguity which arises when several ions traverse the chamber simultaneously. The sensitive area of the detector is 15.5 cm x 15.5 cm, the anode-cathode spacing is 6 mm, and the anode wire spacing is 2.54 mm. Each anode plane consists of 64 sense wires (gold plated tungsten with a diameter of 20 μm) which are paired electrically into 32 channels giving an angular resolution of 0.8° when the detector is 35 cm from the target. This resolution satisfies the requirement imposed by the small angle correlation measurement. To reduce the material thickness of the detector, some of the cathodes are common to two anodes. The design consists of three contiguous cells having a total of four cathode planes made of sheets of 6.4 μm aluminized mylar (both sides aluminized) and the three anodes giving a material thickness of 10 mg/cm². The resulting signals from each pair of anode wires are processed using an electronic Proportional Chamber

TABLE II-1

CALCIUM FLUORIDE PUNCH THROUGH ENERGIES (MeV/n)

THICKNESS	2 mm	3 mm	4 mm
Proton	21.5	27.0	31.5
Deuteron	14.5	18.2	21.4
Triton	11.5	14.5	17.1
^{3}Helium	25.2	31.5	37.0
^{4}Helium	21.5	27.0	31.5

Operating System (PCOS III) developed by LeCroy [Le 81]. LeCroy 2735 16 channel integrated circuit boards placed directly on the anode wire plane board first amplify the anode signals from each plane using four quad amplifier chips, one for each set of four wires. Each set of four amplifier outputs is then passed through a quad discriminator chip and then bussed out of the detector to a slave CAMAC crate containing LeCroy 2731 Delay and Latch modules each capable of processing up to 32 channels or one entire MWPC plane. The information in the latches is controlled via the backplane of the CAMAC crate by a LeCroy 2738 MWPC Digital Readout Controller. The controller is strobed with a valid event gate and read via a single 50 conductor ribbon cable by a LeCroy 4299 Databus Interface. The interface resides in a CAMAC crate which is under the control of the data acquisition routine. Only "hit" information is available from this system. Linear (proportional) signals are not provided. This is not a limitation, however, since there is insufficient energy loss in the detector to obtain a good energy signal for light particles. The energy information is obtained from the telescope array which is behind the MWPC.

Operating conditions for the MWPC were determined to be a gas mixture of Argon-Ethane (50%) at 500 Torr and a cathode high voltage of -3000 volts. Early bench tests of the MWPC system using a ^{106}Ru β- source with an endpoint energy of 3.54 MeV revealed that the detector was extremely sensitive to RF noise. The detector vacuum box was therefore designed to provide adequate RF shielding as well as good ground plane connections between the enclosed amplifier-discriminator cards and the vacuum box. In addition, the entrance and exit windows of the detector were required to withstand an internal/external pressure differential of 500 Torr when the detector was placed in the vacuum chamber. This necessitated the development of a wire mesh (0.6 mm dia. piano wire) which held a 75 μm Kapton window in place. The spacing of the crossed wire wire mesh was approximately 1.5 cm and was pressure tested up to a pressure differential of 760 Torr without failure.

Tests of the completed MWPC with the β- source show that single wire resolution is achievable and that the efficiency of the detector is reasonable, although highly dependent on the threshold settings of the amplifier-discriminator cards. Figure II-9 shows a representative test of the MWPC using the ^{106}Ru β- source with a small (approximately one wire pair wide) start scintillator behind the detector. The chamber was operated at an atmosphere of Ar-Ethane (50%) with Vcath=2.7 kv. Note that the source was placed in five different locations along the center of both the X and Y planes. The source was left in each position for varying amounts of time. Figures II-9;a,b,c show the projecions of each wire plane for the different source positions. Figure II-9;d is a two dimensional plot of coincidences between the X and Y planes of the detector with

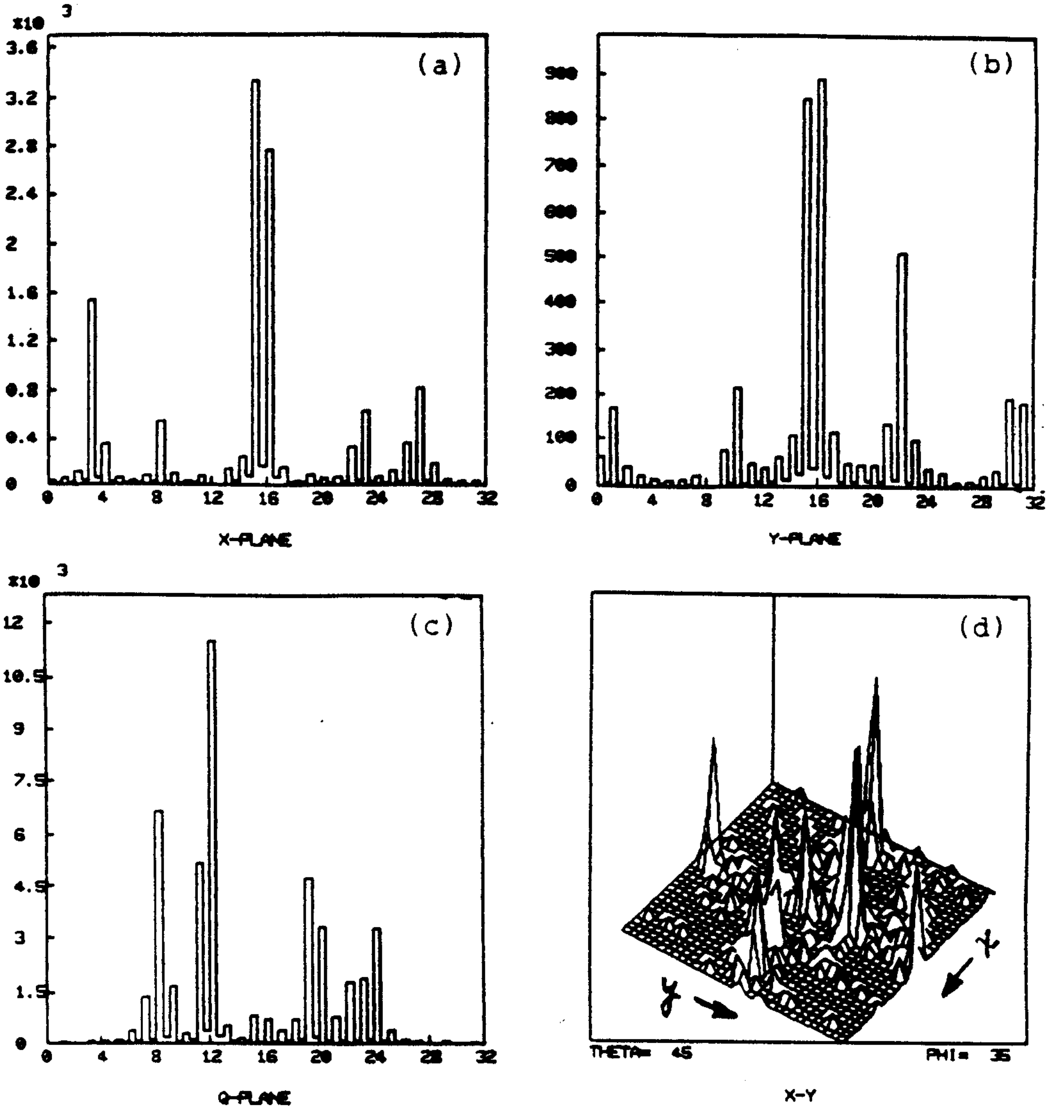

Figure II-9. MWPC position resolution obtained with a β-source placed at 5 locations along the center of both the X and Y planes.

the additional requirement that only one wire fired in each of the two planes. Overall, the position resolution of the detector is quite good, especially considering the amount of angle scattering for an electron in an atmosphere of Ar-Ethane.

The MWPC was used in two experiments, one at Lawrence Berkeley Laboratories, and the other at NSCL. During the former experiment, the MWPC functioned properly during the setup runs and for the first few minutes of the first data run, however, a sudden increase in the beam intensity caused the MWPC to arc internally. Attempts to restore the cathode voltage caused further arcing before a useful working voltage could be reached. Later examination of the anode and cathode planes revealed no obvious cause for the arcing. It has been assumed that the large instantaneous secondary electron flux at the time of the beam current surge created a high electric field point somewhere in the detector (perhaps a whisker on an anode wire), which limited the current. No useful data were obtained with the MWPC at LBL because of this problem. During the NSCL experiment, the MWPC appeared to be functioning properly during the on-line analysis, however, subsequent scanning of the data showed that the MWPC was being gated properly for singles events only. The coincidence events, for which the detector was designed, had MWPC wires in the events a substantial amount of the time, however, the wires seldom corresponded to the array plastics which had fired in the event.

The MWPC has since been used in another experiment at NSCL. This time the detector functioned as originally expected. It is expected that some interesting results will be forthcoming from the use of the MWPC in this latest experiment.

CHAPTER III

EXPERIMENTAL SETUP

The experimental setups for the data to be presented can be divided into two distinct parts. Data was taken over two weekends at the Low Energy Beam Line (LEBL) at the Lawrence Berkeley Laboratory Bevalac using the same beam and target combination, 100 MeV/n ^{40}Ar+Au, and with similar detector combinations and experimental goals each weekend. Another experiment, which was performed at the National Superconducting Cyclotron Laboratory (NSCL) at Michigan State University, used a single beam with two different targets, 30 MeV/n ^{12}C+Au,Al, and a single setup. We will discuss the experiment at LBL first.

A. LBL Experimental Setup

The experimental setup for the 60 inch Maryland chamber is shown in Figure III-1. The positions and solid angles for the detectors are given in Table III-1. All of the detectors to be described here were not in the chamber for both weekends. Differences will be pointed out in the discussion for each detector. The plastic scintillator telescope array (See Chapter II) was positioned in the chamber with the center three telescopes at the beam height (Figure II-2). This array was the only detector which was

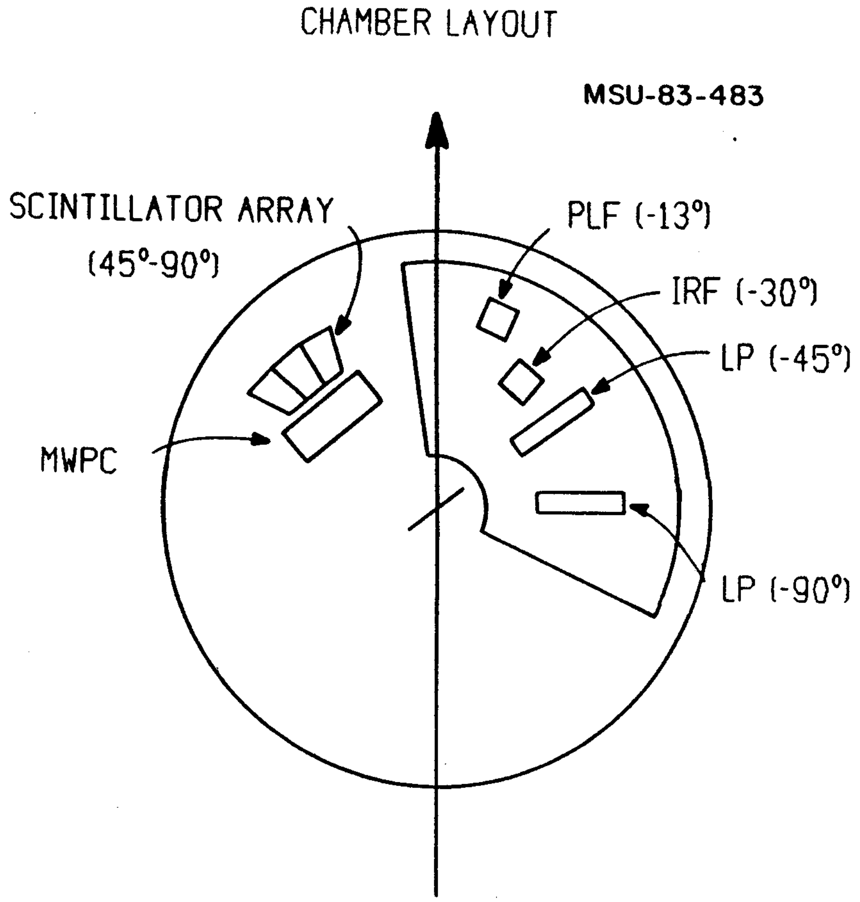

Figure III-1. Chamber setup during the LBL and NSCL experiments.

TABLE III-1

DETECTOR ANGLES FOR THE BEVALAC SETUP

DETECTOR	THETA (DEG)	PHI (DEG)	SOLID ANGLE (MSR)
PLF(a)	-13.0	0.0	24.7
IRF(b)	-30.0	+10.0	16.0
IRF(c)	-30.0	-10.0	14.0
LP(d)	-45.0	0.0	4.5
LP(e)	-90.0	0.0	10.9
ARRAY(f)	45,67.5,90	0.0	12.0

(a) Projectile-like fragment telescope first weekend.

(b) Intermediate Rapidity fragment telescope second weekend. High energy stack.

(c) Intermediate Rapidity fragment telescope second weekend. Low energy stack.

(d) Light Particle telescope first weekend.

(e) Light Particle telescope second weekend.

(f) Scintillator Array. Angles are for the central element of the array.

moved during the experiment and three runs were taken with the center telescope at 45.0, 67.5, and 90.0 degrees, respectively. This allowed essentially a full coverage of the in-plane angles from 38 to 97 degrees for light particles. The plastic scintillator telescopes functioned properly throughout the experiment, although, due to an unforeseen timing problem with the scaledown modules for the singles events during the first weekend, the ADC gates for the plastic scintillator singles data were off by about 50 nsec. This was enough to prevent useful recovery of the first weekend singles data. The scaledown modules were not used during the second weekend. The energy calibrations will be discussed in Chapter IV. In order to improve the coincidence counting rate the singles gate was removed from the electronics logic at the Master "OR" for most of the runs. These runs will be referred to as "coincidence" runs as opposed to the runs in which the singles gate was not removed which will be referred to as "singles" runs.

A high energy fragment detector was placed at -13 degrees as a Projectile-Like Fragment (PLF) trigger for the plastic array during the first weekend. This detector consisted of a five element silicon stack (800 μm, 5 mm, 5 mm, 5 mm, and 5 mm) which measured spectra for near beam rapidity fragments from Li through Ar.

During the second weekend a fragment detector was placed at -30 degrees as an Intermediate Rapidity Fragment trigger for the plastic array. This trigger consisted of two separate silicon stacks placed at the same in-plane angle but at out of plane angles of ±10 degrees. The low energy stack (100 μm, 300 μm, and 5 mm) measured spectra for particles $3 \leq Z \leq 8$, while the high energy stack (800 μm, 800 μm, 5 mm, 5 mm, and 5 mm) measured spectra for particles from Li through Mg.

During the first weekend, a Light Particle telescope (LP) was placed at -45 degrees as a light particle trigger for the plastic array. The LP detector was placed at -90 degrees during the second weekend. This detector was a silicon (1 mm) - NaI(Tl) (10 cm) telescopes and measured spectra for light particles (p, d, t, ^{3}He, and ^{4}He). Unfortunately, the p, d, and t spectra for the -45 degree setting were restricted to low energies due to a high threshold setting for the LP Si constant fraction discriminator.

Data acquisition at the Low Energy Beam Line was controlled by a PDP 11/34 computer through an MBD CAMAC interface. Experiment control and on-line data sampling and histogramming were done using the programs QDA and MULTI running on the PDP. Figure III-2 shows the electronics diagram for the LBL and NSCL experiments. Note that the scaledowns were removed from the electronics for the second weekend. In order to improve the coincidence counting rate the singles gate was removed from the electronics logic at the Master "OR" for most of the runs. These runs will be referred to as "coincidence" runs as opposed to the runs in

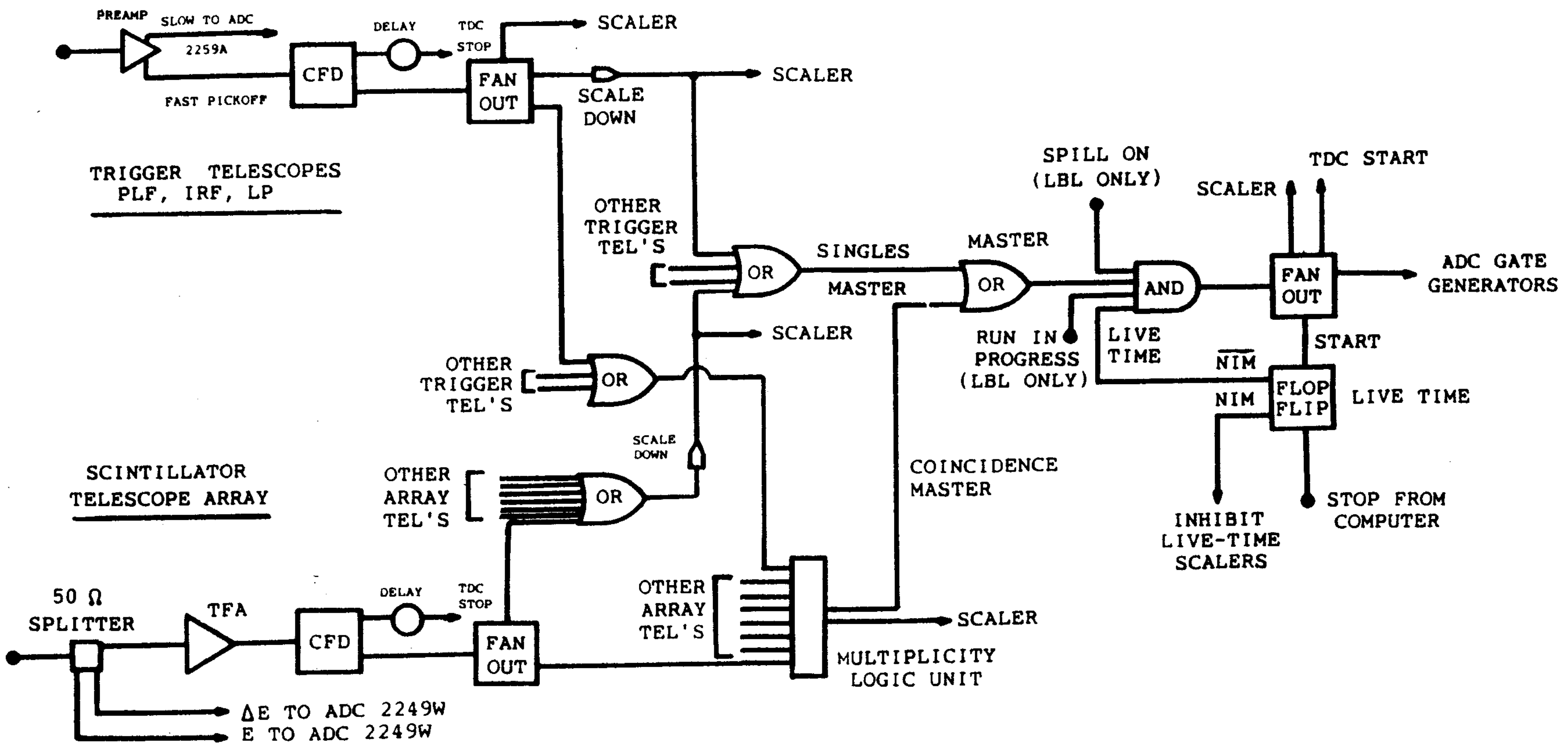

Figure III-2. Electronics schematic for the LBL and NSCL experiments.

which the singles gate was not removed which will be referred to as "singles" runs.

The time structure of the Bevalac ^{40}Ar beam was a beam spill of approximately 500 ms duration every 3.5 sec [Be 79]. The beam intensity was typically 1X10^{7} particles per spill. This resulted in measured livetimes of approximately 20 percent for runs in which both singles and coincidence events were taken without scaledowns on the singles events. For runs in which the singles were scaled down or ignored entirely, the livetimes were approximately 80 percent. The beam current was monitored with an ion chamber which had been calibrated against a counting scintillator at low beam current (<1X10^{6} particles per spill). Figure III-3 shows the ion chamber calibration for the second weekend. Results of a least squares fit to the calibration are shown on the figure. A separate calibration for the first weekend gave a similar fit. For beam currents higher than 1X10^{6} the counting scintillator saturated, hence, the need for the ion chamber for which the response was expected to remain linear up to 1X10^{12} particles per spill.

The target for the LBL experiment was a self-supporting 213 mg/cm^{2} Au foil.

The beam energy out of the Bevatron, as determined by the Bevatron field, was 100 MeV/n. However, a 50 μm aluminum vacuum window in the beamline degraded the beam energy to a calculated value of 92 MeV/n.

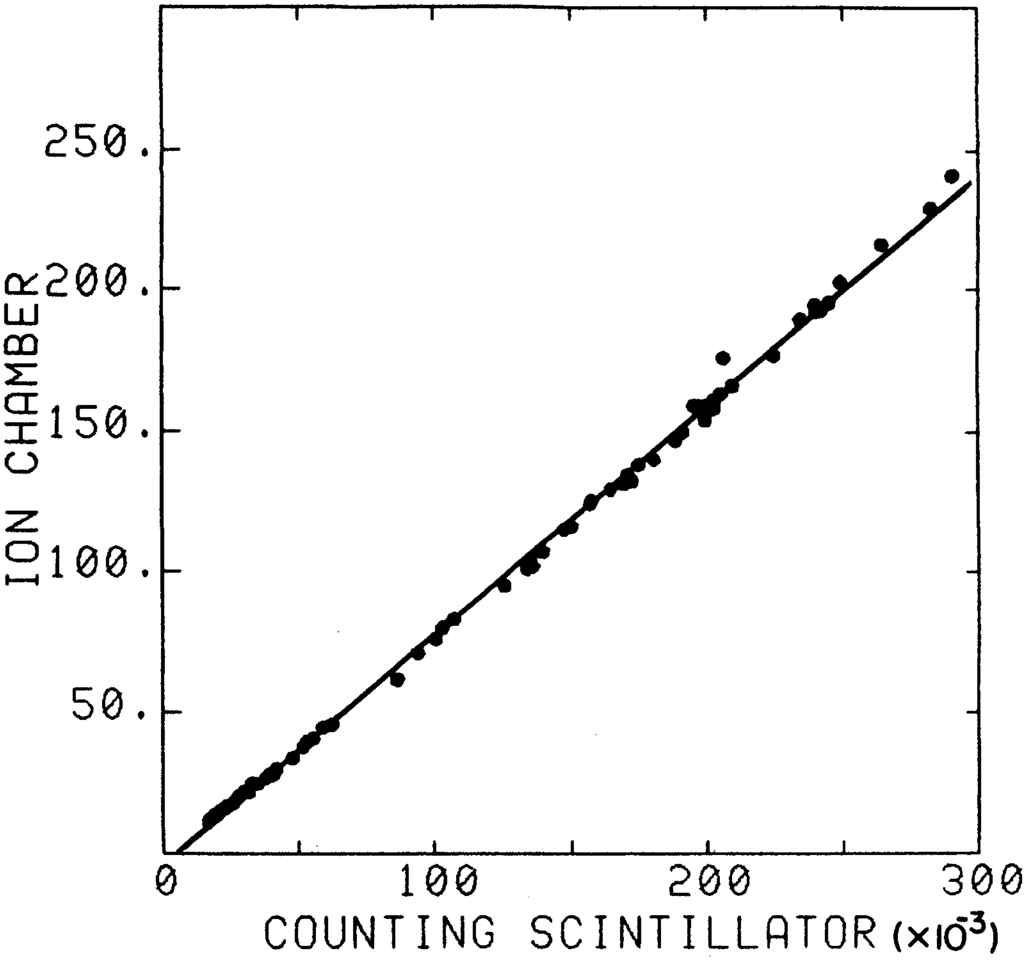

Figure III-3. Ion chamber count rate calibration for the second weekend at LBL. The solid line is a least squares fit.

B. NSCL Experimental Setup

The setup for the 60 inch chamber at NSCL is shown in Figure III-1. Note that the LP detector at -90 degrees was not in place for this experiment. The positions and solid angles for the detectors are given in Table III-2. The plastic scintillator array (See Chapter II) was positioned in the chamber with the bottom two telescopes at the beam height (Figure II-2). As in the LBL experiment, the array was the only detector which was moved during the experiment and the central detector was positioned at various angles from 45.0 degrees to 93.0 degrees.

A high energy fragment detector was placed at -13 degrees as a Projectile-Like Fragment trigger for the plastic array (PLF). This detector consisted of a three element silicon stack (800 μm, 5 mm, and 5 mm) which measured spectra for near beam rapidity fragments from Li through C.

A second fragment detector was placed at -25 degrees as an Intermediate Rapidity Fragment trigger for the plastic array (IRF). This detector consisted of a three element silicon stack (100 μm, 300 μm, and 5 mm) which measured spectra for particles from Li through C.

A third detector was placed at -45 degrees as a Light Particle trigger for the plastic array (LP). This detector was a silicon (400 μm) - NaI(Tl) (10 cm) telescope which measured spectra for p, d, t, ^{3}He, and ^{4}He.

TABLE III-2

DETECTOR ANGLES FOR THE NSCL SETUP

DETECTOR	THETA (DEG)	PHI (DEG)	SOLID ANGLE (MSR)
PLF(a)	-13.0	0.0	4.38
IRF(b)	-25.0	0.0	6.89
LP(c)	-45.0	0.0	13.8
ARRAY(d)	47,56,71,90	6.5	14.9
ARRAY(e)	45,56,71,90	6.5	14.9

(a) Projectile-like fragment telescope.
(b) Intermediate Rapidity fragment telescope
(c) Light Particle telescope.
(d) Scintillator Array for the Au target. Angles are for the central element of the array.
(e) Scintillator Array for the Al target. Angles are for the central element of the array.

Data acquisition at NSCL was controlled by a VAX 11/750, running the program PEEKABOO, connected to an LSI-11/23 processor through a CAMAC serial highway [Au 83]. The electronics diagram is shown in Figure III-2.. As was the case for the second weekend at LBL, the scaledowns were not used during this experiment. Again, the singles gate was removed from the electronics logic at the Master "OR" for most of the runs.

The un-pulsed 30 MeV/n $^{12}C^{4}+$ beam current was monitored in a well shielded faraday cup placed approximately two meters beyond the exit port of the scattering chamber. The current was integrated in a BIC Current Integrator [Bi 80] and was recorded in the computer using a CAMAC scaler module. Apparently, there was an impedence mismatch in the logic ouput of the current integrator causing considerable ringing. This generated a non-constant multiple pulsing at the scaler module. From a comparison with data taken with 35 MeV/n $^{12}C+Au$ and comparisons of actual current integrator front panel meter readings with the scaler readings, it seems that the multiple pulsing was approximately a factor of 10. It was possible to cross normalize the various singles runs in the experiment relative to themselves since the trigger detectors never moved and therefore had constant cross sections. The coincidence runs were normalized relative to the singles runs and therefore relative to themselves by comparing the plastic array cross sections in the coincidence runs at the various angle settings to the same cross sections in the singles runs. The errors involved in such a process are not negligible and will be discussed in Chapter IV. The beam intensity varied from 0.33 particle namps ($2X10^9$ particles per second) to 2.5 particle namps ($1.5X10^{10}$ particles per second) giving livetimes for the singles runs of as low as 15 percent and as low as 60 percent for the coincidence runs.

The targets for the NSCL experiment were self-supporting natural Au and Al foils of 2.0 mg/cm^2 and 3.0 mg/cm^2 thickness, respectively.

The beam energy out of the NSCL cyclotron as determined by the accelerator settings was 30 MeV/n. The beam energy was not degraded in passing to the scattering chamber.

CHAPTER IV

DATA REDUCTION AND ANALYSIS

The data taken in the experiments at LBL and NSCL were recorded on magnetic tape in event form. The event data were later read back onto the computer and sorted by particle type using software gates which had been created with the aid of a two dimensional color display device. The sorted data were then calibrated, binned into histograms and corrected for various experimental effects. Normalizations were applied to obtain the final absolutely normalized spectra. The energy calibrations will be discussed first.

A. Energy Calibrations of Detectors used in LBL Experiment

Energy calibrations for the scintillator array telescopes in the LBL experiment were based on direct beam calibrations done before the second weekend. Since the timing for the ADC gates was changed between the first weekend and the beam calibration, the first weekend spectra for the scintillator array telescopes had to be calibrated against spectra from the second weekend. Further details of the first weekend calibration will be presented after the discussion of the actual beam calibration of the second weekend spectra.

The ability of the Bevatron to produce very low intensity proton and alpha particle beams of 150 MeV/n made it possible to safely calibrate the scintillator detectors by positioning them directly in the beam. A full beam energy calibration point and five lower energy points were obtained for both protons and alphas by degrading the beam in a stepwise variable thickness Cu degrader placed in the target ladder. The energy of each calibration point was determined from the Bevatron beam energy, less any energy loss due to obstructions in the beam line and the calculated energy loss in the degrader. Figure IV-1 shows the calibrations for protons and alpha particles in one of the plastic E elements. The particle energy is the actual energy deposited in the plastic, taking into account the energy loss of the particle in the ΔE element. Note that the proton calibration is linear up to the maximum calibrated energy of 150 MeV. The alpha calibration becomes nonlinear beyond 250 MeV. The difference in slope is due to differences in the NE102 response for the two particles, as shown in Figure IV-2 [Go 60]. The nonlinearity in the alpha response is a result of reaction losses in the scintillator which will be discussed later in the chapter. All seven of the plastic scintillator elements had similar calibrations. No correction was made to the E signal for contributions from the ΔE signal, since knowing the energy deposited in the scintillator made that correction unnecessary. The ΔE signal was, however, corrected for the contribution from the

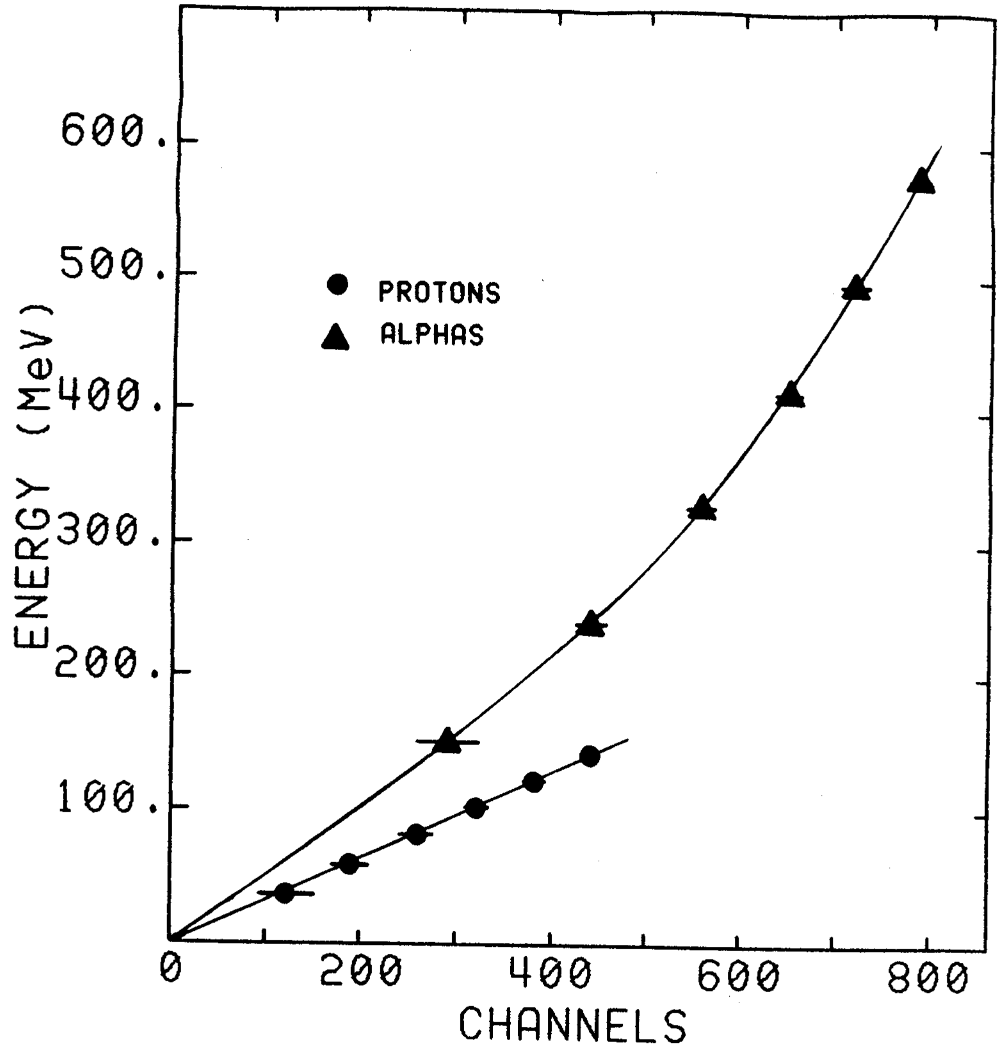

Figure IV-1. Energy calibration for protons (circles) and alphas (triangles) in the plastic scintillator E element of a scintillator array telescope. The lines are least squares fits.

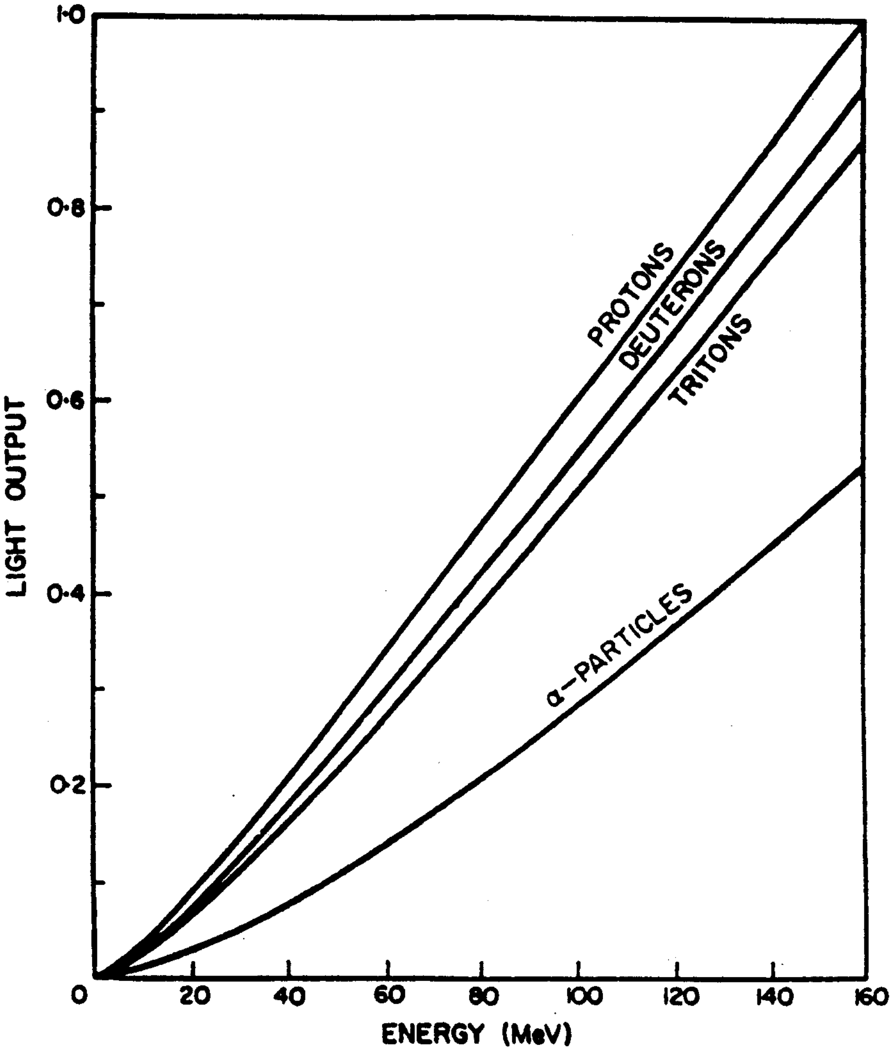

Figure IV-2. NE102 plastic scintillator. Calculated scintillation response to protons, deuterons, tritons and α-particles. [Go 60] tail of the E signal which was collected in the ΔE gate. This correction was necessitated by the fact that at high particle energies the magnitude of the contribution was great enough to cause the ΔE value to begin to increase. Without a correction, this increase gave rise to a double-valuedness for the calibration of the ΔE element as shown in Figure IV-3. The correction applied to the data was derived from that portion of the ΔE-E spectra which contained the neutrons and gamma-rays which triggered the detector by stopping in the plastic (Figure IV-4). For these events, no signal was generated in the ΔE element and therefore, the contribution of the E signal to the ΔE can be obtained. The correction was made by calculating the difference between the ΔE channel of the n,γ line at the minimum E channel and the ΔE channel of the n,γ line at the E channel corresponding to the ΔE channel to be corrected. This difference was then subtracted from the ΔE channel number to give the corrected channel number. As can be seen from Figure IV-5, the resulting corrected calibration curves were quite linear for both protons and alphas. As was true for the plastics, the ΔE CaF_2 calibration was similar for all seven telescopes.

As was stated at the beginning of this chapter, the energy calibration for the scintillator array telescope spectra from the first weekend at LBL had to be obtained by comparison to spectra from the second weekend. Because the first weekend array singles spectra were lost due to a

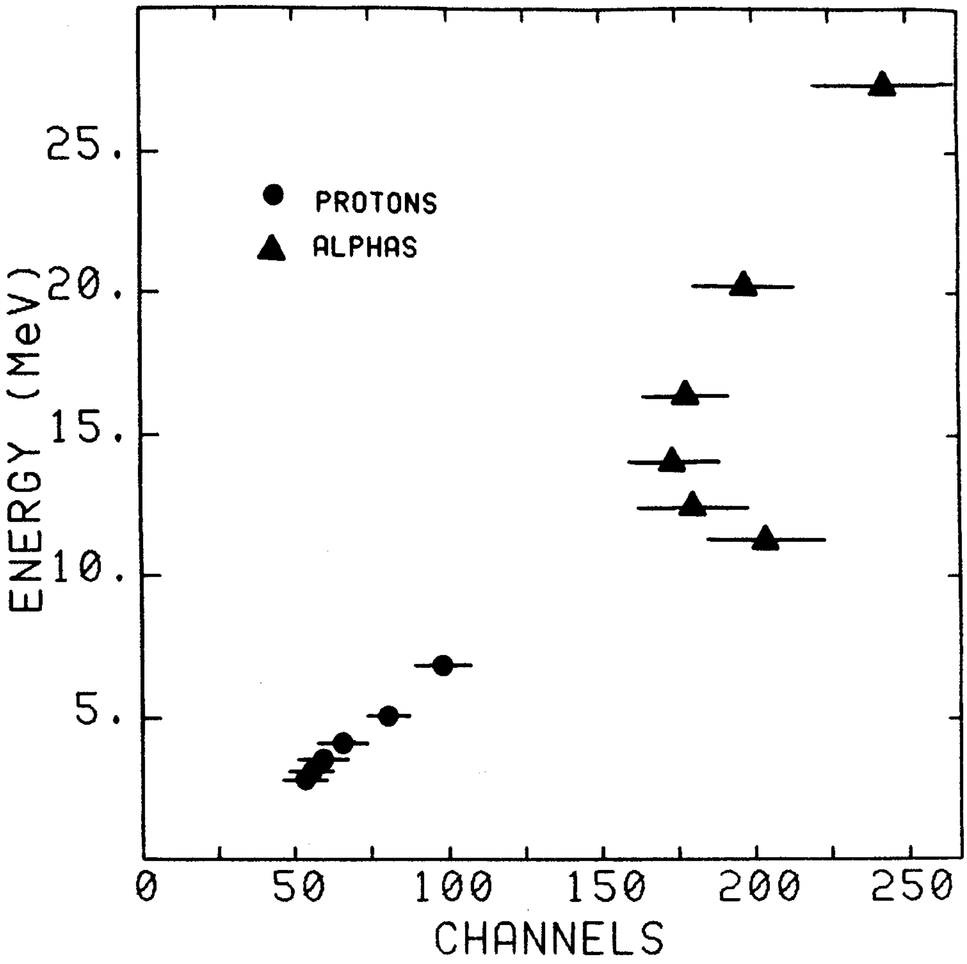

Figure IV-3. Uncorrected energy calibration for protons (circles) and alphas (triangles) in the CaF_2 ΔE element of a scintillator array telescope.

MSU-83-485

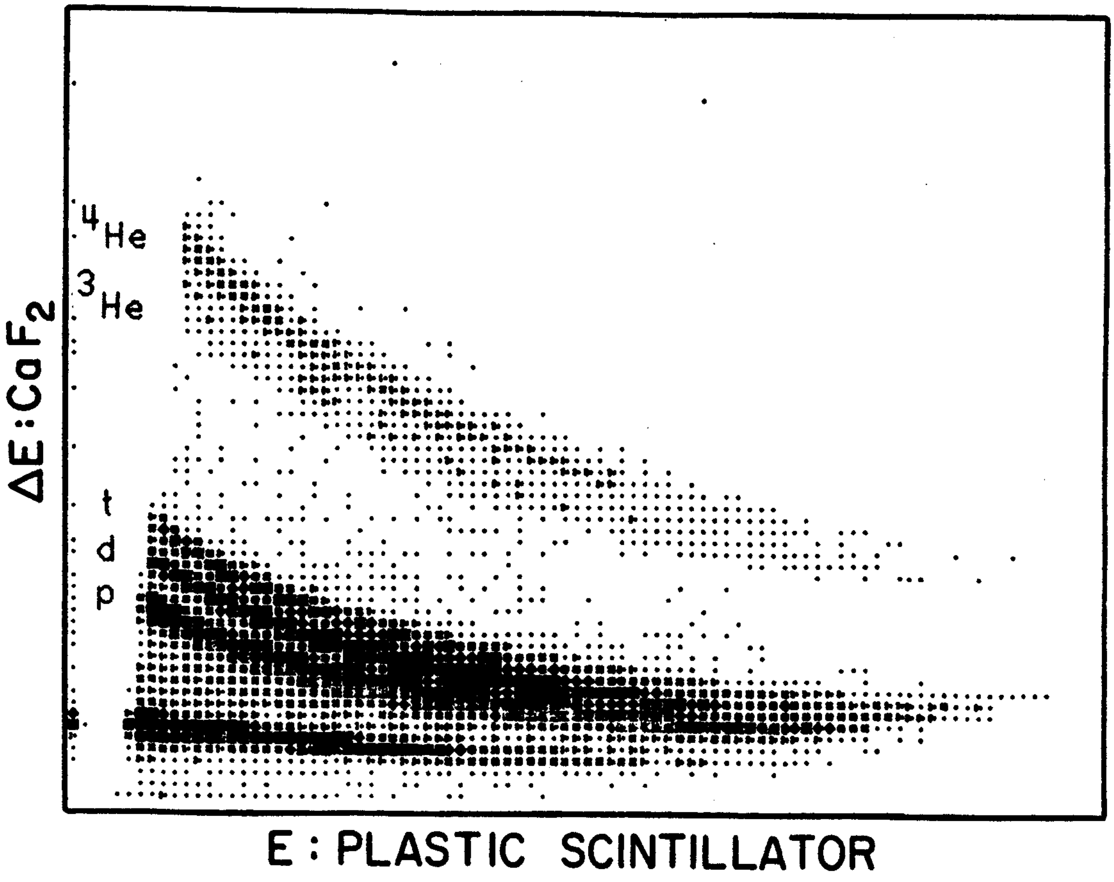

Figure IV-4. Plot of ΔE vs. E for a scintillator array telescope. Note prominent band at the botton is caused by neutrons and gammas stopping in the plastic.

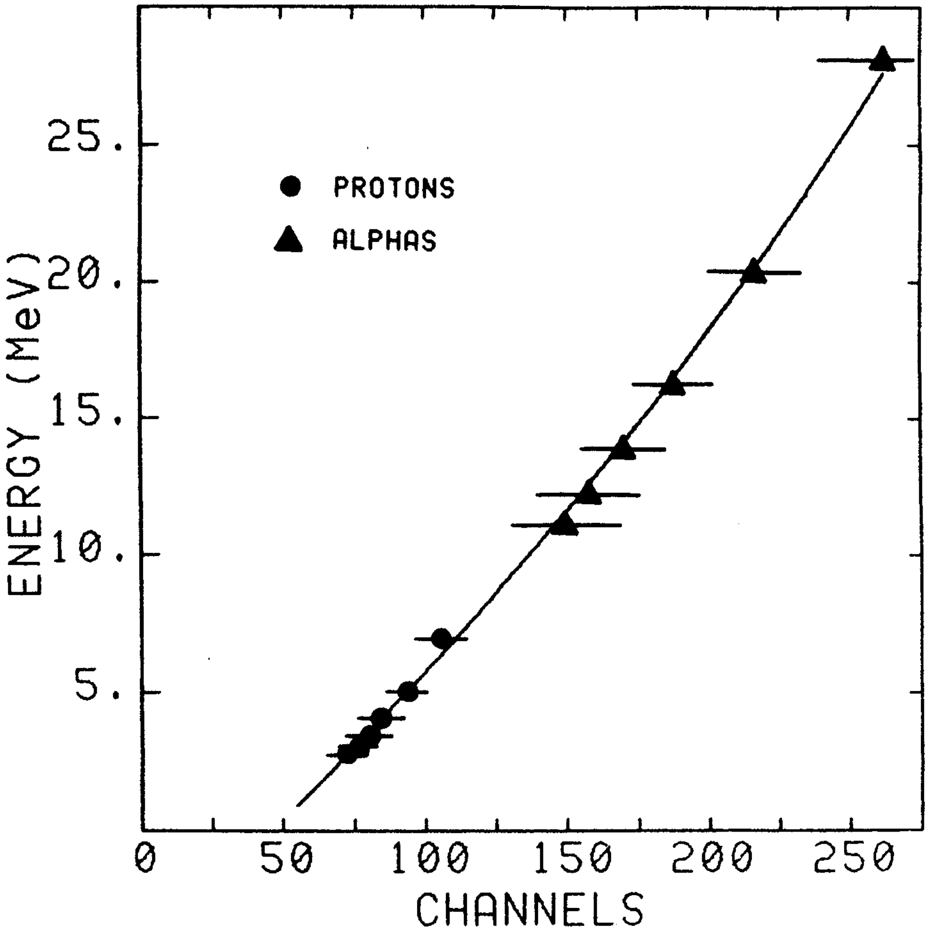

Figure IV-5. Corrected energy calibration for protons (circles) and alphas (triangles) in the CaF_2 ΔE element of a scintillator array telescope. The line is to guide the eye. Separate calibrations were used for protons and alphas.

timing problem with the scaledowns, the calibrations for the first weekend were further restricted to fits to coincidence spectra. The CaF_2 ΔE spectra and the plastic scintillator E spectra were matched to spectra from the second weekend using a least squares fitting routine which determined the proper calibration for each telescope. The correcton to the ΔE response for charge from the E signal in the ΔE gate, which was made for the beam calibration, was also made for the fitted calibration. Values of the reduced chi-squared for the fits were typically less than 5 and a comparison of the final normalized coincidence spectra indicated that a satisfactory calibration was obtained.

The Si ΔE element of the Si-NaI telescope at the -90 degree setting was calibrated with a calibrated pulser. A calibration using the direct proton and alpha beams gave similar results. The NaI E element was calibrated using the direct proton and alpha beams, as shown in Figure IV-6. The Si-NaI telescope at the -45 degree setting was calibrated using only the direct alpha particle beam for the NaI E element and a pulser calibration for the Si ΔE element.

The various fragment detectors, which all consisted of stacks of silicon detectors, were calibrated with the calibrated pulser.

B. Energy Calibrations of Detectors used in NSCL Experiment

The calibration of the scintillator array telescopes at NSCL presented a special challenge in that at the time of

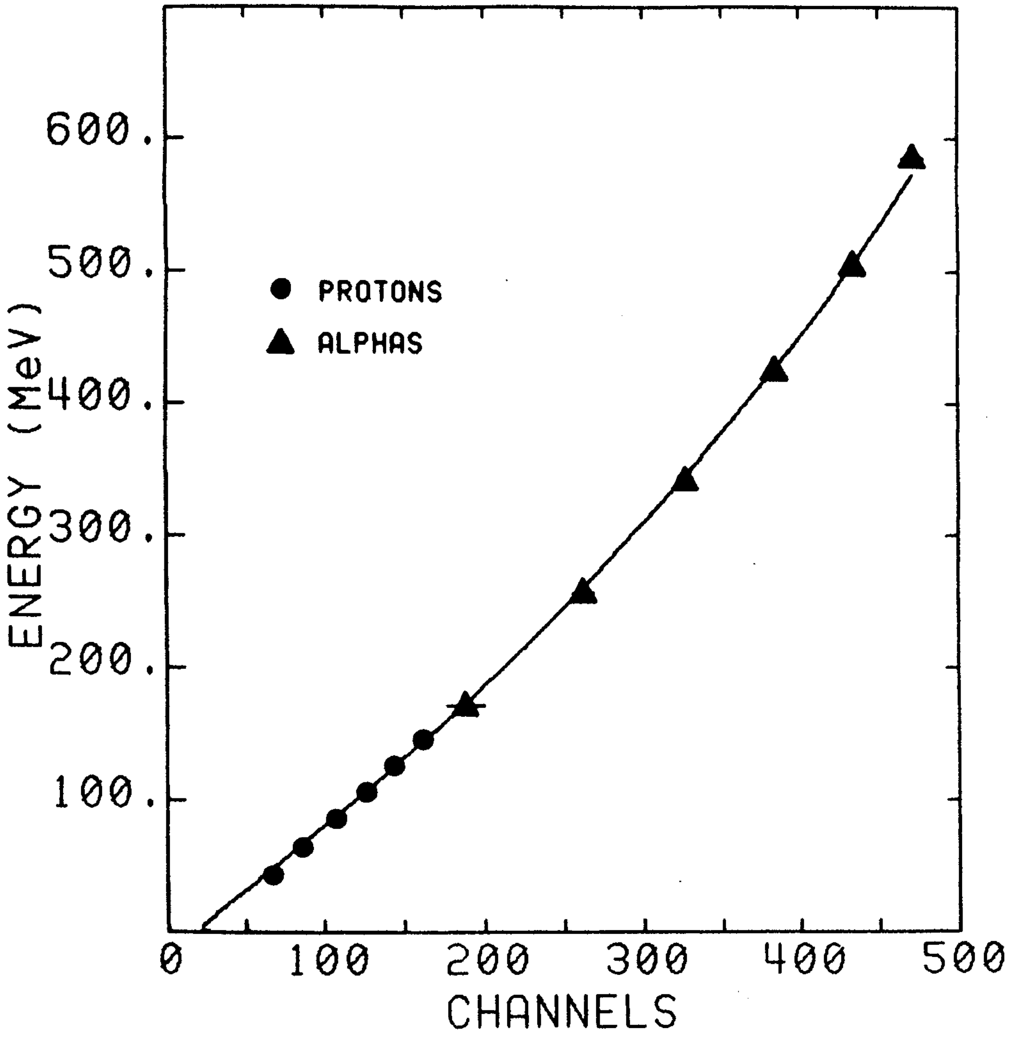

Figure IV-6. Energy calibration for protons and alphas in the NaI E element of a Silicon-NaI telescope. The line is to guide the eye. Separate calibrations were used for protons and alphas.

the experiment, the best beam available for energy calibrations was a 25 MeV/n alpha particle beam. An attempt was made to calibrate using 25 MeV/n alphas elastically scattered from a Au target. However, since the minimum energy for an alpha particle which penetrates the CaF_2 is 22 MeV/n, and since the proton and alpha particle calibrations are not the same, as shown in Figure IV-1, this calibration proved to be inadequate. Approximately one year after the original data was taken a 53 MeV/n alpha beam became available, at which time inclusive p, d, t, ^{3}He, and ^{4}He spectra were measured for the original reactions of 30 MeV/n ^{12}C+Au,Al using a Si-NaI telescope. Calibration points were obtained for 53 MeV/n alpha particles elastically scattered from a Au target and for 70 and 100 MeV recoil protons from alpha elastic scattering on a mylar target. The recoil protons were measured in coincidence with the elastically scattered alphas, giving well separated proton calibration peaks. These calibrated spectra were then used to calibrate the original spectra using a fitting technique similar to that used to calibrate the first weekend spectra from LBL. The ΔE calibration was retained from the 25 MeV/n alpha calibration and was used for both protons and alphas. No correction was made in the ΔE channel number for the contribution from the E signal since the measured particle energies did not extend to high enough energies to show a significant contribution.

The Si-NaI telescope was calibrated using a calibrated pulser for the silicon ΔE element and the 25 MeV/n alpha calibration for the NaI E element. The NaI inclusive data were compared to the 45 degree data taken in the more recent calibration run with 53 MeV/n alphas and found to be in good agreement.

The fragment detector telescopes were again calibrated with a calibrated pulser.

C. Normalizations

The method for monitoring the beam currents in the two experiments has been discussed in Chapter III. All runs with the same detector settings were summed for the coincidence events. The singles events were summed only for singles runs, ie. the runs in which the singles event trigger was present in the electronics logic. Pseudo singles events were present in the coincidence runs due to coincident neutrons and gamma rays and other unidentifiable coincident particles, but, these events were biased by the coincidence trigger requirements and therefore, did not constitute true singles events.

The NSCL spectra originally had only a relative normalization because of a problem with the current integrator which was discussed in Chapter III. It was possible, however, to provide an absolute normalization for the spectra by normalizing to the spectra measured in the recalibration run. It is believed that the normalization for the NSCL spectra is known to approximately 20 percent based on errors incurred in the cross normalization of the coincidence spectra discussed in Chapter III and the absolute normalization method, which is believed to be known to 10 percent. The LBL normalizations are believed to be good to 10 percent.

D. Target Thickness Correction

Because of the 213 mg/cm^2 Au target thickness at LBL, the fragment spectra (PLF and IRF) were corrected for energy losses in the target. The corrections were based on the energy lost by a given particle at a given energy in the full thickness of the target, including the added thickness encountered by the particle due to the target angle relative to the detector. Corrections were typically less than 20 MeV. The bin sizes for the inclusive fragment histograms were 100 MeV for the PLF and 30 MeV for the IRF and a factor of two larger for the coincidence histograms. This was therefore, a relatively small correction to the spectra. This correction was not applied to the NSCL spectra due to the small thickness of the 2.0 mg/cm^2 Au and 3.0 mg/cm^2 Al targets.

E. Reaction Loss Correction

The scintillator array and Si-NaI telescope spectra were corrected for reaction losses of the light particles stopping in the detectors. Charged particles traversing a scintillation counter or solid state counter may undergo nuclear interactions as well as interactions with the atomic electrons. The latter type of interaction gives rise to the full energy peak in the detector. The nuclear interactions, on the other hand, tend to broaden the full energy peak on the low energy side. Inelastic collisions in the detector typically have neutrons, gammas, deuterons, and alphas as the reaction products. Due to the nonlinearity of the response of scintillation materials to more highly ionizing particles, the light output in the detector is less for these reaction products than it would have been for the original projectile. This results in the loss of the particle from the full energy peak. In the case of neutrons and gammas, light output is less because of the reduced probability of any further interaction in the detector by the reaction products. Other effects can also lead to losses in the detector. We will discuss one of them, scattering out of the detector, later on in the chapter.

A number of authors have presented data and calculations for reaction losses in detector materials such as silicon [Ja 66, Ma 68 and Me 69] and NaI(Tl) and plastic scintillator [Ja 66 and Me 69]. We have patterned our calculation after that of Measday and Richard-Serre [Me 69]. The calculation requires the integration of the total inelastic reaction cross section of the incident particle as it stops in the detector. The range of the particle is divided up into cells of about 0.1 mg/cm^2 in length. At each cell the particle has a different energy and since the reaction cross section is energy dependent, the reaction cross section must be determined for the average energy of each cell. The average energy in each cell was calculated from a range-energy table generated by the code DONNA. The reaction cross section was then calculated using a parameterization obtained by fitting a modified form of the standard reaction cross section

$$\sigma_R=\pi R^2(1-V_C/E)x(1+(\kappa/E)^{\lambda}) \qquad \text{(IV-1)}$$

to measured cross sections tabulated by Measday and Richard-Serre [Me 69]. The parameters in Equation IV-1 are the nuclear interaction radius R given by

$$R=r_0(A_1{}^{1/3}+A_2{}^{1/3}-1) \quad \text{(fm)}, \qquad \text{(IV-2)}$$

where $r_0=1.2$ fm,

the coulomb potential at the interaction radius, V_C, given by

$$V_C=Z_1Z_2e^2/R \quad \text{(MeV)}, \qquad \text{(IV-3)}$$

and κ and λ which were adjustable parameters. An adjustable overall normalization factor was also included in the fit. The calculation of the reaction cross section was repeated for each cell with the total fraction of interactions being given by

$$f=1-\exp(-\sum_i n_i\sigma_i), \qquad \text{(IV-4)}$$

where n_i is the number of atoms/cm² in the i^{th} cell and σ_i is the calculated cross section in each cell. The data and the parameterized fit for protons in carbon are shown in Figure IV-7. Although plastic scintillator also contains hydrogen, its contribution to the reaction loss is negligible since the scattered proton is likely to remain in the detector volume. The quality of the fit in Figure IV-7 was limited by the use of the standard reaction cross section formula as the basis for the fit. This parameterization was necessary in order to extend the cross sections to particles other than protons. Another limitation on the quality of the fit was the attempt to determine a single consistent set of parameters for all relevant materials. The values found for κ and λ were $\kappa=20$ MeV and $\lambda=1.2$, with the normalization constants being 1.1 for silicon, 2.0 for NaI, 2.7 for CaF_2, and 1.45 for plastic scintillator.

The resulting corrections for protons in NaI and plastic scintillator are shown in Figures IV-8 and 9 respectively, plotted as the ratio "tail-to-peak", i.e. f/(1-f), along with the data tabulated in [Me 69]. The agreement is good for both detector materials. The tail-to-peak ratios for p, d, t, ^{3}He, and ^{4}He in a silicon-NaI telescope and a scintillator array telescope are shown in Figures IV-10 and 11 respectively. The fit to the reaction cross section and the calculation of the correction factors

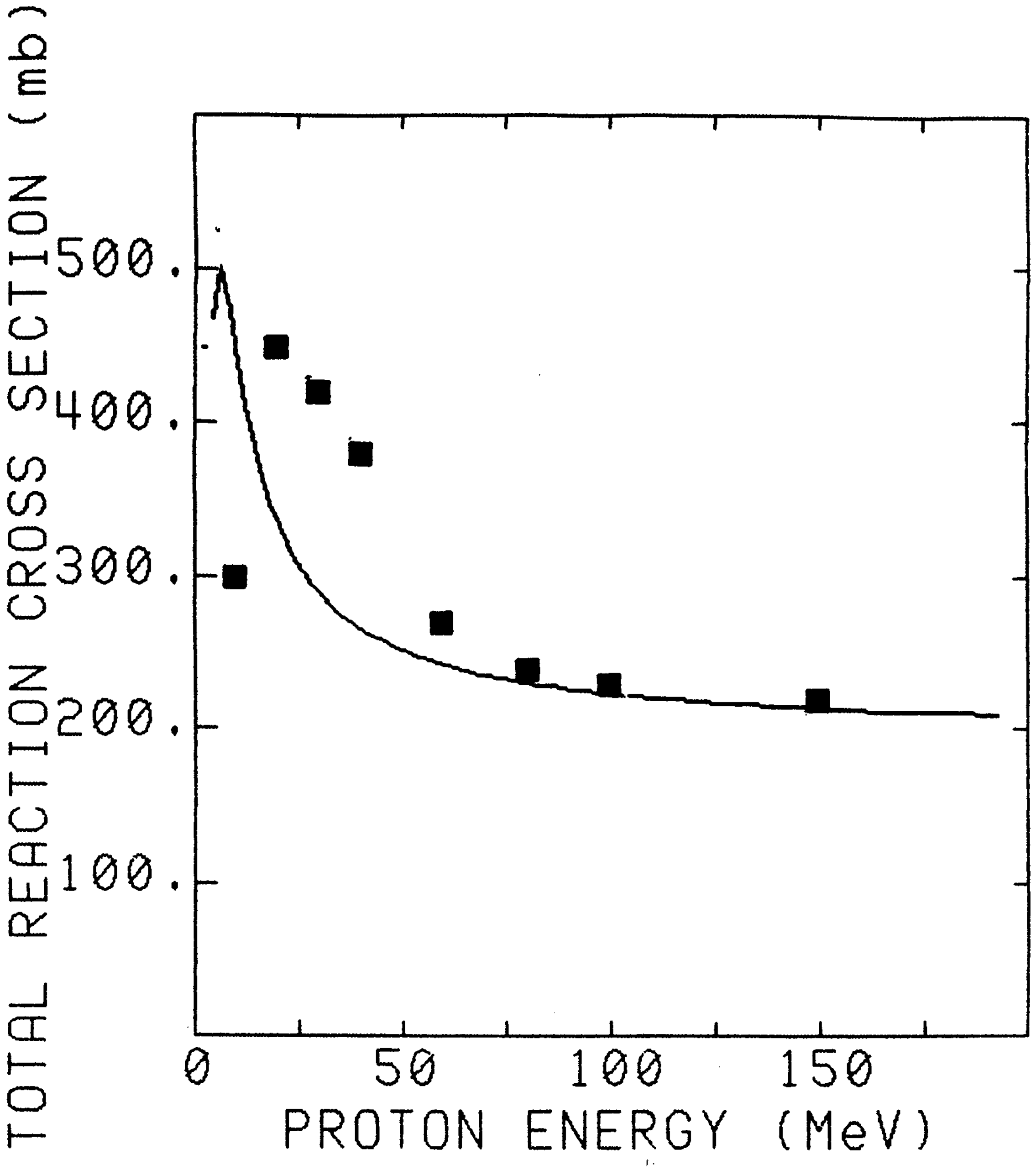

Figure IV-7. Parameterized fit to measured total reaction cross section for protons on carbon. Data is from Measday [Me 69].

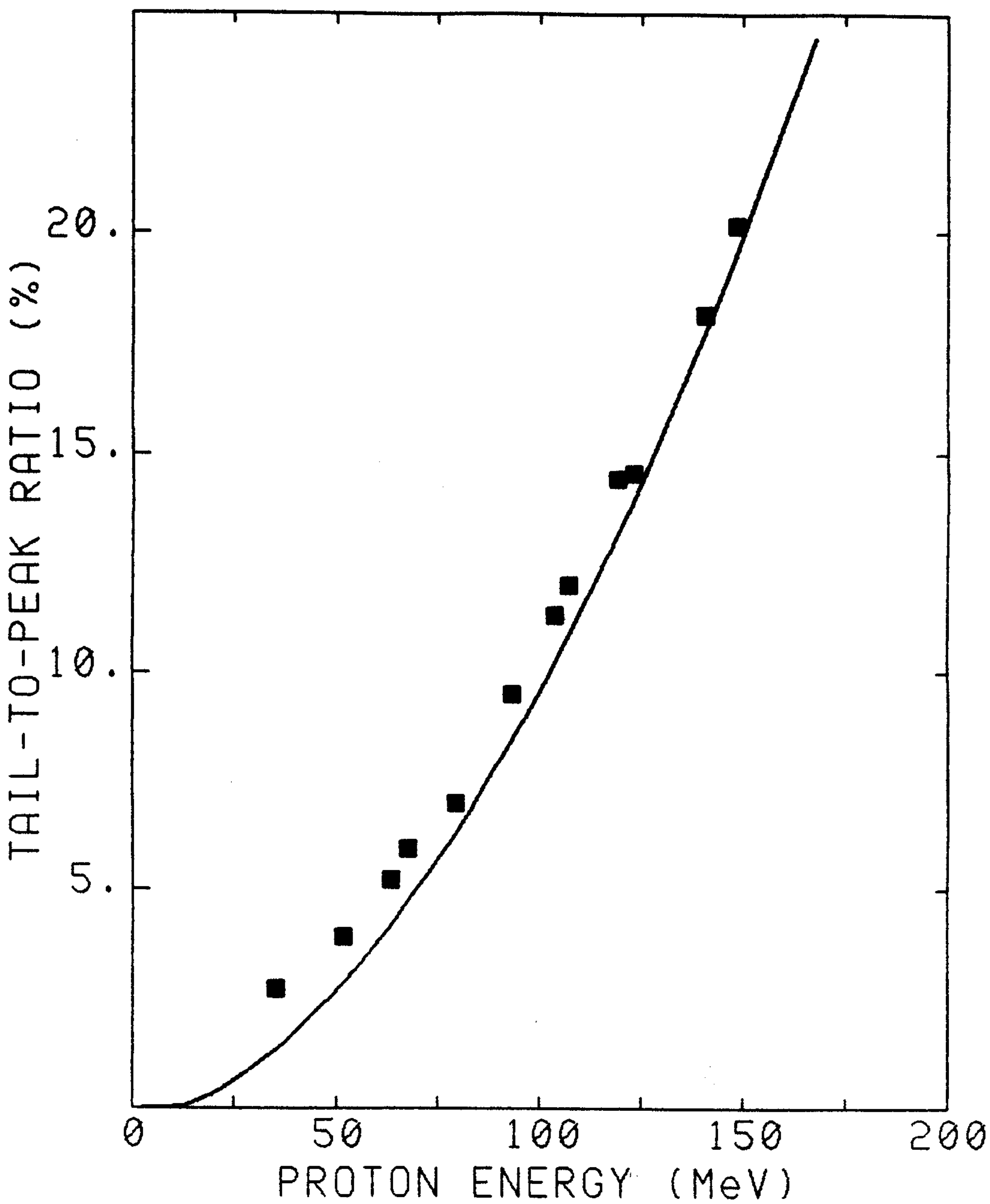

Figure IV-8. Calculated tail-to-peak ratio for reaction losses of protons in NaI with data compiled by Measday [Me 69].

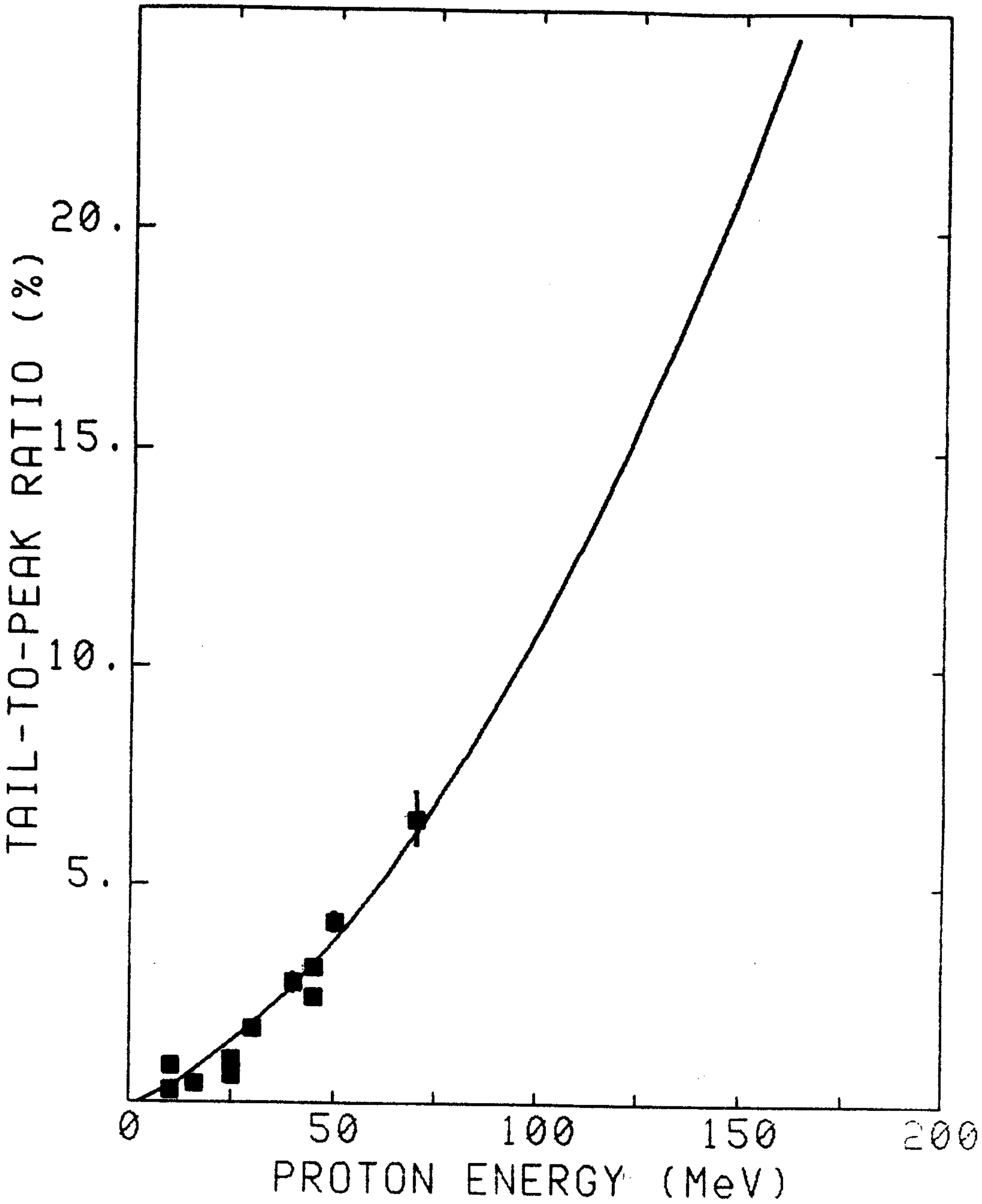

Figure IV-9. Same as Figure IV-8 for NE102 plastic scintillator.

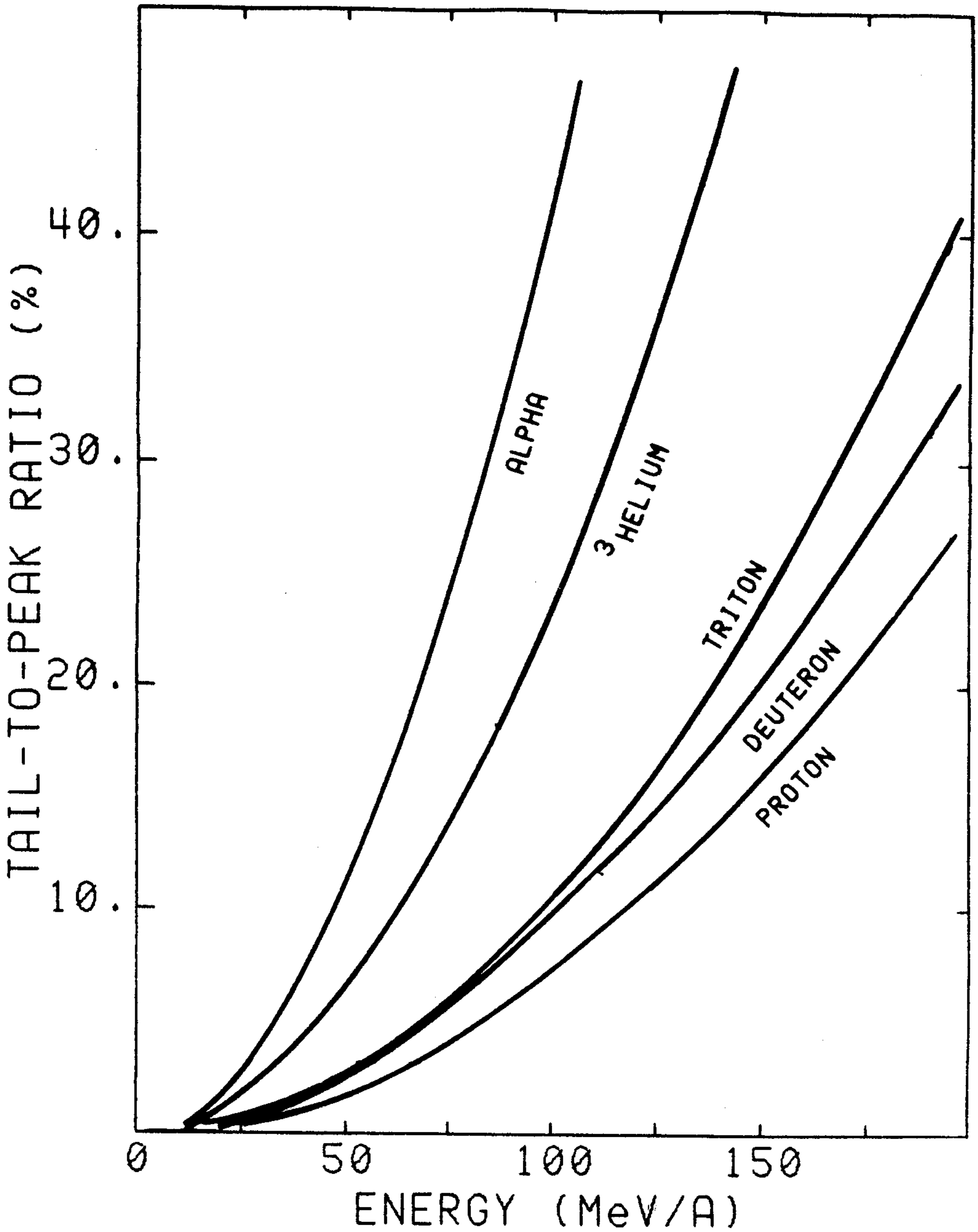

Figure IV-10. Calculated tail-to-peak ratios for reaction losses of p, d, t, ^{3}He and ^{4}He in the Silicon-NaI telescope.

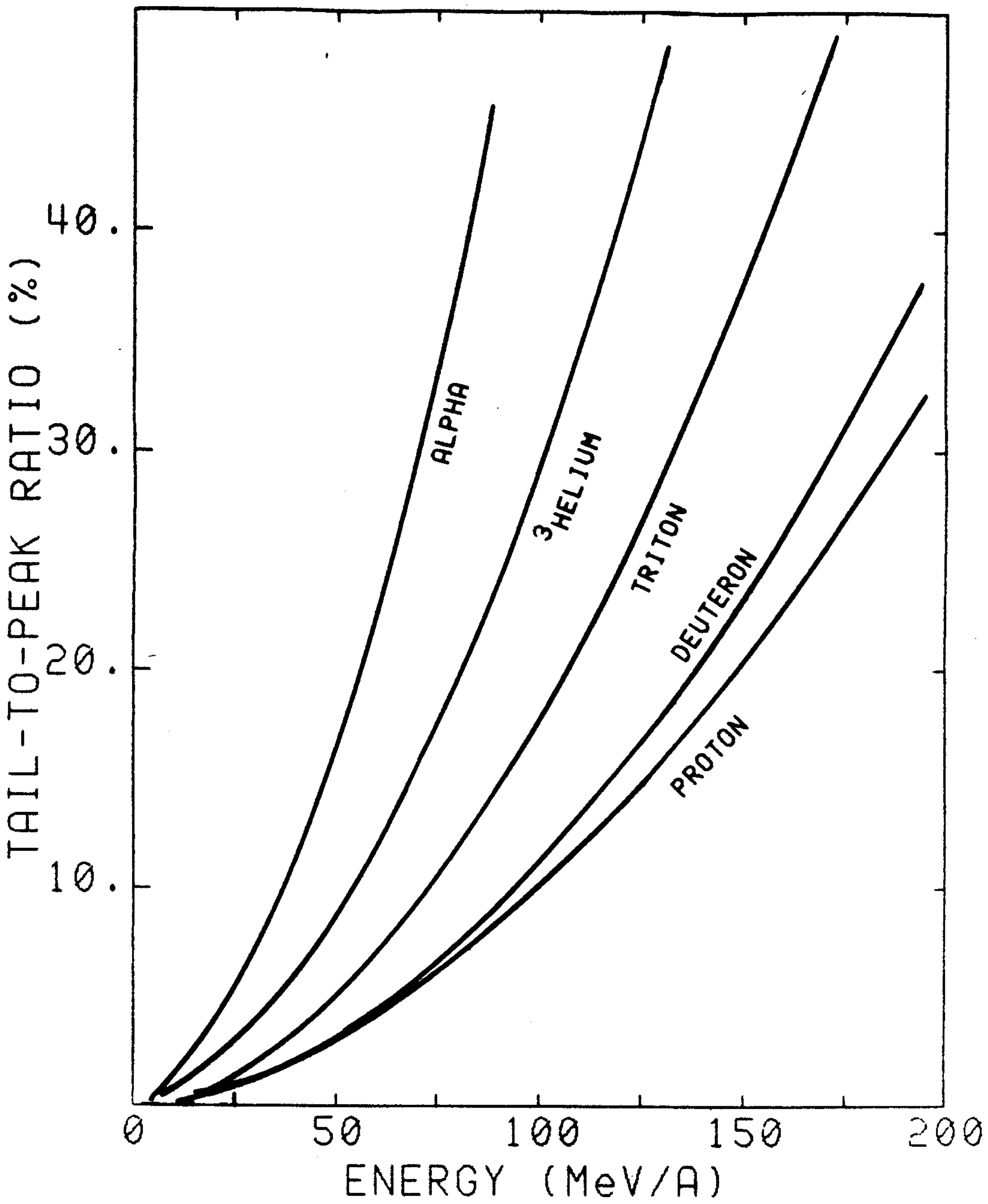

Figure IV-11. Same as Figure IV-10 for the scintillator array telescopes.

was also performed for the silicon ΔE element. No data or independent calculations were available for CaF_2, so parameters similar to NaI were used instead. The silicon and CaF_2 corrections had little effect on the overall correction because of their limited thickness. The actual correction to the spectra was made by dividing each bin by the appropriate value of $1-f$.

F. Scattering Out Correction

In order to achieve the high packing density of the scintillator array, the individual telescopes were not collimated. Particles incident near the edge of a detector were likely to scatter out and not be identified as valid events. This is the other important mode of particle loss in the array detectors. Particles scattering into the detectors from neighboring telescopes would not be identified as valid events since there would be no ΔE signal for such events. No correction is required for these events. To correct for the scattering out, a Monte Carlo calculation was developed to simulate the effects of transverse straggling of the particles and to correct for the slight geometrical error incurred by placing the telescopes closer than their design distance. The code calculated the range of a given energy particle in the plastic and then calculated its transverse straggling based on a gaussian distribution with a root mean square projected angle given by the formula [Pa 84]

$$\Theta_{proj} = \frac{Z\cdot 14(t+m_0)}{A\cdot t(t+2m_0)} (L/L_R)^{1/2}[1 + \frac{1}{9} \mathrm{Log}_{10}(L/L_R)][1 + \frac{Am_0}{(t+m_0)A_S}] \tag{IV-5}$$

where

t=Incident kinetic energy per nucleon,

m_0=931.5,

L=Thickness of material traversed (g/cm^2),

L_R=Radiation length,

A,A_S=Mass number of particle, medium,

Z=Atomic number of particle.

Radiation lengths for a variety of materials are tabulated in the literature [Pa 84]. Radiation lengths for unmeasured compounds were calculated based on a formulation given by Tsai [Ts 74]. The calculated trajectory of the particle was checked against the actual geometry of the detector to ascertain if the particle would have scattered out. The effect of transverse scattering in the CaF_2 was included in the calculation of the trajectory. The entrance point for each particle at each energy was also found using a Monte Carlo technique such that the geometry of the front face of the telescope was treated exactly with a constant probability at each point. The fraction scattered out, R, was calculated as the number of simulated events for which the particle scattered out divided by the total number of events. The correction factor with which each bin of the measured spectra was multiplied is then 1/(1-R). The fraction scattered out of a scintillator array telescope for p, d, t, ^{3}He, and ^{4}He are shown in Figure IV-12 plotted as tail-to-peak ratios.

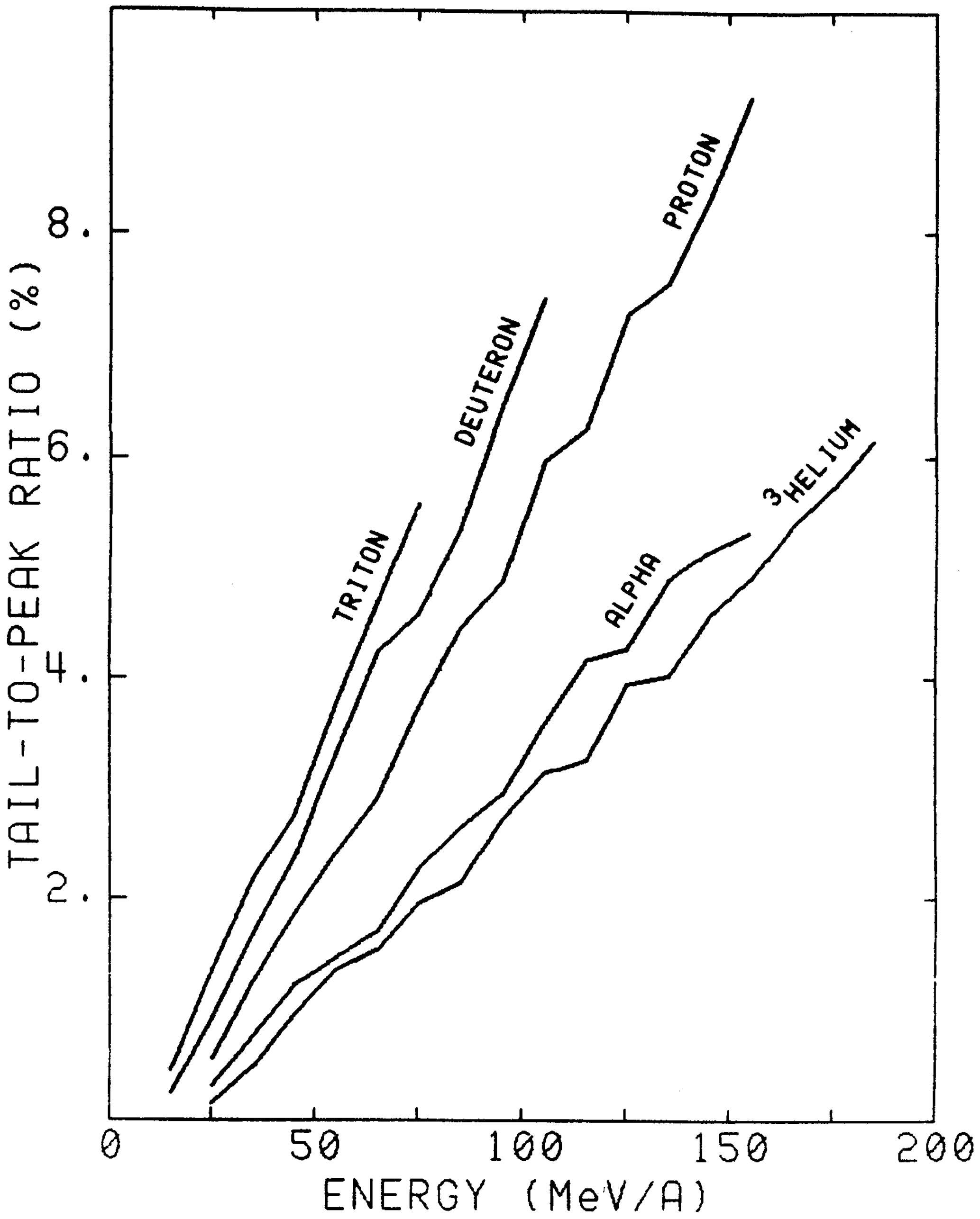

Figure IV-12. Calcuated tail-to-peak ratios for scattering out losses of p, d, t, ^{3}He and ^{4}He in the scintillator array telescopes.

CHAPTER V

RESULTS AND DISCUSSION

The data presented in this chapter are primarily light particle energy spectra derived from the scintillator array telescopes discussed earlier. Exceptions will be figures showing the inclusive spectra for the trigger telescopes. Of primary interest here are the effects of the various coincidence conditions imposed on the light particle spectra measured with the scintillator array. All telescopes in the array have been summed together in order to obtain the best possible statistics. The errors depicted in the energy spectra are statistical. Positive detector angles imply the side of the reaction plane on which the scintillator array was placed. Negative angles imply the opposite side of the reaction plane.

A. 92 MeV/A ^{40}Ar+Au Inclusive Spectra

1. Light Particle (Scintillator Array) Inclusive Spectra

Light particle inclusive spectra (Z=1,2) have been measured for the reaction 92 MeV/A ^{40}Ar+Au at angles of 45, 67.5, and 90 degrees in the laboratory. Energy spectra for p, d, t and ^{3}He, ^{4}He are shown in Figures V-1;a&b, respectively. The solid curves in the figure correspond to

Figure V-1. Energy spectra of (a) p,d,t, and (b) ^{3}He,^{4}He from the reaction 92 MeV/A ^{40}Ar+Au. The angles measured are 45° (circles), 67.5° (squares), and 90° (double triangles) in the laboratory. The errors depicted are statistical. The solid lines correspond to a hydrodynamics model calculation and the dot-dashed lines correspond to a firestreak calculation as described in the text.

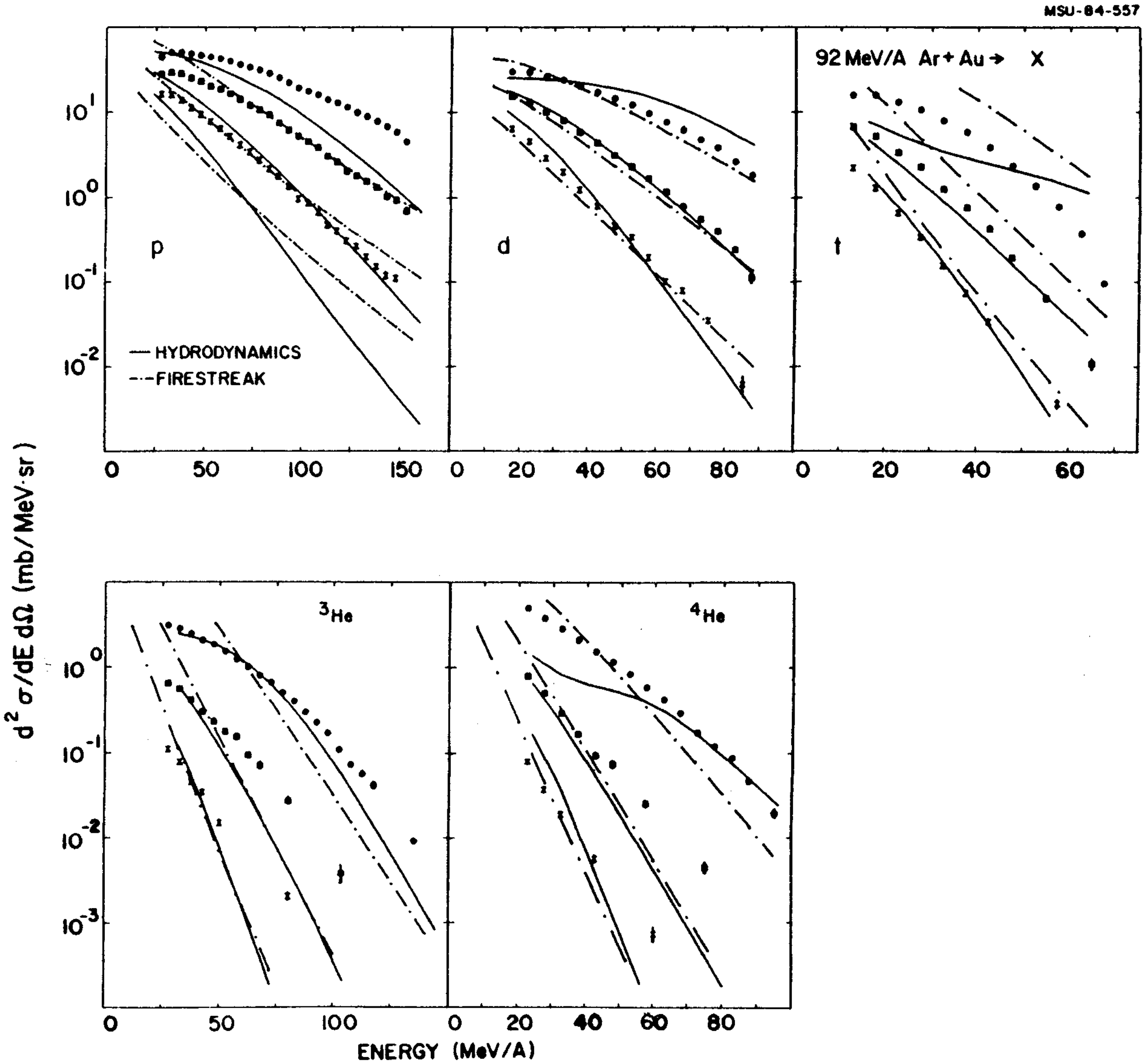
MSU-84-557
92 MeV/A Ar + Au → X
p
d
t
3He
4He
— HYDRODYNAMICS
-·-FIRESTREAK
$d^2\sigma/dE\,d\Omega$ (mb/MeV·sr)
10^1
10^0
10^{-1}
10^{-2}
10^{-3}
0
50
100
150
0
20
40
60
80
ENERGY (MeV/A)

Figure V-1

hydrodynamics (HD) calculations by Buchwald [Bu 84] with arbitrary normalizations for each light particle as follows: protons x10; deuterons x3.3; tritons x.13; ^{3}He x1; and ^{4}He x.33 . The HD results are azimuth and impact parameter averaged for impact parameters from 0 to 7 fm. The dot-dashed curves are firestreak (FS) calculations for the same system using the impact parameter with the maximum weight giving a firestreak with 82 nucleons and 34 protons at an impact parameter of 5 fm [We 84]. It is interesting to note that while neither calculation fits the proton spectra, both fit the deuteron spectra. The HD calculation tends to give a more realistic fit to the other spectra. This is especially true at the low energy end of the spectra where the FS calculation tends to overpredict the cross sections. The firestreak model assumes that the surfaces of the colliding nuclei are diffuse. The surface of each nucleus is divided into infinitesimal streaks parallel to the projectile direction. The projectile streaks follow straightline trajectories and interact with the target streaks only through completely inelastic collisions. The streaks are not allowed to broaden during the collision. The simplifying assumptions for the trajectories and interaction mechanism are valid at the relativistic energies for which the firestreak model was first proposed. At intermediate energies, ie. between 20 and 200 MeV/nucleon, these assumptions break down, causing the model to overpredict the low energy part of the spectra, particularly for particles of mass A>2.

2. Moving Source Parameterization

When considering a large volume of data it becomes useful to find a way to parameterize the whole set in terms of a few meaningful parameters. To that end, we have chosen to fit the light particle scintillator array spectra with what is commonly known as a single moving source parameterization. It has been shown that the high energy tails of light particle inclusive spectra can be explained in terms of emission from an excited source of light particles in thermal equilibrium [Go 77]. This source emits particles isotropically in its rest frame which is moving at approximately half the beam velocity. The energy spectra are also assumed to be isotropic in the source rest frame with a relativistic Maxwell-Boltzmann energy distribution in the rest frame [La 69] given by

$$\frac{d^2\sigma}{p^2dpd\Omega} = \frac{\sigma}{4\pi m^3} \frac{\exp(-E/\tau)}{2(\tau/m)^2\ K_1(m/\tau)+(\tau/m)K_0(m/\tau)}\ , \qquad (V-1)$$

where p and E are the momentum and total energy, respectively, of a particle in the source rest frame. K_1 and K_2 are MacDonald functions, also known as modified Bessel functions of the second kind. The double-differential cross sections are transformed into the laboratory frame using

$$\frac{d^2\sigma}{dEd\Omega} = pE'\frac{d^2\sigma}{p'^2dp'd\Omega'}\ , \qquad (V-2)$$

where $d^2\sigma/p'^2dp'd\Omega'$ is the moving source rest frame momentum distribution, p(p') is the particle lab (source rest frame) momentum, and E' is the source rest frame total energy of the particle expressed as

$$E' = \gamma_{m.s.}(E-\beta_{m.s.}p\cos\theta_{lab}), \qquad (V-3)$$

where

$$\gamma_{m.s.} = 1/(1-\beta_{m.s.}{}^2)^{1/2}. \qquad (V-4)$$

Here E and θ_{lab} are the total energy and angle in the lab, respectively. The moving source spectra are fit to the data using the method of least squares with three free parameters. The three fit parameters are σ, the total cross section, $\beta_{m.s.}$, the velocity of the moving source (usually expressed as the ratio to the beam velocity), and τ, the slope parameter, which is often referred to as the temperature of the source. The effect of the velocity parameter can be understood by considering that if the source velocity is zero, then the spectra at all angles will be identical, ie., isotropic emission as in Figure V-2;a. If the source is moving along the beam direction, the spectra will no longer appear isotropic, but will have the general appearance of Figure V-2;b. The source velocity is then a measure of the change in the cross section as a function of angle, ie. the source velocity is related to the slope of the angular distribution $d\sigma/d\Omega$. The inverse temperature reflects the slope of the spectra in the high energy tails. A negative energy shift is applied to the data before fitting to take into account the boost acquired

Figure V-2. Schematic representation of the energy spectrum of particles emitted from a thermally equilibrated source (a) in the source's rest frame and (b) in the lab frame with the source moving in the forward direction.

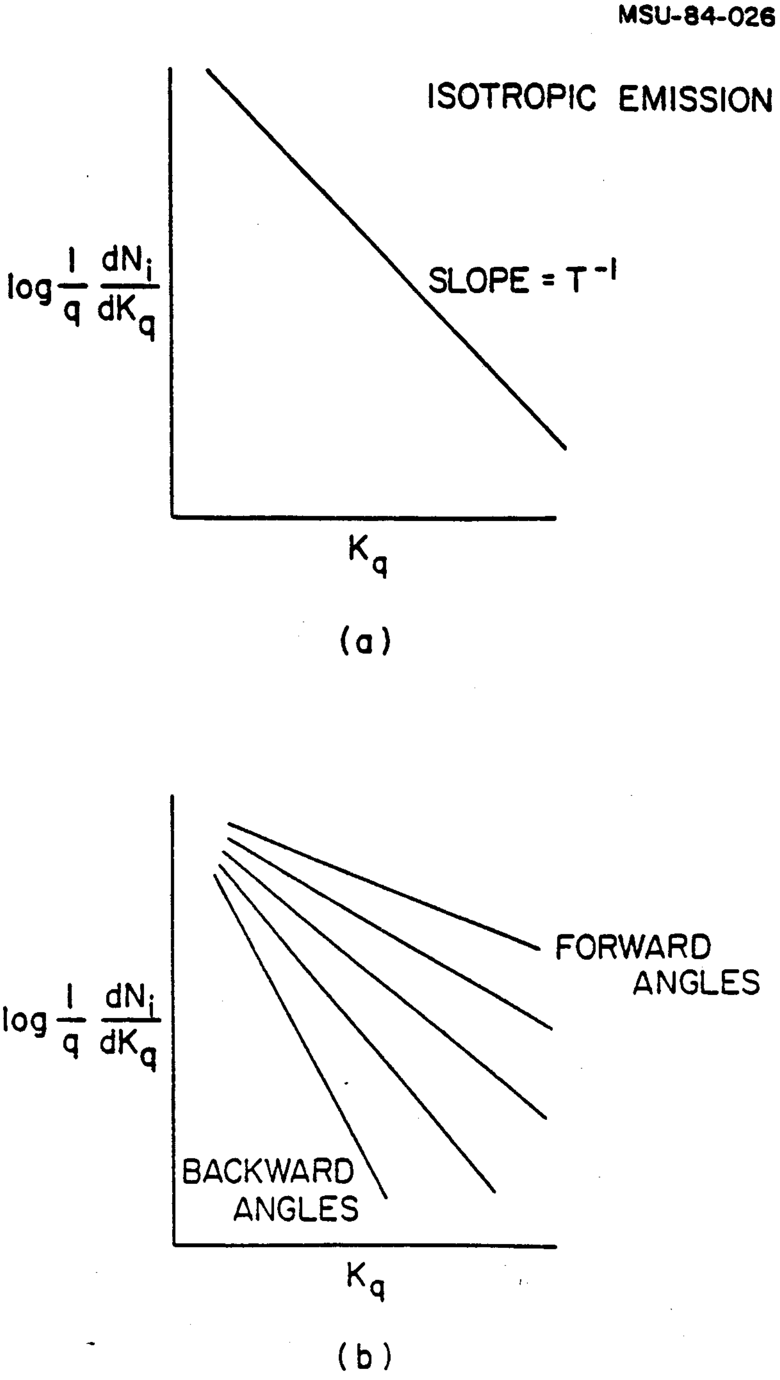
MSU-84-026
ISOTROPIC EMISSION
$\log \frac{1}{q} \frac{dN_i}{dK_q}$
SLOPE = T^{-1}
K_q
(a)
$\log \frac{1}{q} \frac{dN_i}{dK_q}$
FORWARD ANGLES
BACKWARD ANGLES
K_q
(b)

Figure V-2

by the particle in the coulomb field of the target. The resulting moving source fit spectra are then shifted up in energy by the same amount for comparison with the measured spectra. The coulomb shifts used in the analysis of the Au target data were 10 and 18 MeV for Z=1 and 2, respectively. For the Al target data, shifts of 4 and 8 MeV were used for Z=1 and 2, respectively.

The inclusive spectra for p, d, t, and ^{3}He,^{4}He are shown with single moving source fits (solid curves) in Figures V-3;a&b, respectively. The spectra were not fit for energies below 50 MeV/nucleon to eliminate contributions from target emission. All angles were included in the fits. The values of the parameters extracted from the inclusive spectra are given in Table V-1 and agree with the systematics of the moving source parameterization as shown in Figure V-4 [We 82].

3. Coalescence Model

The dot-dashed curves in Figure V-3 are the results of coalescence model calculations for the light composite fragment cross sections. A coalescence relation given by

$$\frac{d^2\sigma(Z,N,E_A)}{dE_A d\Omega_A} = C \left[\frac{d^2\sigma(1,0,E)}{dE d\Omega}\right]^A, \quad (V-5)$$

where

$$C = \left(\frac{N_p + N_t}{Z_p + Z_t}\right)^N \frac{A^{-1}}{N!Z!} \frac{1}{\sigma_0} \left[\frac{4\pi P_0{}^3/3}{[p\sqrt{(p^2+m^2)}]}\right]^{A-1} \quad (V-6)$$

Figure V-3. Energy spectra of p,d,t,^{3}He, and ^{4}He from the reaction 92 MeV/A ^{40}Ar+Au. The solid lines correspond to moving source fits as described in the text. The dot-dashed lines correspond to coalescence model calculations.

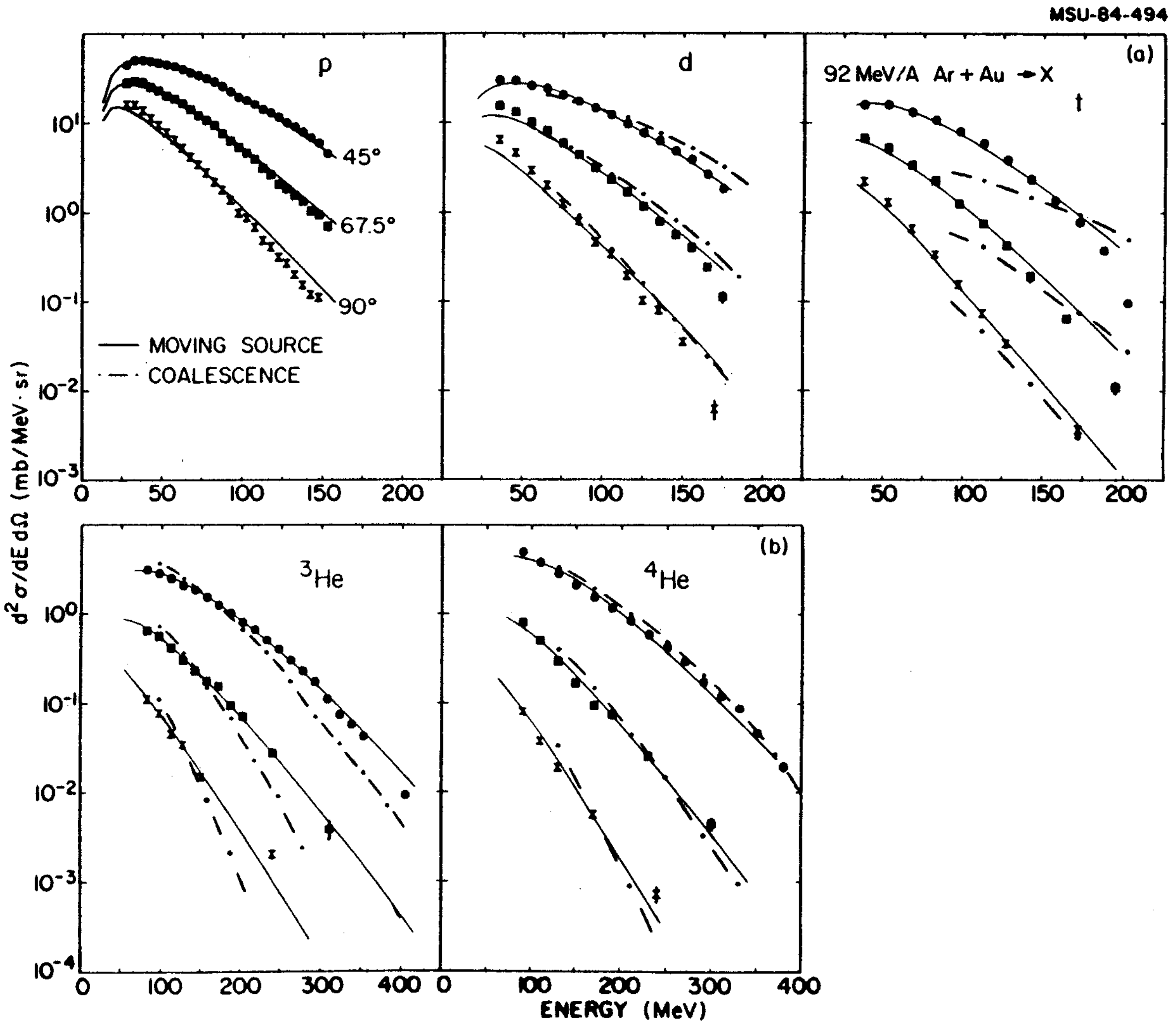
MSU-84-494
p
d
(a)
92 MeV/A Ar + Au → X
t
45°
67.5°
90°
MOVING SOURCE
COALESCENCE
(b)
^{3}He
^{4}He
$d^2\sigma/dE\,d\Omega$ (mb/MeV·sr)
10^1
10^0
10^{-1}
10^{-2}
10^{-3}
10^{-4}
0
50
100
150
200
300
400
ENERGY (MeV)

Figure V-3

TABLE V-1

MOVING SOURCE PARAMETERS FOR 92 MeV/A Ar+Au (INCLUSIVE)

Particle	Temperature τ (MeV)	Cross section σ_0 (mb)	Velocity β (c)
PROTON	21.4±0.2	22600.±246.	0.205±0.002
DEUTERON	21.6±0.2	13600.±223.	0.181±0.003
TRITON	19.5±0.3	7827.±217.	0.152±0.002
^{3}He	29.4±0.2	2540.± 35.	0.218±0.002
^{4}He	25.9±0.3	3960.±111.	0.194±0.002

Figure V-4. The variation with incident energy above the barrier of:(a) the p,d,t,^{4}He cross sections associated with a mid-rapidity source (the solid lines are to guide the eye, and the dashed line is the fireball model prediction for protons);(b) the extracted temperatures from the moving source compared with fireball description (dashed) and a Fermi gas model (solid) for equal participation from projectile and target nucleus;(c) the moving source velocities compared with the fireball (dashed) and equal participation models (solid).

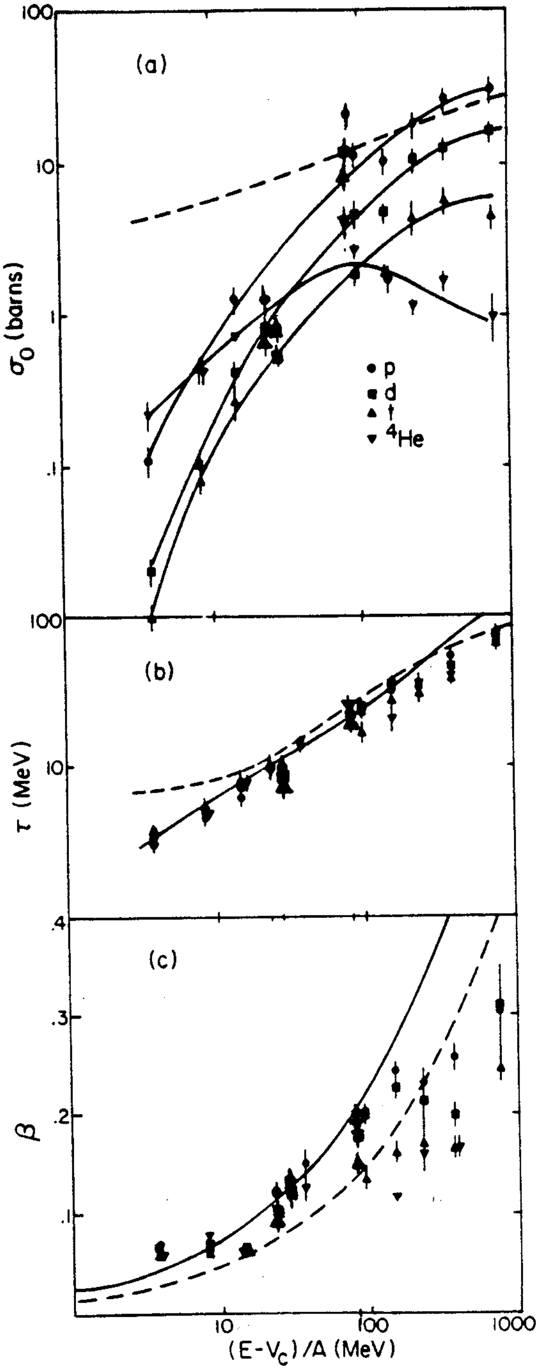
(a)
σ0 (barns)
100
10
1
.1
p
d
t
4He
(b)
τ (MeV)
100
10
(c)
β
.4
.3
.2
.1
10
100
1000
(E-Vc)/A (MeV)

was used to extract the coalescence radii from fits of the proton inclusive spectra to the composite fragment spectra. In Eqn. V-5 $d^2\sigma(Z,N,E_A)/dE_A d\Omega_A$ is the double differential cross section of nuclei composed of Z protons and N=A-Z neutrons. N_p, N_t are the number of neutrons in the projectile and target nuclei, respectively, and Z_p, Z_t are the number of protons in the projectile and target nuclei, respectively. The value of σ_0 is taken to be the total reaction cross section. P_0 is the coalescence radius and p and m are the relativistic momenta and mass for the protons. The coalescence radius in momentum space, was the single free parameter used in the fits. The deuteron and alpha spectra are well described by the coalescence model. The model does not fit the triton and ^{3}He spectra very well, although, the coalescence radii are still reasonable. The coalescence radii are summarized in Table V-2. It is possible to relate the coalescence radii to the size of the fireball at the freeze-out density V through the parameter $\bar{p}_0$ given as [Me 78]

$$(P_0{}^3)^{A-1} = A^3 \frac{2s+1}{2^A} (\bar{p}_0{}^3)^{A-1} \qquad \text{(V-7)}$$

This parameterization removes explicitly the spin alignment and phase factors from the coalescence radius. With the freeze-out density given by [Le 79]

$$V = (N!Z!)^{1/(A-1)} (3h^3/4\pi\bar{p}_0{}^3) \qquad \text{(V-8)}$$

and the volume of the equivalent sphere taken to be

TABLE V-2

COALESCENCE MODEL PARAMETERS

	P_0 (MeV/fm)	$\tilde{p}_0$ (MeV/fm)	V (fm^3)	R (fm)
92 MeV/A ^{40}Ar+Au (a)				
^{2}H	165	90	615	5.28
^{3}H	139	101	629	5.32
^{3}He	155	113	450	4.76
^{4}He	171	147	229	3.80
100 MeV/A ^{16}O+Au (b)				
^{2}H		87		5.5
^{3}H		111		3.8
^{3}He		115		3.8
^{4}He		142		2.9

(a) Present work.
(b) Parameters from Auble, et al. [Ab 83]

$$V=4/3(\pi R^3) \tag{V-9}$$

the radii at freeze-out were obtained and are presented in Table V-2. Included in Table V-2 are the coalescence model parameters obtained by Auble, et al. [Ab 83] for the reaction 100 MeV/A ^{16}O+Au. The parameters obtained in the present experiment are in fair agreement with the ^{16}O induced results.

4. Intermediate Rapidity Fragment Inclusive Spectra

The inclusive fragment spectra ($3 \leq Z \leq 7$) for the Intermediate Rapidity Fragment (IRF) trigger at -30 degrees are shown in Figure V-5. The data have been plotted as invariant cross sections as a function of the total fragment momentum. The lines are to guide the eye. The similarity of the shapes of the cross sections is an indication that a single reaction mechanism is responsible for the production of the various fragments. This phenomenon has been examined in detail by Jacak, et al. [Ja 83]. It was shown that the inclusive fragment spectra from 30 to 90 degrees in the laboratory frame could be explained with the assumption of fragment emission from a single intermediate rapidity thermal source. Temperatures and velocities extracted from the intermediate mass fragment spectra using the single moving source parameterization were similar to parameters found for inclusive light particle spectra measured in the same experiment.

Figure V-5. Invariant cross section plots versus total momentum for intermediate rapidity fragments in the IRF trigger at -30° from the reaction 92 MeV/A ^{40}Ar+Au. The lines are to guide the eye.

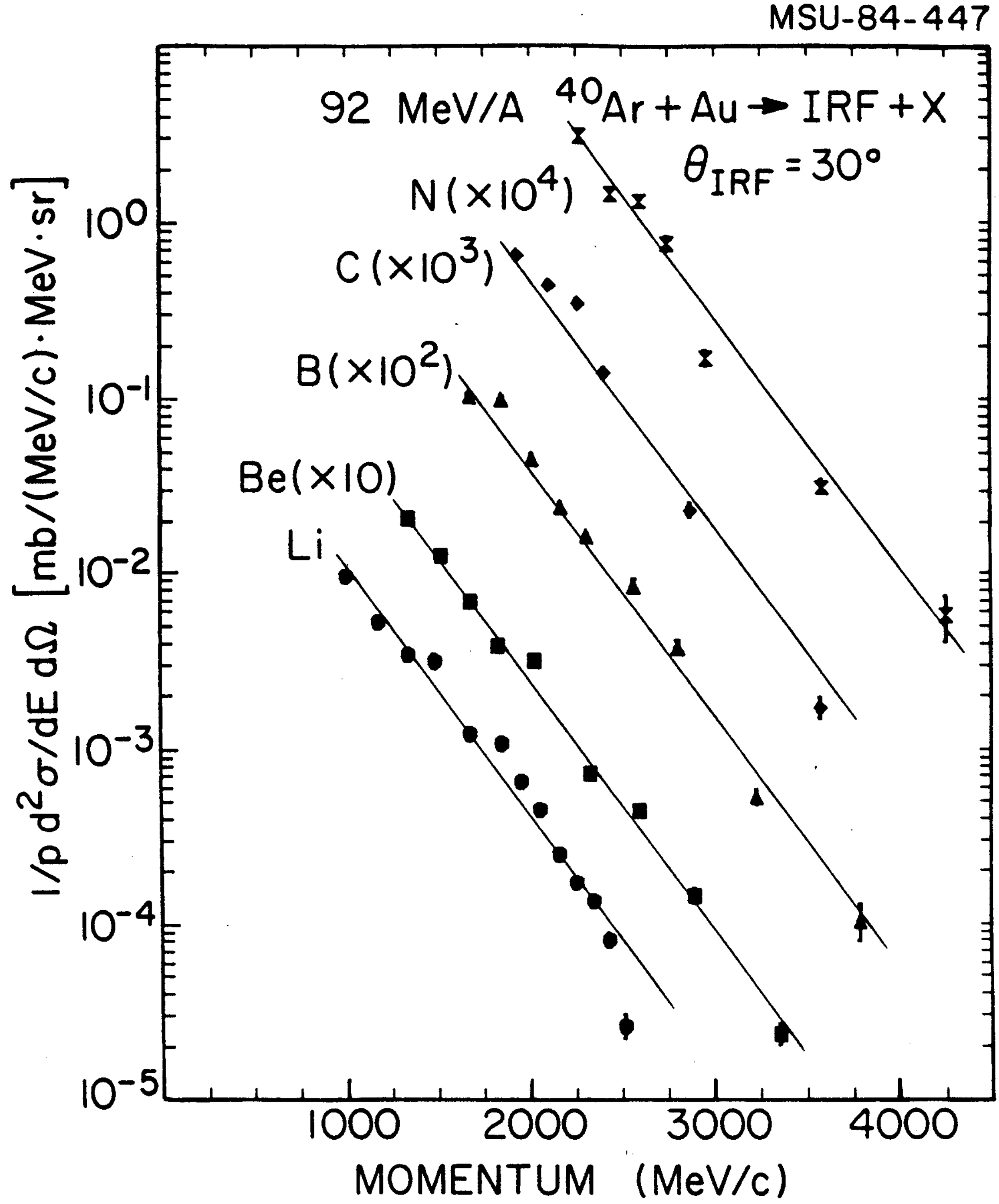
MSU-84-447
92 MeV/A ^{40}Ar + Au → IRF + X
θ_{IRF} = 30°
N (×10^4)
C (×10^3)
B (×10^2)
Be (×10)
Li
1/p d$^2\sigma$/dE dΩ [mb/(MeV/c)·MeV·sr]
10^0
10^{-1}
10^{-2}
10^{-3}
10^{-4}
10^{-5}
1000
2000
3000
4000
MOMENTUM (MeV/c)

Figure V-5

Figure V-6. Projectile-like fragment cross sections for the PLF trigger at -13° plotted versus the fragment velocity over the projectile velocity from the reaction 92 MeV/A ^{40}Ar+Au.

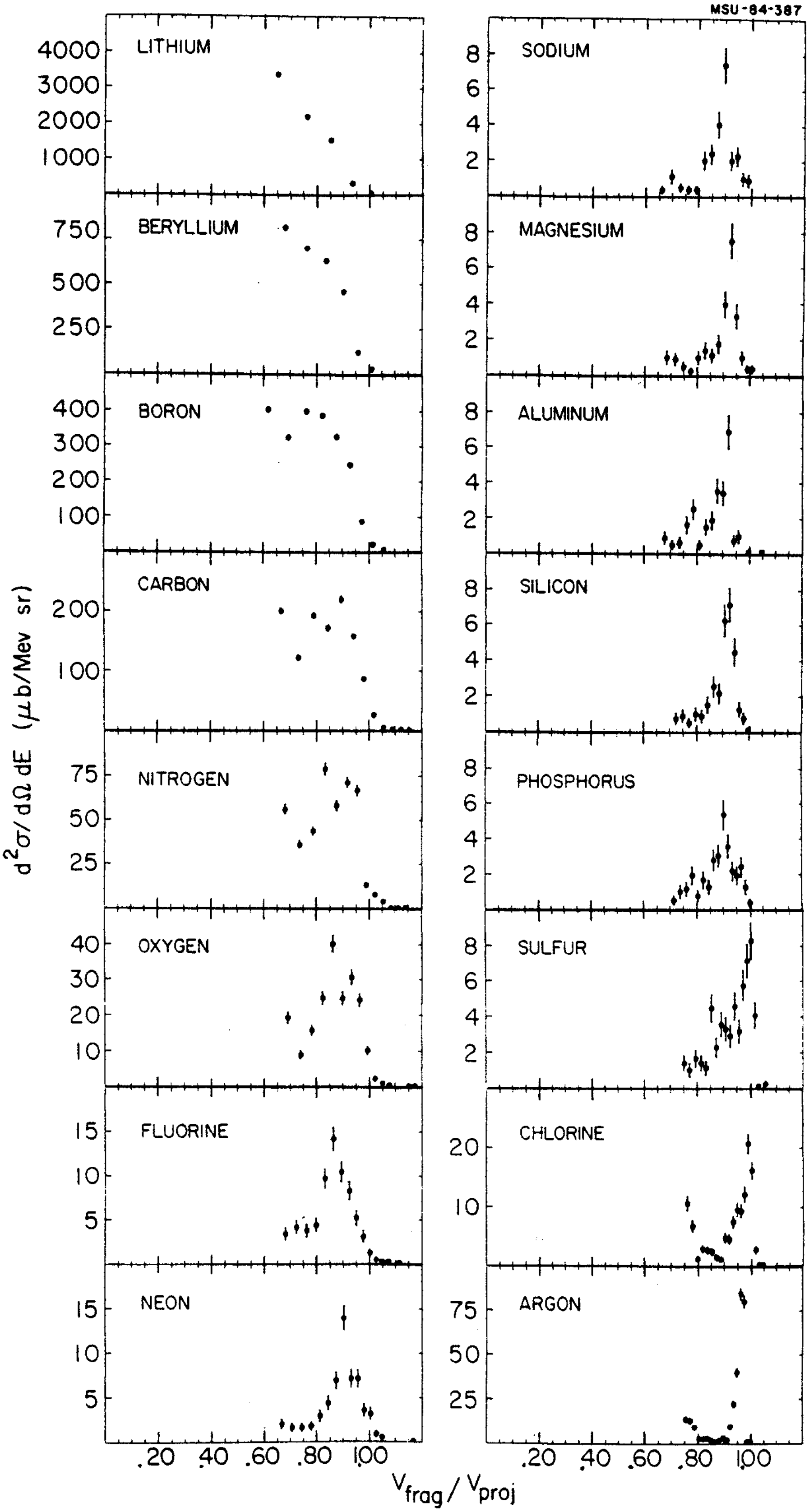
MSU-84-387
LITHIUM
BERYLLIUM
BORON
CARBON
NITROGEN
OXYGEN
FLUORINE
NEON
SODIUM
MAGNESIUM
ALUMINUM
SILICON
PHOSPHORUS
SULFUR
CHLORINE
ARGON
4000
3000
2000
1000
750
500
250
400
300
200
100
200
100
75
50
25
40
30
20
10
15
10
5
15
10
5
8
6
4
2
20
10
75
50
25
$d^2\sigma/d\Omega\,dE$ (μb/Mev sr)
.20
.40
.60
.80
1.00
V_{frag}/V_{proj}

Figure V-6

5. Projectile-Like Fragment Inclusive Spectra

The inclusive double differential cross sections for the Projectile-Like Fragment (PLF) trigger at -13 degrees are shown in Figure V-6. Cross sections are shown for fragments with ($3 \leq Z \leq 18$) as a function of the ratio of the fragment velocity to the incident projectile velocity. It is possible to observe evidence of three distinct reaction mechanisms in the PLF fragment spectra - projectile fragmentation, thermal emission, and few nucleon transfer.

Projectile fragmentation has been described as an interaction occurring for large impact parameters in which the incoming projectile nucleus becomes excited upon contact with the target nucleus. The projectile velocity is not appreciably reduced by the collision as it would be for a collision at a smaller impact parameter. The excited projectile either breaks up near the target nucleus before equilibration of the excitation energy or decays in flight after thermal equilibrium is established. The momentum distribution for a fragment emitted from a decaying projectile has been described by Goldhaber [Go 74] using a gaussian distribution $\exp(-p^2/2\sigma^2)$, where σ is the momentum width of the distribution. For a fragment with K nucleons emitted from a projectile with A nucleons the momentum width is given as

$$\sigma^2 = \sigma_0{}^2 K(A-K)/(A-1), \qquad \text{(V-9)}$$

where $\sigma_0 \approx 100$ MeV/c. The value of σ_0 can be related to the fermi momentum of the nucleons in the projectile nucleus by

$\sigma_0 = p_f/\sqrt{5}$. Projectile fragmentation has been observed in Ar induced reactions on Au at 213 MeV/nucleon by Viyogi, et al. [Vi 79] as well as at energies below 100 MeV/nucleon in Ar, C, and N induced reactions [Mo 81, Bo 83, Gu 83, Ra 83]. The velocity distributions in Figure V-6 which most clearly show projectile fragmentation are those for the oxygen through phosphorus fragments. The observed peaks appear gaussian in shape with centroids between 85 and 90 percent of the projectile velocity. The shift in velocity down from the projectile velocity can in part be accounted for by the loss in kinetic energy of the emitting system due to the binding energy associated with the emitted fragment.

The Li and Be fragment velocity distributions are primarily exponential in shape with only slight shoulders to indicate the possible presence of projectile fragmentation phenomena. The exponential fall-off of the distributions is consistent with the assumption of emission from a thermal source, as discussed in section A.4. The B, C, and N velocity distributions show evidence of both fragmentation and thermal emission.

The few nucleon transfer reaction mechanism involves the exchange between the target and projectile nuclei of one or several nucleons. The fragment velocity distributions for the transfer process are characterized by narrow peaks centered at the beam velocity. The narrow peak widths can be attributed to the limited range of energies of the available excited states into which the exchanged nucleons can be transferred. The sulfur, chlorine, and argon fragment velocity distributions of Figure V-6 appear to be dominated by the few nucleon transfer mechanism as shown by the markedly narrower widths and higher velocities relative to the oxygen through phosphorus distributions. The apparent sudden change from fragmentation to transfer reactions at sulfur has been examined more closely by Borrel, et al. [Bo 83] and Rami, et al. [Ra 84] in Ar induced reactions at 44 and 27.6 MeV/A, respectively. They find that the mechanism changes from fragmentation to few nucleon transfer between ^{35}S and ^{36}S. Interestingly, formation of a fragment smaller than ^{36}S from ^{40}Ar would require the transfer to the target of a fragment larger than an alpha particle. The argon velocity distribution undoubtedly contains a large component from elastic scattering. The grazing angle for the 92 MeV/nucleon ^{40}Ar+Au reaction is approximately 3 degrees.

These three reaction mechanisms need to be taken into account when attempting to understand the light particle coincidence data. For coincidences with fragments with $Z\leq7$, the contributions from thermal sources are non-negligible. A picture which includes both fragmentation and thermal emission is necessary. For coincidences with fragments with $8\leq Z\leq15$, a fragmentation picture should suffice. There will undoubtedly still be contributions to the light particle spectra from emission from a moving thermal source as well as target evaporation. Coincidence events with the highest three Z fragments might be expected to yield light particles originating primarily from target evaporation.

6. Light Particle (90°) Inclusive Spectra

The inclusive light particle spectra (Z=1,2) for the Light Particle (LP) trigger at -90 degrees are shown in Figure V-7. The spectra are plotted as invariant cross sections as a function of the total particle momentum. The lines are to guide the eye. The slightly steeper slopes at the low energy end of the d and t spectra are associated with evaporation from the colder target remnant. For the LP triggered light particle coincidence spectra, the target evaporation portion of the LP spectra has been discarded. A lower cut at an energy of 20 MeV/nucleon was imposed on the LP spectra, corresponding to a momentum of approximately 200 MeV/c/nucleon. Inclusive spectra measured at 90 degrees in the scintillator array were in good agreement with the LP spectra.

B. 92 MeV/A ^{40}Ar+Au Coincidence Spectra

1. Momentum Conservation Model

The interpretation of coincidence spectra has as an inherent hazard the possibility of assigning special significance to phenomena which had their origins in simple conservation laws. It is, of course, not possible to

Figure V-7. Invariant cross section plots versus total momentum for p,d,t, and ^{4}He in the LP trigger at -90° from the reaction 92 MeV/A ^{40}Ar+Au. The lines are to guide the eye.

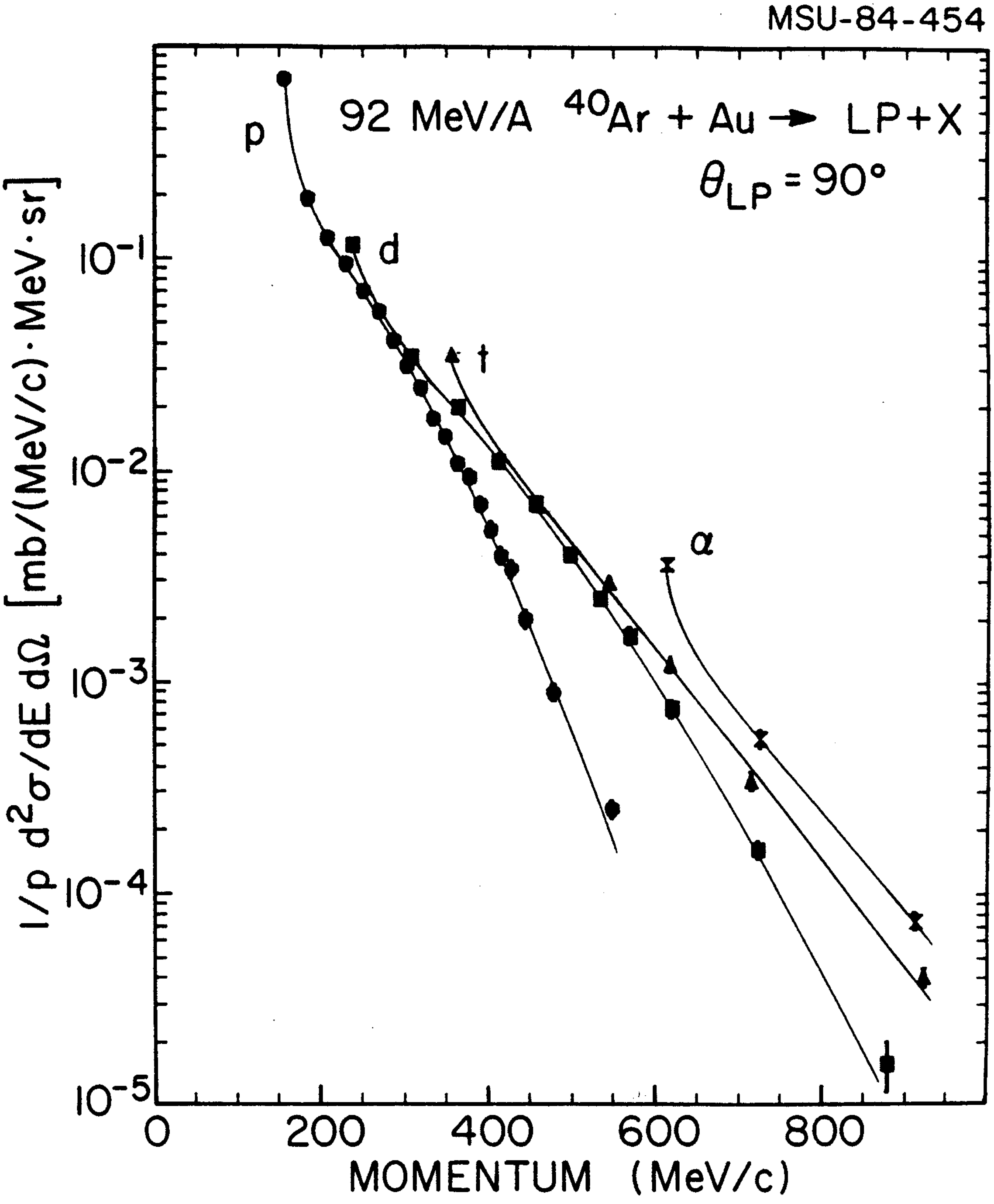
MSU-84-454
92 MeV/A ^{40}Ar + Au → LP+X
θ_{LP} = 90°
p
d
t
α
1/p d^{2}σ/dE dΩ [mb/(MeV/c)·MeV·sr]
10^{-1}
10^{-2}
10^{-3}
10^{-4}
10^{-5}
0
200
400
600
800
MOMENTUM (MeV/c)

Figure V-7

perfectly model a nuclear reaction, even for conservation of momentum, because of the simplifying assumptions which must be made. It is, however, useful to attempt to understand the coincidence results from the perspective of the current level of understanding of the inclusive results, and do so within the framework of the conservation laws. The calculation which has been performed assumes that two coincident particles are emitted sequentially from a single moving source as described in section A.1. In reality, more than two particles are emitted from any collision violent enough to create an excited thermal source. The assumption of two particle emission is a minimal requirement. Emission of a third particle would be likely to reduce the correlations seen in the two particle calculation due to the increased number of degrees of freedom. From a knowledge of the momentum of the first particle, it is possible to calculate the reduction in excitation energy of the source and its recoil momentum. The second particle is then emitted from the cooled, recoiling source. Since it is not possible to know which particle was emitted first, both time sequences are combined to give the final coincidence cross section. The initial source parameters used in the calculations were those parameters extracted from the inclusive light particle spectra for the particle of interest. The size of the emitting source was chosen to correspond to the size of the fireball formed at the most probable impact parameter. This gave source sizes of N=82 for the Ar+Au reaction and N=18 and 38 for the C+Al and C+Au reactions, respectively. The normalizations of the final calculated coincidence cross sections were obtained using cross sections from moving source fits to the inclusive spectra of both emitted particles. The intermediate mass fragment cross sections were provided by Jacak [Ja 84]. The spectra were further normalized by dividing by the reaction cross section. There were no other free parameters in the Ar+Au normalizations. Fragment cross sections were not available for the 30 MeV/A reactions. The calculated spectra for the 30 MeV/A reactions were arbitrarily normalized in order to compare the shapes of the distributions. A detailed presentation of the calculation is given in Appendix A.

All of the coincidence spectra to be presented here have been divided by the solid angle of the trigger detector. The limits imposed on the integration of the trigger particle spectra are those imposed by the lower and upper energy cutoffs of the detector, except where noted. The solid curves in the figures are moving source fits to the data with energy and angle cuts as given in the presentations of the inclusive results. Exceptions will be pointed out when they occur. The dotted curves in the figures are momentum conservation calculations as outlined above.

2. Light Particle - IRF Coincidence Spectra

Light particle spectra for coincidences between p, d, t, ^{3}He and ^{4}He at 45, 67.5, and 90 degrees and intermediate rapidity fragments ($3 \leq Z \leq 7$) at -30 degrees are shown in Figures V-8-12. The inclusive light particle spectra have been included in the figures for comparison with the coincidence spectra. The coincidence spectra have the same general features as the inclusive spectra for all measured light particle - intermediate rapidity fragment combinations. the momentum conservation calculation (dotted lines) for the proton spectra of Figure V-8 are in overall agreement with the data. Differences between the calculation and the data are seen to occur for low proton energies and for the normalizations of the Be and B triggered spectra. Excessive emphasis should not be placed on the normalizations of the calculation. The discrepancies at low energies can be understood as an overestimate of the calculated recoil velocity of the source. The trigger fragment is assumed to be emitted to -30 degrees causing the source to recoil. The perpendicular component of the recoil velocity makes the calculated light particle spectra between +45 and +90 degrees slightly less steep because the source now has a velocity component directed toward that side of the reaction plane. The parallel component of the recoil momentum reduces the original velocity of the source and causes the calculated spectra to become more isotropic. The effect of the source recoil on the calculated spectra is

Figure V-8. (a)Proton inclusive energy spectra and proton coincidence spectra for IRF trigger fragments (b)lithium, (c)beryllium, (d)boron, (e)carbon, and (f)nitrogen from the reaction 92 MeV/A ^{40}Ar+Au. The trigger fragment angle was -30°. The solid and dotted lines are moving source fits and momentum conservation calculations, respectively, as described in the text.

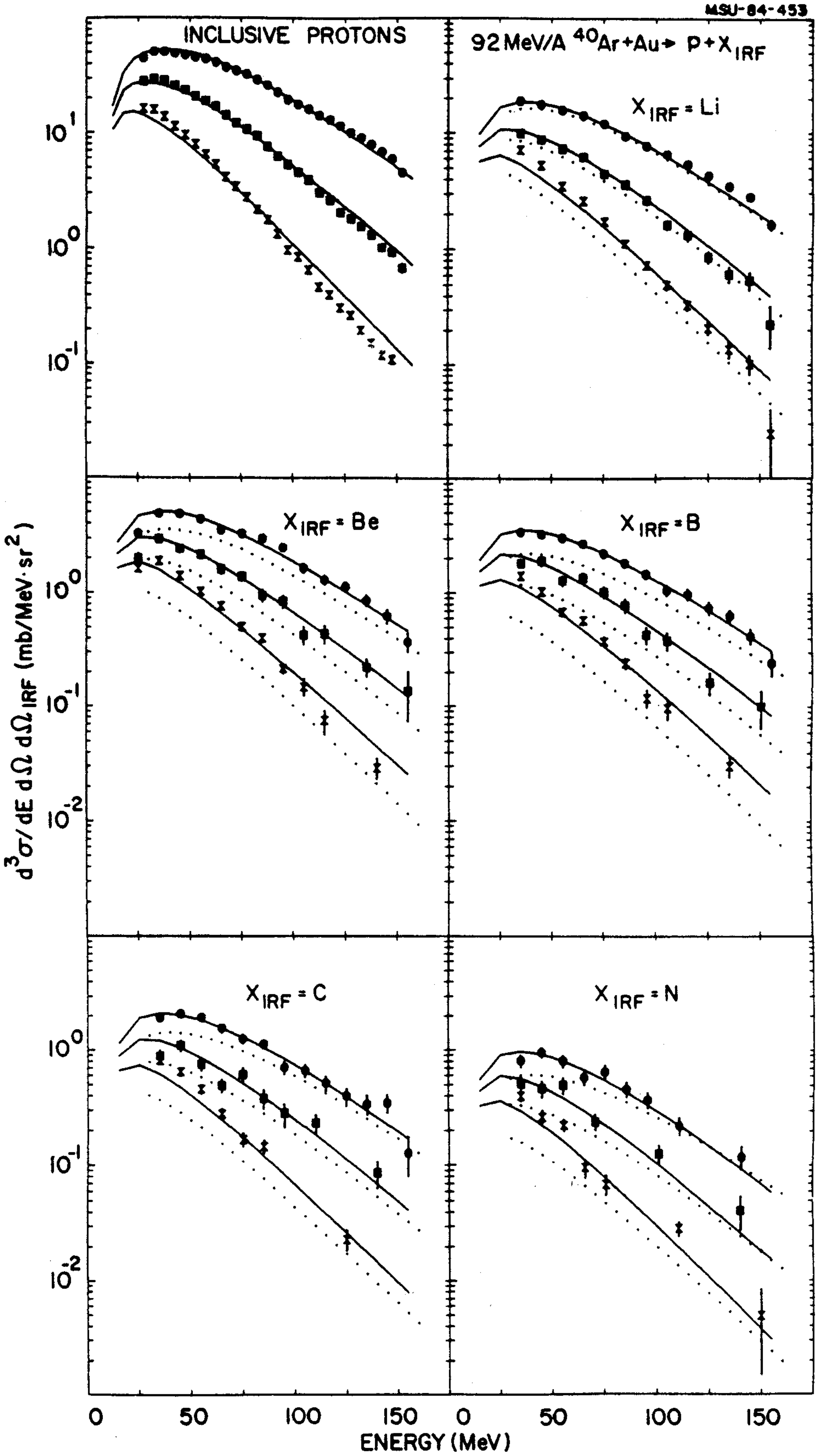
MSU-84-453
INCLUSIVE PROTONS
92 MeV/A 40Ar+Au→ P+X IRF
X IRF = Li
X IRF = Be
X IRF = B
X IRF = C
X IRF = N
d3σ/dE dΩ dΩ IRF (mb/MeV·sr2)
10^1
10^0
10^-1
10^-2
0
50
100
150
ENERGY (MeV)

Figure V-8

Figure V-9. Same as Figure V-8 for deuterons.

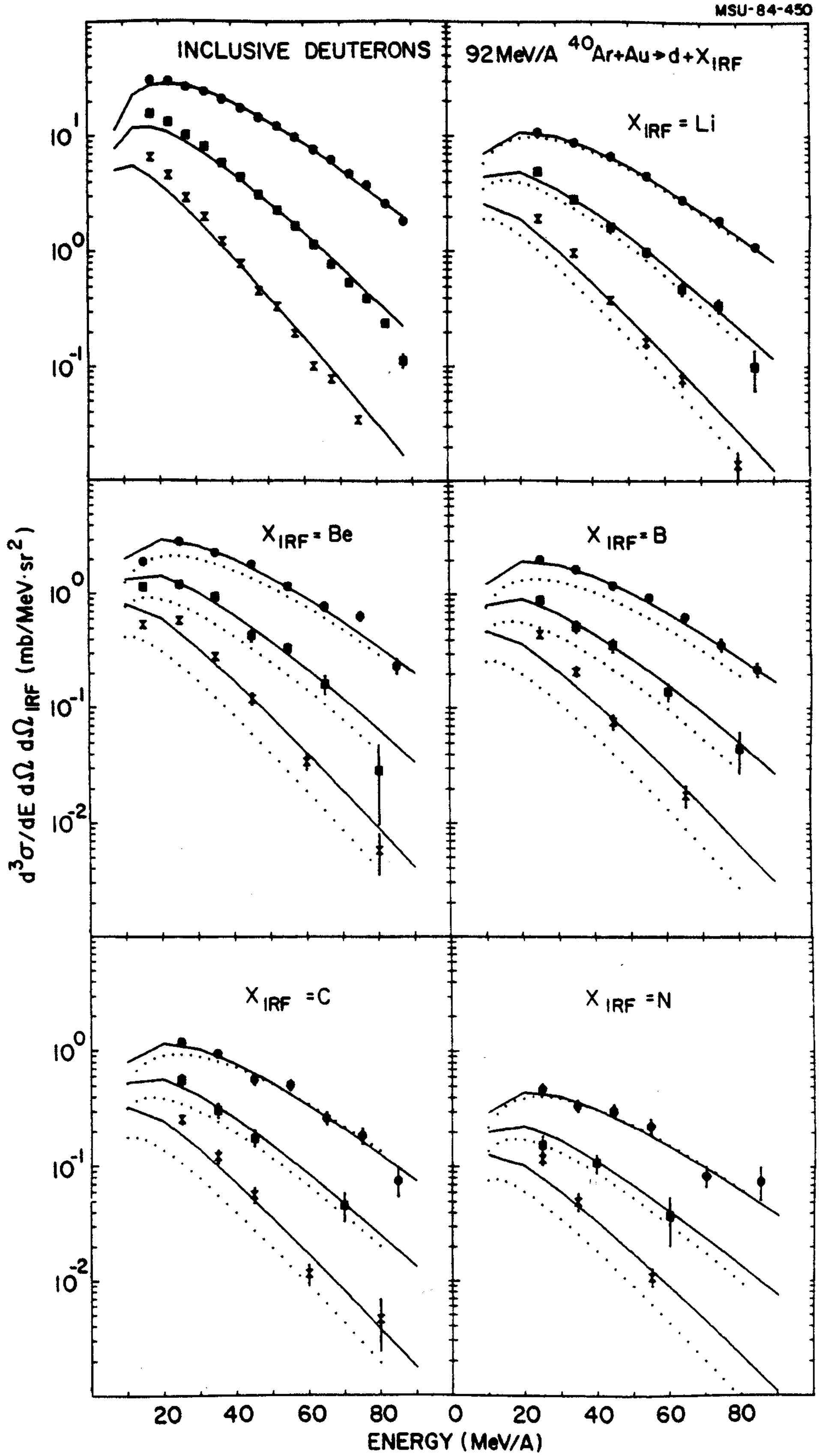
MSU-84-450
INCLUSIVE DEUTERONS
92MeV/A ^{40}Ar+Au→d+X$_{IRF}$
X$_{IRF}$ = Li
X$_{IRF}$ = Be
X$_{IRF}$ = B
X$_{IRF}$ = C
X$_{IRF}$ = N
$d^3\sigma/dE\,d\Omega\,d\Omega_{IRF}$ (mb/MeV·sr^2)
10^1
10^0
10^{-1}
10^{-2}
20
40
60
80
0
ENERGY (MeV/A)

Figure V-9

Figure V-10. Same as Figure V-8 for tritons.

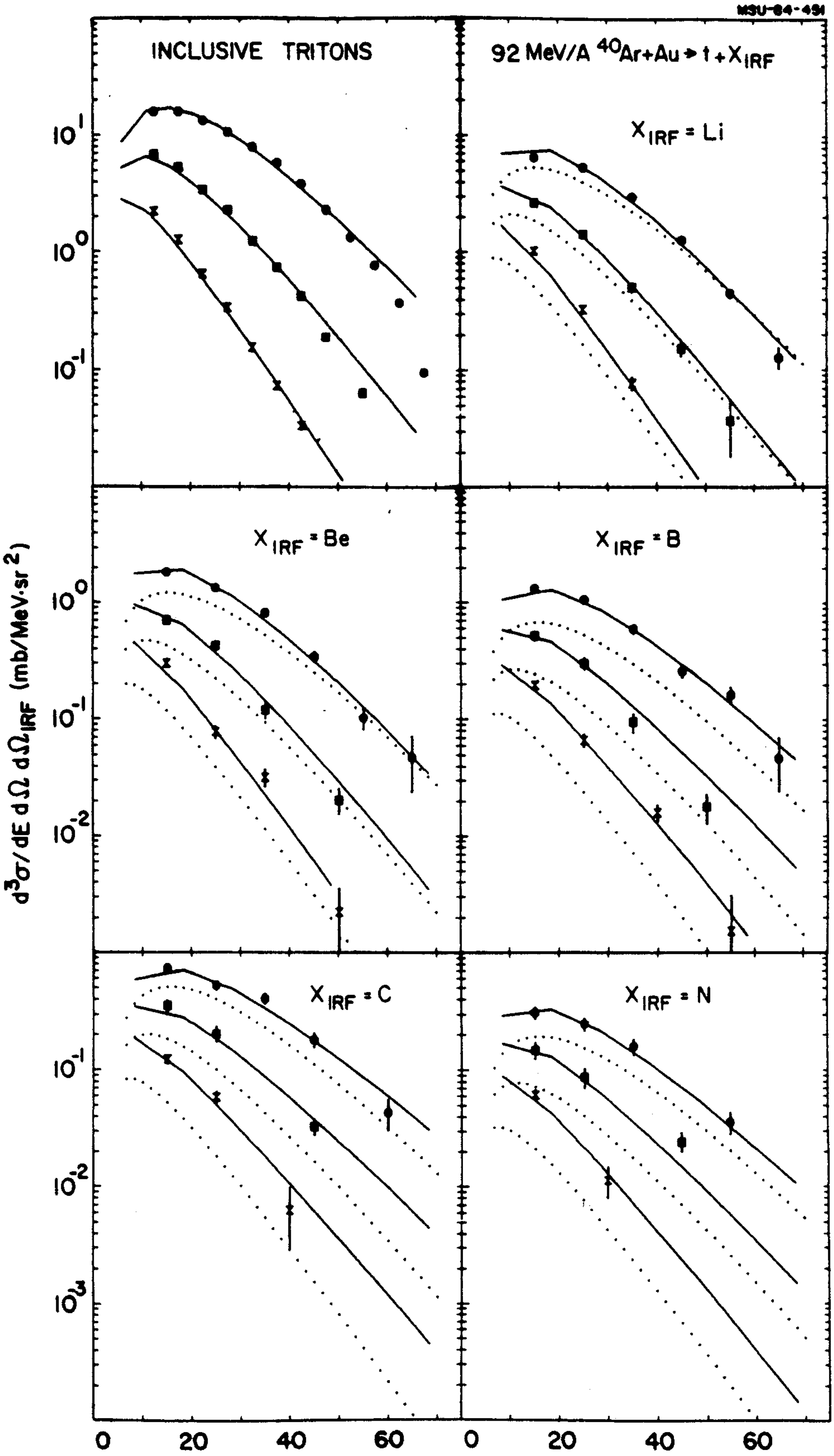
MSU-84-491
INCLUSIVE TRITONS
92 MeV/A ^{40}Ar+Au → t + X_{IRF}
X_{IRF} = Li
X_{IRF} = Be
X_{IRF} = B
X_{IRF} = C
X_{IRF} = N
$d^3\sigma/dE\,d\Omega\,d\Omega_{IRF}$ (mb/MeV·sr^2)
10^1
10^0
10^{-1}
10^{-2}
10^{-3}
0
20
40
60
ENERGY (MeV/A)

Figure V-10

Figure V-11. Same as Figure V-8 for ^{3}He.

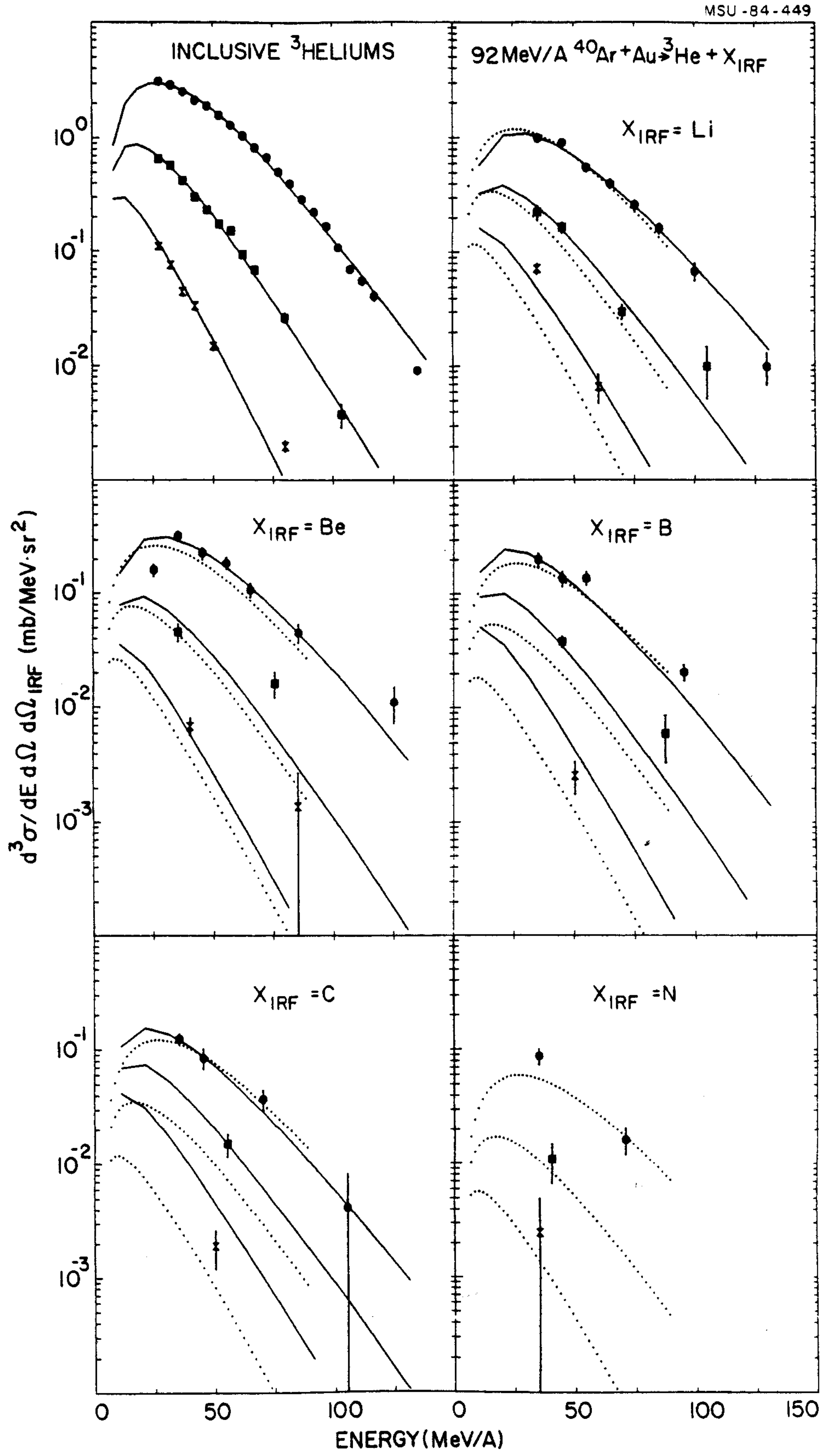
MSU-84-449
INCLUSIVE ^{3}HELIUMS
92 MeV/A ^{40}Ar + Au → ^{3}He + X_{IRF}
X_{IRF} = Li
X_{IRF} = Be
X_{IRF} = B
X_{IRF} = C
X_{IRF} = N
$d^3\sigma/dE\,d\Omega\,d\Omega_{IRF}$ (mb/MeV·sr^2)
10^0
10^{-1}
10^{-2}
10^{-3}
0
50
100
150
ENERGY (MeV/A)

Figure V-11

Figure V-12. Same as Figure V-8 for ^{4}He.

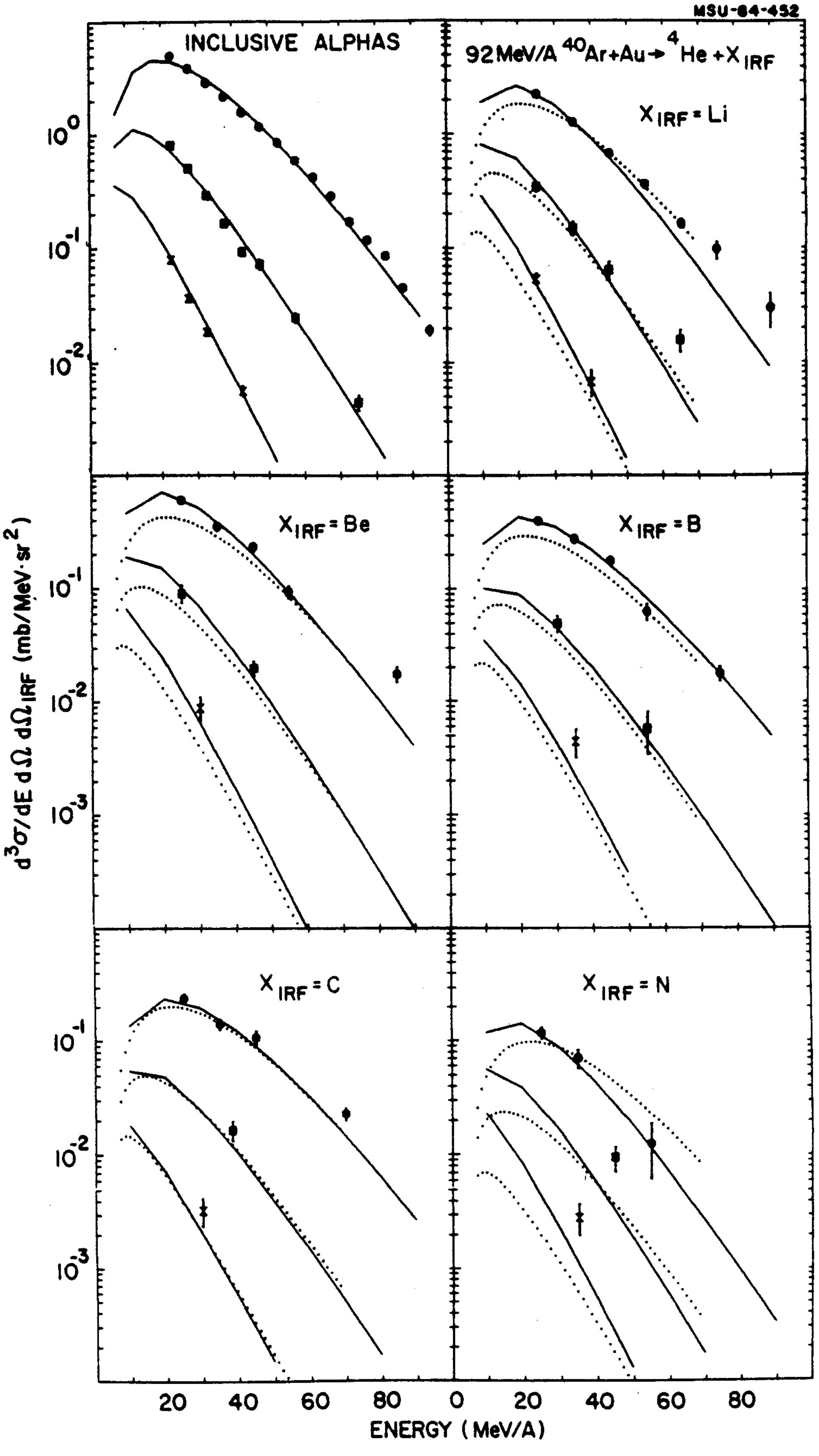
MSU-84-452
INCLUSIVE ALPHAS
92MeV/A ^{40}Ar+Au→ ^{4}He + X$_{IRF}$
X$_{IRF}$ = Li
X$_{IRF}$ = Be
X$_{IRF}$ = B
X$_{IRF}$ = C
X$_{IRF}$ = N
10^0
10^{-1}
10^{-2}
10^{-3}
d^{3}σ/dE dΩ dΩ$_{IRF}$ (mb/MeV·sr^2)
20
40
60
80
0
ENERGY (MeV/A)

Figure V-12

quite small. Any effect in the data is apparently even smaller.

The extracted moving source fit parameters for the IRF triggered light particle coincidence spectra are tabulated in Table V-3. the temperatures and velocities are plotted in Figures V-13;a&c, respectively, as ratios to the inclusive values. Note, the points plotted for fragment masses of 1 and 2 correspond to coincidences with the LP trigger and will be discussed later in the chapter.

Figure V-13;a shows that the extracted coincidence spectra temperatures tend to be slightly higher than the inclusive temperatures (about 5 percent). There does not appear to be any significant variation in this parameter over the range of trigger fragments measured. Figure V-13;c shows that the extracted coincidence spectra velocities tend to be lower than the inclusive velocities by about 10 percent. There may be some indication of a decrease in the velocity parameter with increased trigger fragment mass. There seems to be no significant dependence of the temperature and velocity parameters on the particular type of light particle measured. The apparent differences between the ^{3}He parameters and those of the other light isotopes may be due to the lower statistics of the ^{3}He spectra.

The slightly lower apparent velocities for the coincidence spectra relative to the inclusive spectra may be due to the fact that the 45 degree angle was included in all

TABLE V-3

MOVING SOURCE PARAMETERS FOR 92 MeV/A Ar+Au (IRF TRIGGER)

Particle	Trigger IRF	Temperature τ (MeV)	Cross section σ_0 (mb)	Velocity β (c)
PROTON	LITHIUM	23.0±0.6	8351.±192.	0.188±0.004
	BERYLLIUM	23.6±0.5	2312.± 62.	0.180±0.003
	BORON	23.5±0.6	1612.± 48.	0.178±0.005
	CARBON	22.6±0.9	923.± 43.	0.182±0.008
	NITROGEN	21.7±1.4	405.± 24.	0.169±0.009
DEUTERON	LITHIUM	23.6±0.2	5271.±154.	0.171±0.010
	BERYLLIUM	23.8±0.6	1439.± 64.	0.161±0.004
	BORON	24.8±0.7	984.± 40.	0.172±0.004
	CARBON	24.0±0.8	549.± 23.	0.156±0.007
	NITROGEN	25.8±1.7	224.± 16.	0.159±0.008

TABLE V-3 (CONTINUED)

Particle	Trigger IRF	Temperature τ (MeV)	Cross section σ_0 (mb)	Velocity β (c)
TRITON	LITHIUM	19.8±0.5	3497.±155.	0.137±0.004
	BERYLLIUM	20.4±1.0	894.± 71.	0.135±0.006
	BORON	23.0±1.5	642.± 50.	0.144±0.007
	CARBON	24.6±0.9	362.± 28.	0.138±0.023
	NITROGEN	23.3±1.3	164.± 24.	0.133±0.017
^{3}He	LITHIUM	34.3±1.3	910.± 52.	0.208±0.014
	BERYLLIUM	31.9±3.8	286.± 45.	0.223±0.021
	BORON	32.9±4.9	176.± 22.	0.178±0.035
	CARBON	35.3±6.9	109.± 12.	0.159±0.059

TABLE V-3 (CONTINUED)

Particle	Trigger IRF	Temperature τ (MeV)	Cross section σ_0 (mb)	Velocity β (c)
^{4}He	LITHIUM	25.2±1.0	1882.±158.	0.172±0.007
	BERYLLIUM	26.3±1.3	546.± 56.	0.183±0.006
	BORON	27.8±1.6	386.± 64.	0.197±0.012
	CARBON	27.5±2.4	219.± 25.	0.199±0.013
	NITROGEN	25.7±5.2	90.± 17.	0.152±0.035

Figure V-13. [(a) and (c)] Coincidence spectra moving source fit temperatures and velocities for the LP and IRF triggers and [(b) and (d)] the PLF trigger from the reaction 92 MeV ^{40}Ar+Au. The parameters for protons (circles), deuterons (squares), tritons (double triangles), ^{3}He (crosses), and ^{4}He (pluses) are plotted as ratios of the coincident spectrum value over the inclusive spectrum value as a function of coincident particle mass.

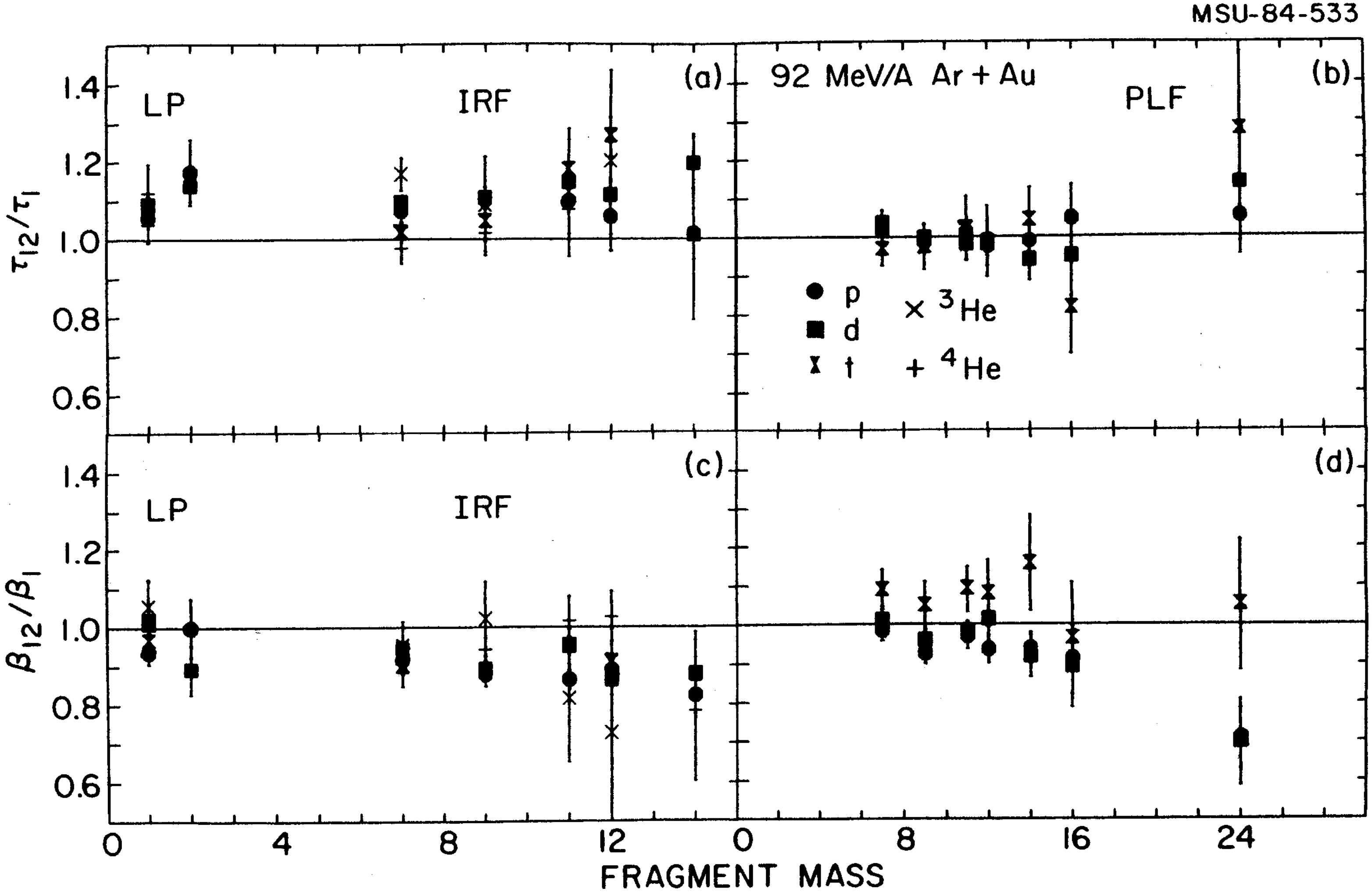
MSU-84-533
92 MeV/A Ar + Au
(a)
(b)
(c)
(d)
LP
IRF
PLF
● p
■ d
t
× ^{3}He
+ ^{4}He
τ_{12}/τ_1
β_{12}/β_1
1.4
1.2
1.0
0.8
0.6
0
4
8
12
16
24
FRAGMENT MASS

Figure V-13

of the moving source fits. The size of the scintillator array gave an angular acceptance at the 45 degree setting forward to ≈35 degrees. It is well known that forward angle inclusive light particle spectra show contributions from projectile evaporation at energies corresponding to the beam velocity. It is likely that detection of intermediate mass fragments at -30 degrees selects events in which the projectile either disintegrates or is appreciably slowed. The IRF triggered light particle spectra would therefore not be as likely to have contributions from projectile evaporation.

Figure V-14 shows the results of the hydrodynamics (HD) calculation of Buchwald [Bu 84] for the reaction 92 MeV/A ^{40}Ar+Au. The solid lines are the predicted p, d, t, ^{3}He, and ^{4}He spectra for in-plane angles of 45, 70, and 90 degrees and an azimuthal angle of $\phi=0°$. An azimuthal angle of $\phi=0°$ corresponds to the side of the reaction plane on which the projectile nucleus is incident in the calculation. the dot-dashed lines show the prediction for an azimuthal angle of $\phi=180°$, ie. the opposite side of the reaction plane. The calculation is impact parameter averaged for impact parameters from 0 to 7 fermi. The calculation is not azimuthally averaged as was the HD calculation used in comparison to the inclusive light particle spectra. The normalizations used for the HD predictions of Figure V-14 were the same as those used for the azimuthally averaged predictions of Figure V-1. The hydrodynamics prediction can

Figure V-14. Coincidence energy spectra from 92 MeV/A Ar+Au for (a) p,d,t and (b) ^{3}He,^{4}He triggered by a Li fragment in the IRF trigger. The solid (dot-dashed) lines correspond to an impact parameter averaged hydrodynamics calculation for an azimuthal angle of 0° (180°)

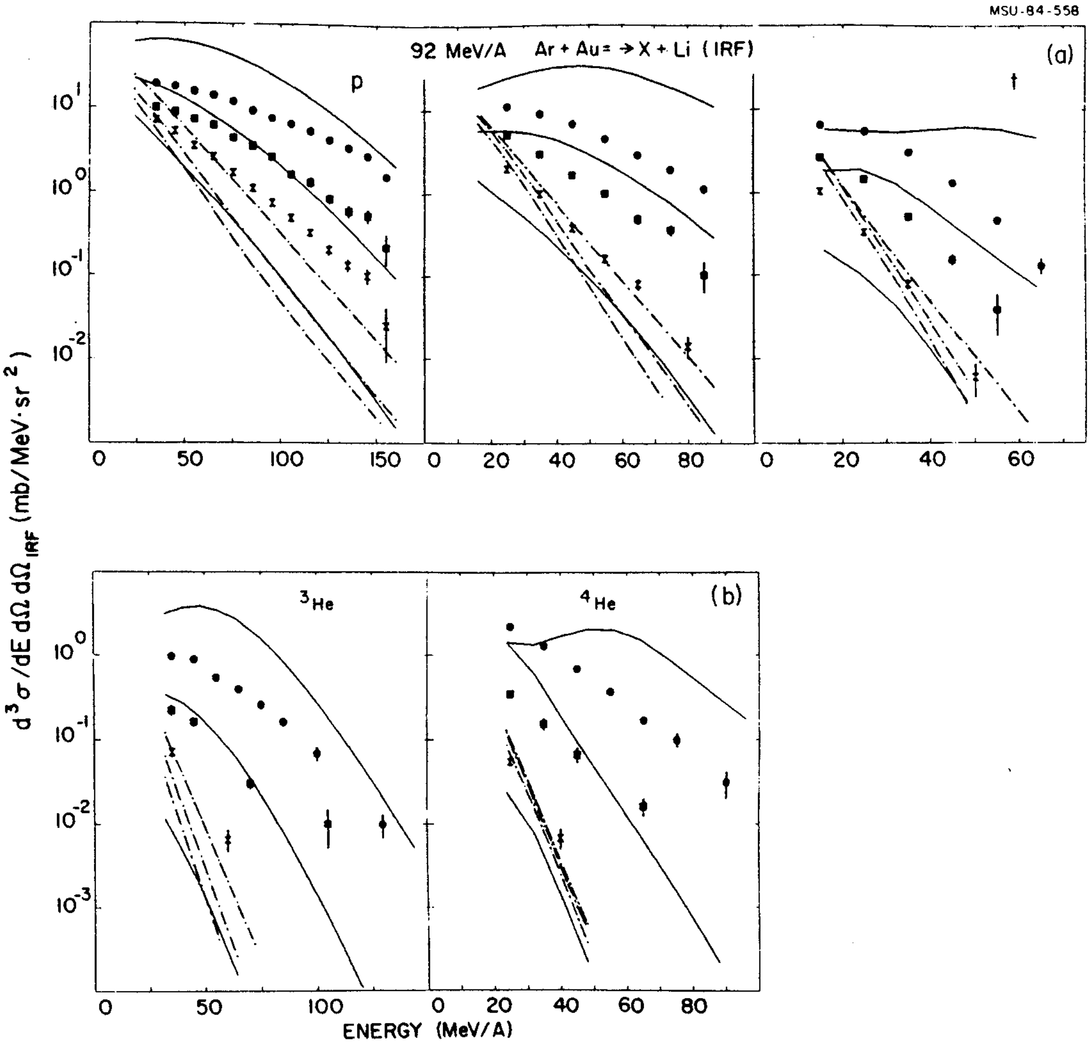
MSU-84-558
92 MeV/A Ar + Au= → X + Li (IRF)
(a)
p
t
10^1
10^0
10^{-1}
10^{-2}
0
50
100
150
0
20
40
60
80
0
20
40
60
^{3}He
^{4}He
(b)
10^0
10^{-1}
10^{-2}
10^{-3}
0
50
100
0
20
40
60
80
ENERGY (MeV/A)
$d^3\sigma/dE\,d\Omega\,d\Omega_{IRF}$ (mb/MeV·sr^2)

Figure V-14

be characterized by the enhancement of the forward angle $\phi=0°$ spectra. The $\phi=180°$ prediction is almost isotropic. This azimuthal angle dependence is due to what is called the "highly inelastic bounce-off" effect. Hydrodynamics predicts that for collisions which are not head-on, the incident projectile is inelastically scattered from the target nucleus into the $\phi=0°$ side of the reaction plane and then decays by emission of light particles. The light particles are focussed in the direction of the scattered projectile due to its relatively high velocity. The target nucleus is also excited and decays by emission of light particles while slowly recoiling into the $\phi=180°$ side of the reation plane. The predicted $\phi=0°$ spectra subsequently show an enhancement in the high energy tails at forward angles. The $\phi=180°$ spectra are characteristic of emission from a stationery source. The symbols in Figure V-14 are light particle coincidence spectra for a Li fragment in the IRF trigger. The light particle spectra, while not in agreement with the prediction at either azimuthal angle, are qualitively more like the $\phi=0°$ prediction. The disagreement with the data may be a result of the experimental determination of the reaction plane. The intermediate mass fragments measured in the IRF trigger detector may be from central and head-on collsions in which the projectile explodes into a number of lighter fragments. An individual fragment would carry no information about the reaction plane. The disagreement may also be due to an overprediction of the reaction dynamics by the model. It appears that an event trigger which more completely measures the multiplicity of charged particles created in heavy ion collisions, ie. a 4π array, is needed.

3. Light Particle - PLF Coincidence Spectra

Light particle spectra for coincidences between p, d and t at 45, 67.5, and 90 degrees and projectile-like fragments ($3 \leq Z \leq 15$) at -13 degrees are shown in Figures V-15-17. It was shown in section A.5. that the observed fragmentation process was the same for fragments in the PLF trigger with $8 \leq Z \leq 15$. The spectra for coincident fragments with $9 \leq Z \leq 15$ have therefore, been summed together in order to obtain reasonable statistics. The inclusive light particle spectra have been included in the figures for comparison with the coincidence spectra. The light particle coincidence spectra for the Li through N PLF triggers appear to be very similar to the inclusive spectra.

As was pointed out in section A.5. of this chapter, the inclusive PLF spectra for fragments with $Z \leq 7$ exhibit substantial contributions from thermal source emission associated with central collisions. It is therefore, not surprising that the light particle coincidence spectra associated with these fragments are similar to the inclusive spectra and the IRF triggered spectra. The conservation of momentum calculations (dotted lines) are shown for the Li through N PLF triggers. Comparison of the calculation with

Figure V-15 (a)Proton inclusive energy spectra and proton coincidence spectra for PLF trigger fragments (b)lithium, (c)beryllium, (d)boron, (e)carbon, (f)nitrogen, (g)oxygen, and (h)fluorine through phosphorus from the reaction 92 MeV/A ^{40}Ar+Au. The trigger fragment angle was -13°. The solid and dotted lines are moving source fits and momentum conservation calculations, respectively, as described in the text.

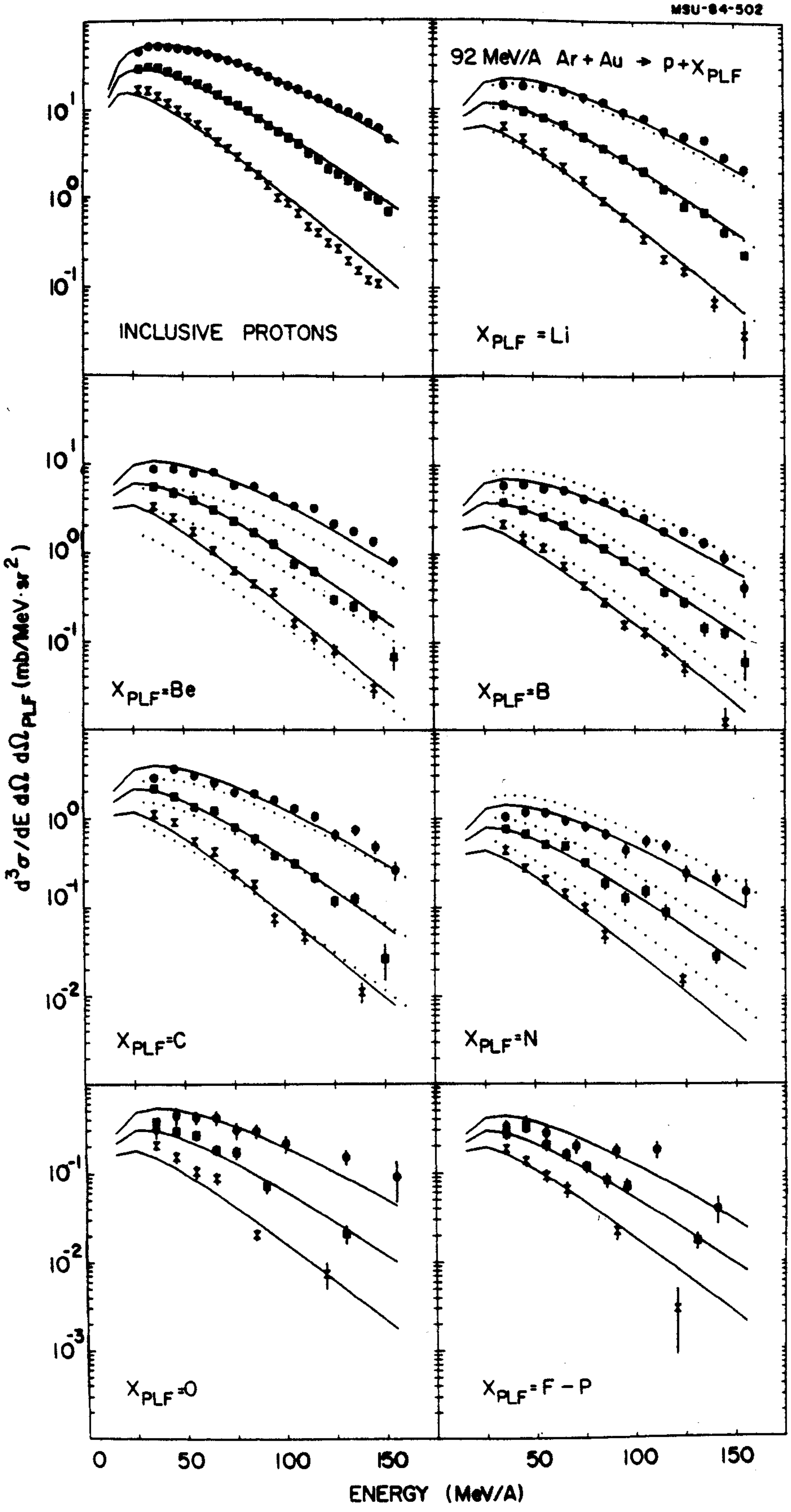
MSU-84-502
92 MeV/A Ar + Au → p + X_{PLF}
INCLUSIVE PROTONS
X_{PLF} = Li
X_{PLF} = Be
X_{PLF} = B
X_{PLF} = C
X_{PLF} = N
X_{PLF} = O
X_{PLF} = F − P
$d^3\sigma/dE\,d\Omega\,d\Omega_{PLF}$ (mb/MeV·sr^2)
10^1
10^0
10^{-1}
10^{-2}
10^{-3}
0
50
100
150
ENERGY (MeV/A)

Figure V-15

Figure V-16. Same as Figure V-15 for deuterons.

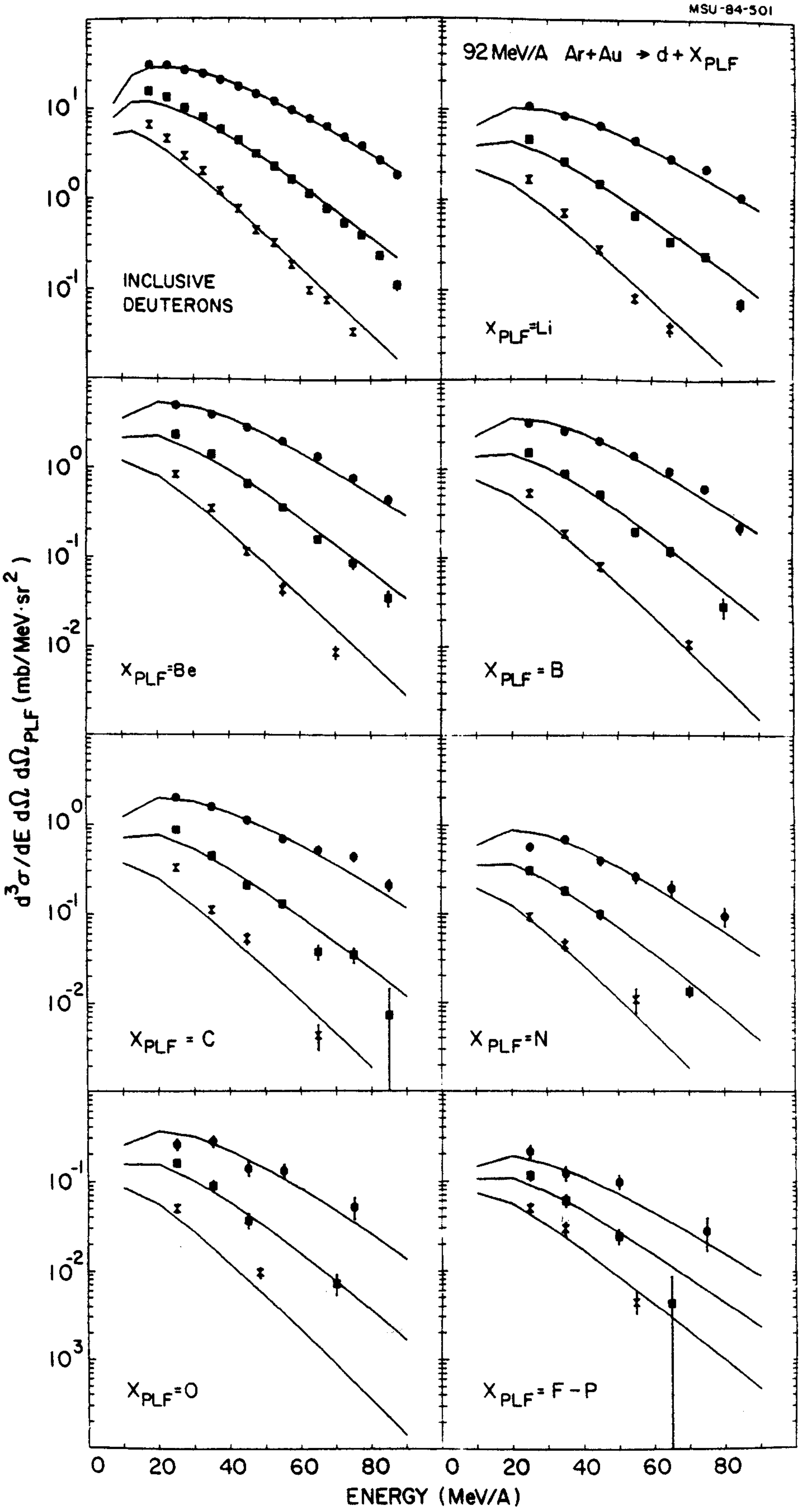
MSU-84-501
92 MeV/A Ar+Au → d + X_{PLF}
INCLUSIVE DEUTERONS
X_{PLF}=Li
X_{PLF}=Be
X_{PLF} = B
X_{PLF} = C
X_{PLF}=N
X_{PLF}=O
X_{PLF}= F - P
$d^3\sigma/dE\,d\Omega\,d\Omega_{PLF}$ (mb/MeV·sr^2)
10^1
10^0
10^{-1}
10^{-2}
10^3
0
20
40
60
80
ENERGY (MeV/A)

Figure V-16

Figure V-17. Same as Figure V-15 for tritons.

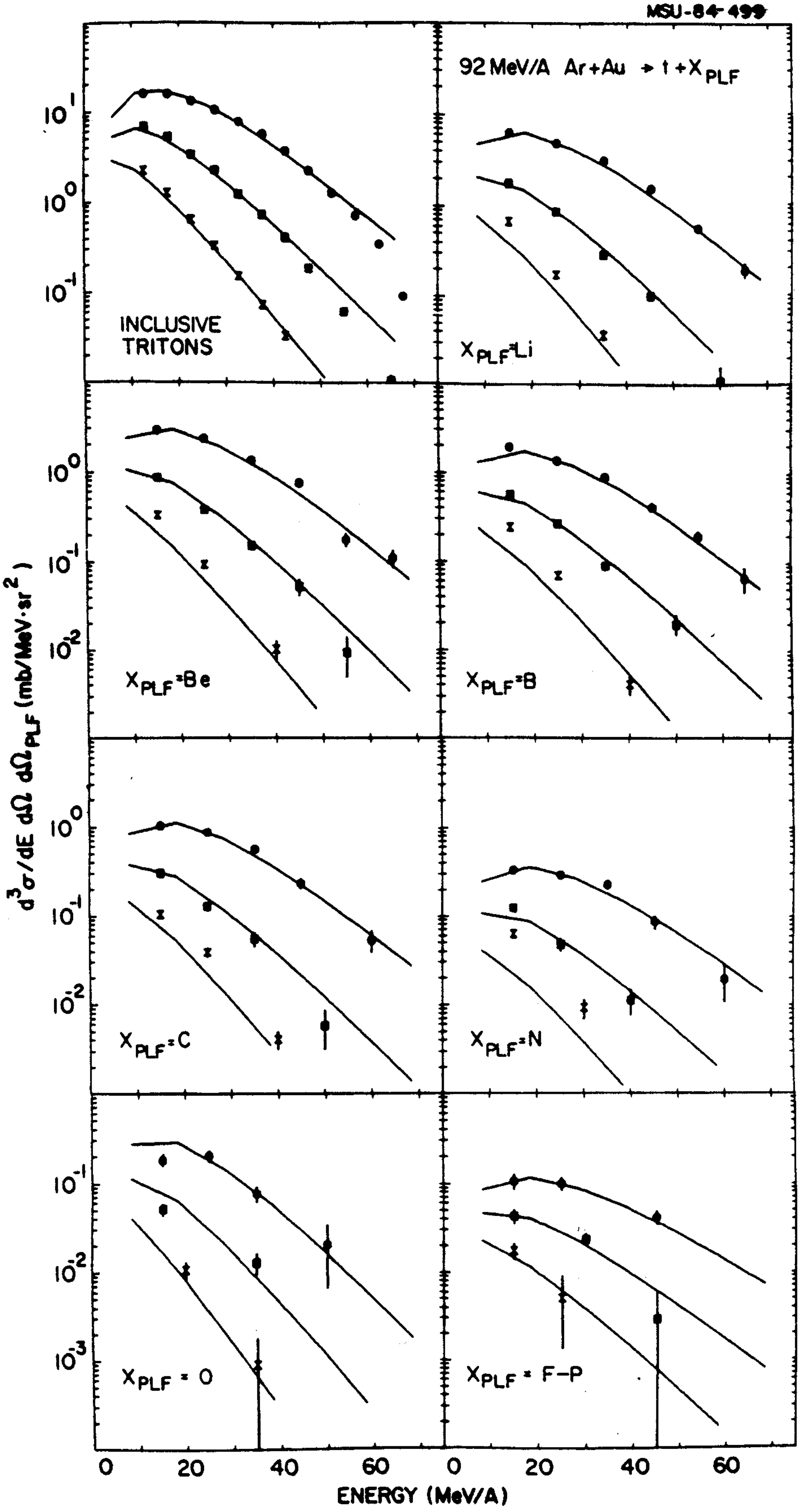
MSU-84-499
92 MeV/A Ar+Au → t+X_PLF
INCLUSIVE TRITONS
X_PLF=Li
X_PLF=Be
X_PLF=B
X_PLF=C
X_PLF=N
X_PLF = O
X_PLF = F-P
d³σ/dE dΩ dΩ_PLF (mb/MeV·sr²)
10¹
10⁰
10⁻¹
10⁻²
10⁻³
0
20
40
60
ENERGY (MeV/A)

Figure V-17

the data shows that there is little effect due to conservation of momentum for emission to -13 degrees. It can be seen from Figure V-15 that the proton coincidence cross sections for the oxygen and the fluorine through phosphorus PLF triggers have much flatter angular distributions than the inclusive cross sections. A flatter angular distribution is characteristic of a lower source velocity. A similar trend is seen for the deuteron spectra.

For fragments at -13 degrees with $8 \leq Z \leq 15$, the inclusive PLF spectra are dominated by the projectile fragmentation process. Collisions leading to projectile fragmentation must necessarily be peripheral and therefore, less likely to create an excited moving source. There would be two primary sources of emission for this type of collision - emission from the fragmenting projectile which would be focussed in the direction of the projectile, and emission from the excited target which would be isotropic in the laboratory frame. The light particle spectra measured in this experiment are well away from the measured fragment direction. The observation of lower apparent source velocities for the proton and deuteron spectra is therefore consistent with emission from the excited target. There is still a contribution from an intermediate source, although it appears to be greatly diminished.

Light particle - fragment coincidence spectra for fragments with $Z \geq 16$ had insufficient statistics to study the reaction mechanisms involved. If the mechanism for these fragments is few nucleon transfer, then it is likely that the associated light particle coincidence rate is low. The low statistics are consistent with this assumption, as well as with the observed trend toward decreasing fragmentation cross sections with increasing fragment mass.

The extracted moving source fit parameters are given in Table V-4. The temperatures and velocities are plotted in Figures V-13;b,d as ratios of the coincident values to the inclusive values. Note that the parameters for spectra summed over coincidences with fluorine through phosphorous fragments are plotted at an approximate average mass of 24. As was true for the light particle - IRF spectra, the temperature parameter shows no variation with the PLF trigger fragment mass. In addition, the PLF triggered spectra source temperatures are the same as the inclusive temperature. The velocities show a clear trend toward decreasing velocities with increasing trigger fragment mass for the proton and deuteron spectra. An apparent velocity 30 percent below the inclusive result is obtained for the average projectile mass of A=24. The triton spectra velocities do not decrease with trigger coincident fragment mass and in fact, are very nearly constant. One might speculate, that since composite emission is suppressed for a less excited system, the triton spectra which are observed between 45 and 90 degrees are dominated by the contributions from more central collisions and or alternately by emission from whatever intermediate source might be created in the

TABLE V-4

MOVING SOURCE FIT PARAMETERS FOR 92 MeV/A Ar+Au (PLF TRIGGER)

Particle	Trigger PLF	Temperature τ (MeV)	Cross section σ_0 (mb)	Velocity β (c)
PROTON	LITHIUM	21.8±0.3	9365.±264.	0.202±0.005
	BERYLLIUM	21.1±0.3	4458.±149.	0.190±0.006
	BORON	21.6±0.5	2928.± 97.	0.199±0.006
	CARBON	21.0±0.6	1590.± 68.	0.192±0.007
	NITROGEN	21.2±0.9	588.± 30.	0.192±0.008
	OXYGEN	22.4±1.9	233.± 18.	0.187±0.018
	FLUOR-PHOS	22.5±2.1	187.± 16.	0.145±0.016
DEUTERON	LITHIUM	22.4±0.7	5115.±272.	0.183±0.006
	BERYLLIUM	21.6±0.7	2490.±143.	0.173±0.005
	BORON	21.2±0.9	1667.± 96.	0.177±0.005
	CARBON	21.2±1.2	921.± 72.	0.183±0.010
	NITROGEN	20.3±1.2	372.± 32.	0.166±0.010
	OXYGEN	20.5±2.2	153.± 23.	0.161±0.019
	FLUOR-PHOS	24.6±3.3	88.± 11.	0.126±0.020

TABLE V-4 (CONTINUED)

Particle	Trigger PLF	Temperature τ (MeV)	Cross section σ_0 (mb)	Velocity β (c)
TRITON	LITHIUM	18.9±0.9	3186.±264.	0.165±0.008
	BERYLLIUM	19.0±1.2	1462.±149.	0.159±0.009
	BORON	19.9±1.6	906.±103.	0.165±0.009
	CARBON	19.2±1.8	569.± 89.	0.164±0.013
	NITROGEN	20.3±1.6	197.± 30.	0.176±0.019
	OXYGEN	15.9±2.3	130.± 25.	0.146±0.022
	FLUOR-PHOS	24.9±3.9	64.± 17.	0.159±0.026

process leading to projectile fragmentation.

4. Light Particle - LP Coincidence Spectra

Light particle spectra for coincidences between p, d, t, ^{3}He and ^{4}He at 45, 67.5, and 90 degrees and light particles (p,d) in the LP trigger at -90 degrees are shown in Figure V-18. The energy spectra of the LP trigger were integrated from a lower cut of 20 MeV/nucleon up to the maximum measured energy. A comparison with the momentum conservation calculations shows that the coincidence cross sections are well described by the assumption of emission from a moving thermal source.

The extracted moving source fit parameters for the light particle - LP triggerd spectra are tabulated in Table V-5. The temperatures and velocities are plotted in Figures V-13;a&c, respectively, along with the IRF parameters as ratios to the inclusive values. The moving source temperatures and velocities are similar to those for the intermediate rapidity fragment coincidence spectra.

C. 30 MeV/A ^{12}C+Al,Au Inclusive Spectra

1. Light Particle Inclusive Spectra

Light particle inclusive spectra (Z=1,2) have been measured for the reaction 30 MeV/A ^{12}C+Al at the angles 45, 56, 71, and 90 degrees and at 45, 49, 56, 71, and 90 degrees for 30 MeV/A ^{12}C+Au. The 45 and 49 degree spectra for the

Figure V-18. Light particle coincidence spectra for (a)protons in coincidence with p, (b)protons in coincidence with d, and (c)deuterons, (d)tritons, (e)^{3}Heliums, and (f)^{4}Heliums in coincidence with protons in the LP trigger from the reaction 92 MeV/A ^{40}Ar+Au. The LP trigger was at -90°. The solid and dotted lines are moving source fits and momentum conservation calculations, respectively, as described in the text.

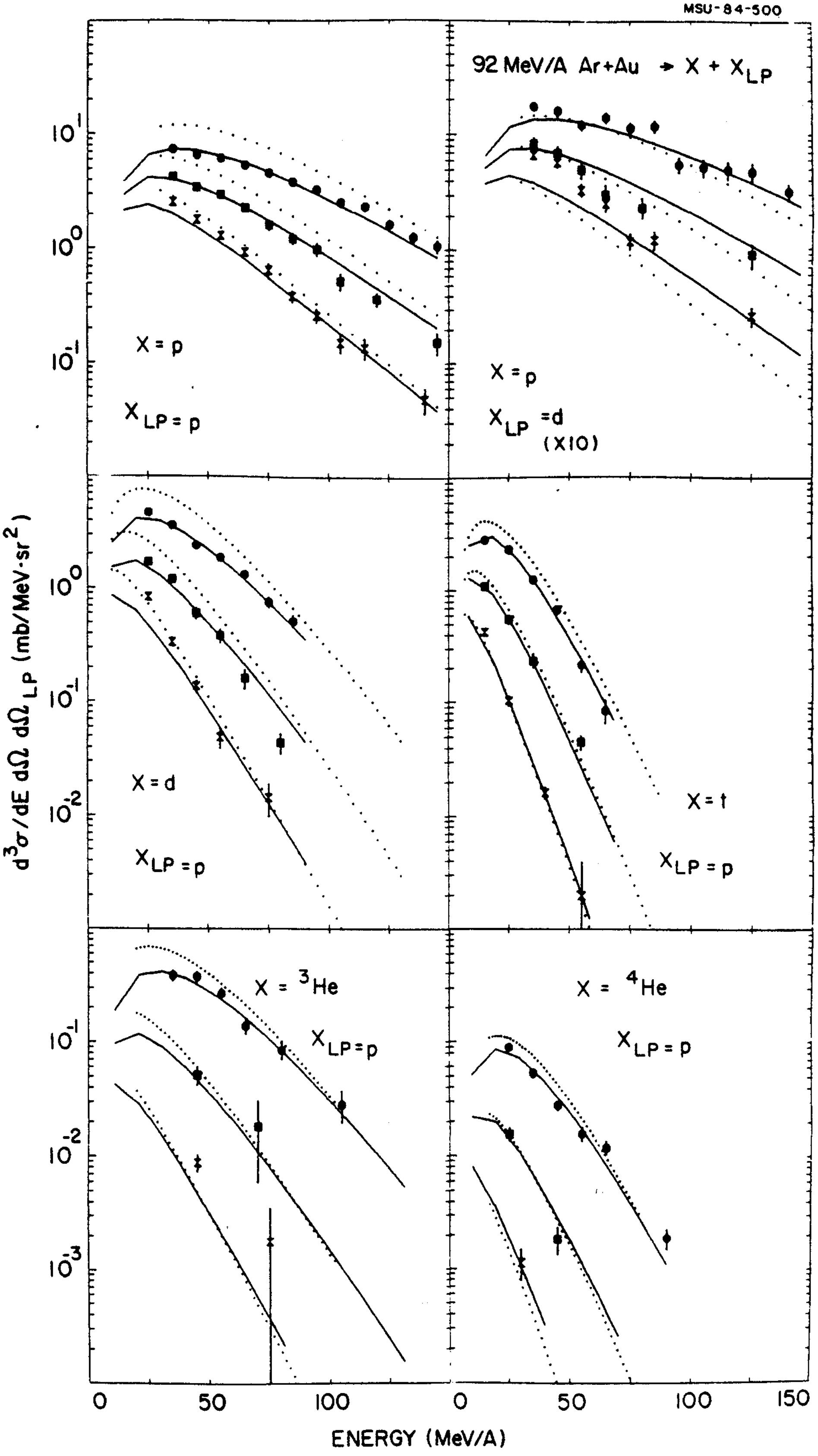
MSU-84-500
92 MeV/A Ar+Au → X + X_{LP}
X = p
X_{LP} = p
X = p
X_{LP} = d
(X10)
X = d
X_{LP} = p
X = t
X_{LP} = p
X = ^{3}He
X_{LP} = p
X = ^{4}He
X_{LP} = p
$d^3\sigma/dE\,d\Omega\,d\Omega_{LP}$ (mb/MeV·sr^2)
10^1
10^0
10^{-1}
10^{-2}
10^{-3}
0
50
100
150
ENERGY (MeV/A)

Figure V-18

TABLE V-5

MOVING SOURCE PARAMETERS FOR 92 MeV/A Ar+Au (LP TRIGGER)

Particle	Trigger LP	Temperature τ (MeV)	Cross section σ_0 (mb)	Velocity β (c)
PROTON	PROTON	22.6±0.5	3292.± 94.	0.192±0.006
PROTON	DEUTERON	25.2±1.8	679.± 40.	0.205±0.015
DEUTERON	PROTON	23.5±0.7	2110.± 36.	0.184±0.018
DEUTERON	DEUTERON	24.6±0.8	527.± 43.	0.161±0.011
TRITON	PROTON	20.5±1.1	1454.± 59.	0.147±0.003
^{3}He	PROTON	32.0±2.8	396.± 63.	0.230±0.016
^{4}He	PROTON	28.9±2.0	747.± 71.	0.193±0.010

Figure V-19. Inclusive energy spectra for p,d, and t from the reactions (a) 30 MeV/A ^{12}C+Au and (b) 30 MeV/A ^{12}C+Al . The angles measured are 47° (45° for the Al target) (circles), 56° (squares), 71° (triangles), and 90° (diamonds). The errors depicted are statistical. The solid lines correspond to moving source fits as described in the text.

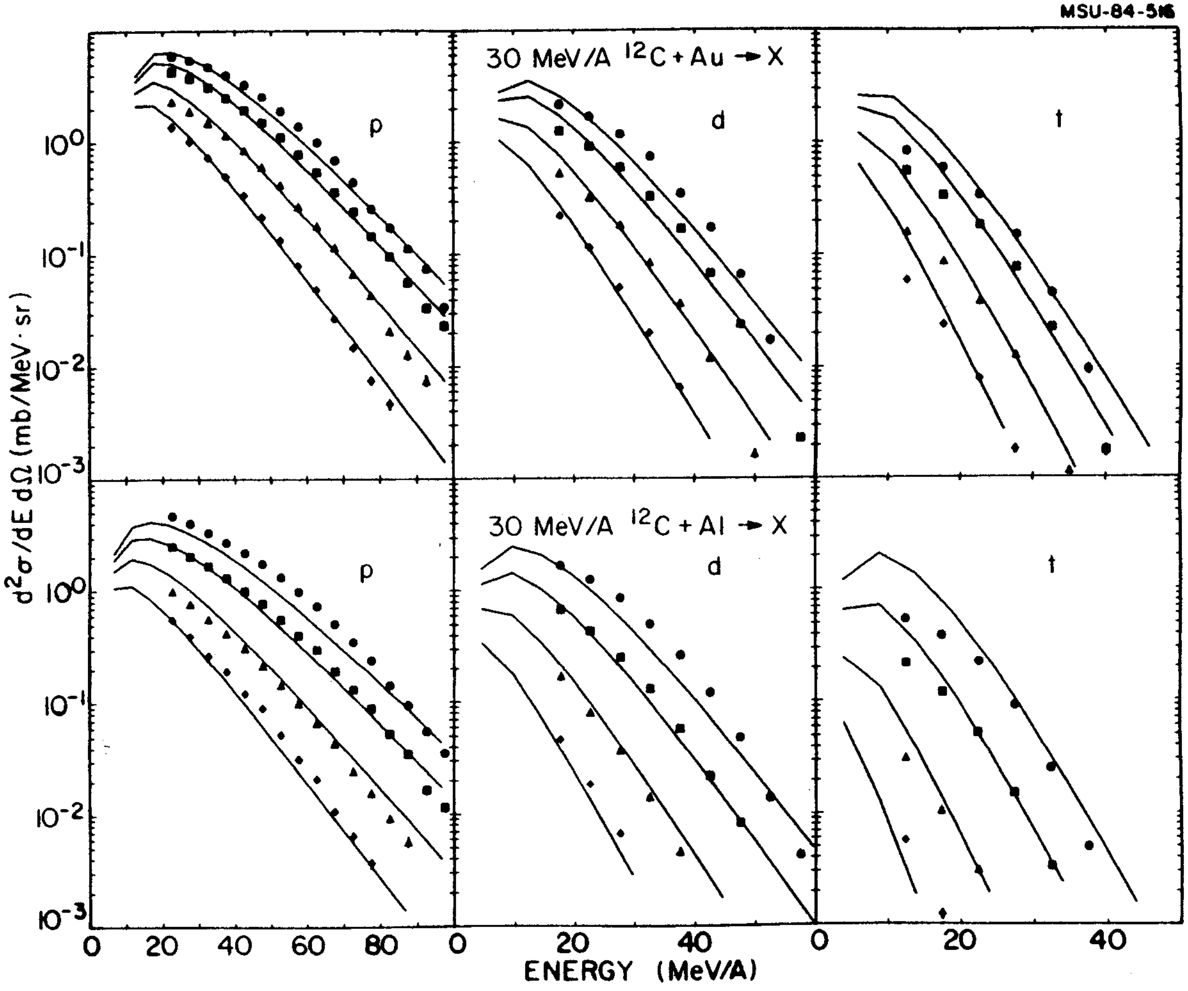
MSU-84-516
30 MeV/A ^{12}C + Au → X
30 MeV/A ^{12}C + Al → X
p
d
t
$d^2\sigma/dE\,d\Omega$ (mb/MeV·sr)
10^0
10^{-1}
10^{-2}
10^{-3}
0
20
40
60
80
ENERGY (MeV/A)

Figure V-19

Au target have been combined because of low statistics at the 45 degree setting. An average angle of 47 degrees will be used for the combined spectra. Energy spectra for the hydrogen isotopes are shown in Figure V-19. The solid curves in the figure are moving source fits to the data. The lower energy cuts for the fits were 30, 20, and 20 MeV/nucleon for p, d, and t, respectively. These cuts were selected in order to eliminate contributions from target evaporation. The most forward angle data were not included in the fits in order to eliminate contributions from projectile evaporation. The contributions from projectile evaporation can be more clearly seen in the d and t spectra shown in Figure V-20. These inclusive spectra were measured in a separate experiment for the reaction 30 MeV/A ^{12}C+Al at angles of 15, 45, 75, 90, and 105 degrees in the laboratory. The peaks in the 15 degree cross sections at energies of approximately 30 MeV/A are evidence of projectile evaporation. It can be seen that there is still a contribution from projectile evaporation at 45 degrees.

A coulomb shift of 4 MeV was used for light particles with the aluminum target and 10 MeV with the gold target. The same cuts and shifts will be used for the coincidence spectra. The moving source fit parameters are given in Table V-6. The temperatures and velocities are in agreement with the systematics of Figure V-4. Spectra for the helium isotopes were also measured. However, it was found that there was an insufficient amount of data to warrant further

Figure V-20. Inclusive energy spectra for d and t from the reaction 30 MeV/A ^{12}C+Au at angles of 15° (pluses), 45° (circles), 75° (squares), 90° (double triangles), and 105° (crosses). The spectra were measured in a separate experiment using a Si-NaI(Tl) telescope.

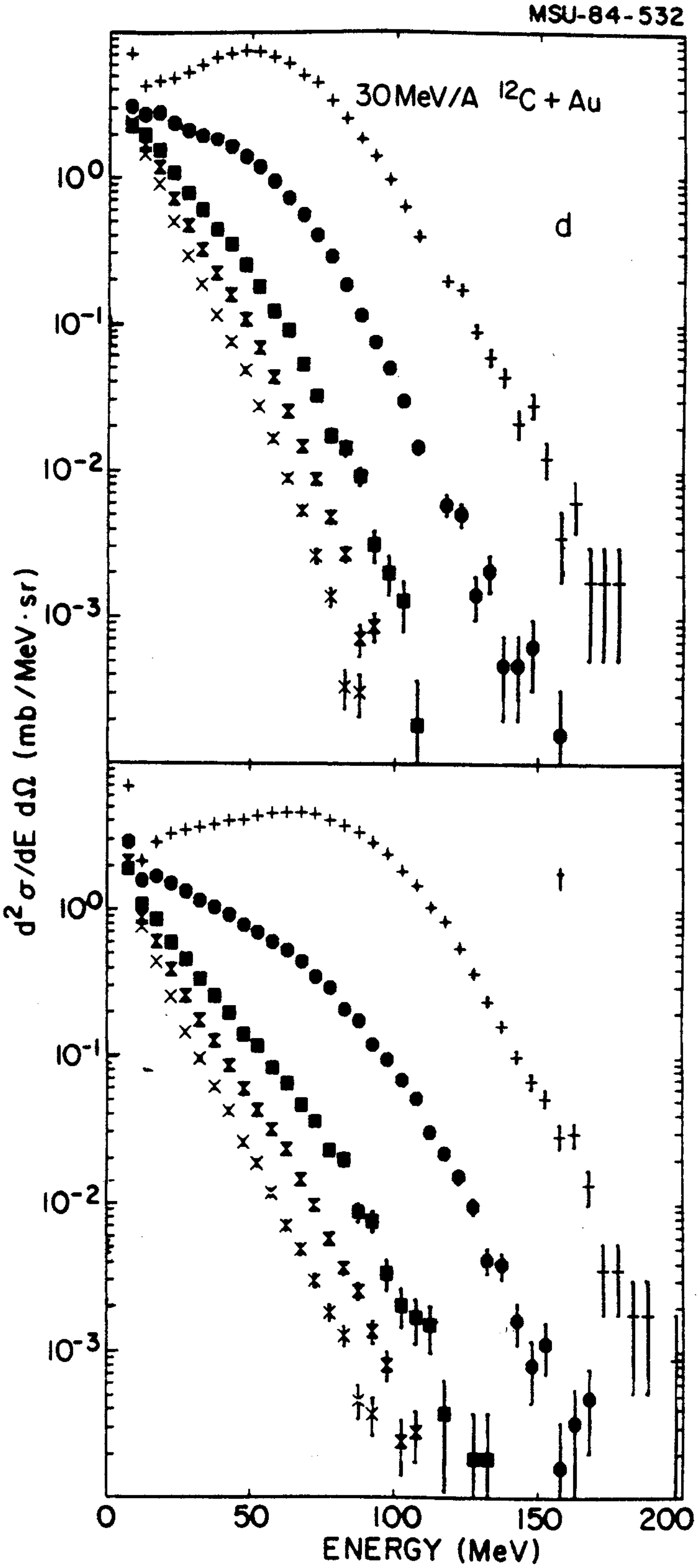
MSU-84-532
30MeV/A ¹²C + Au
d
10⁰
10⁻¹
10⁻²
10⁻³
d²σ/dE dΩ (mb/MeV·sr)
0
50
100
150
200
ENERGY (MeV)

Figure V-20

TABLE V-6

MOVING SOURCE PARAMETERS 30 MeV/A C+Al,Au (INCLUSIVE)

Particle	Temperature τ (MeV)	Cross section σ_0 (mb)	Velocity β (c)
30 MeV/A C+Al			
PROTON	9.5±0.2	774.± 38.	0.139±0.047
DEUTERON	8.4±0.4	510.± 75.	0.130±0.007
TRITON	7.0±0.2	760.±143.	0.140±0.003
30 MeV/A C+Au			
PROTON	9.3±0.1	1200.± 32.	0.121±0.003
DEUTERON	9.3±0.3	697.± 59.	0.100±0.005
TRITON	9.2±0.6	600.±131.	0.092±0.005

analysis. The extracted source temperatures for the two targets are quite similar. The source velocities for the Al target spectra are ≈30 percent higher than for the Au target. The fireball model and the systematics of the moving source parameterization predict that the source velocity should scale as the velocity of the center of mass of the colliding system. For C+Al,Au, the ratio of the center of mass velocities is about 1.35 in agreement with the observed velocities.

2. Intermediate Rapidity Fragment Inclusive Spectra

The inclusive fragment spectra ($3 \leq Z \leq 6$) for the IRF trigger at -25 degrees are shown in Figures V-21;a&b for the Al and Au targets, respectively. The shapes of the spectra are quite similar and again indicate, that as was true at higher energies [Ja 83], these fragments are created by similar mechanisms. Further evidence for a single mechanism has been seen in the reaction 30 MeV/A ^{12}C+Au by Fields et.al. [Fi 84]. Using a single set of initial parameters for all fragments, Fields performed a model calculation which assumed emission from an excited region of the combined target and projectile. The excitation region then spread into the colder surrounding material giving rise to a continuous progression of temperatures for the apparent source. It was concluded from the intermediate mass fragment spectra that the lighter fragments were more favorably emitted from the highly excited, early stages of

Figure V-21. Inclusive energy spectra for fragments in the IRF trigger at -25° with $3 \leq Z \leq 6$ from the reactions (a) 30 MeV/A ^{12}C+Al and (b) 30 MeV/A ^{12}C+Au.

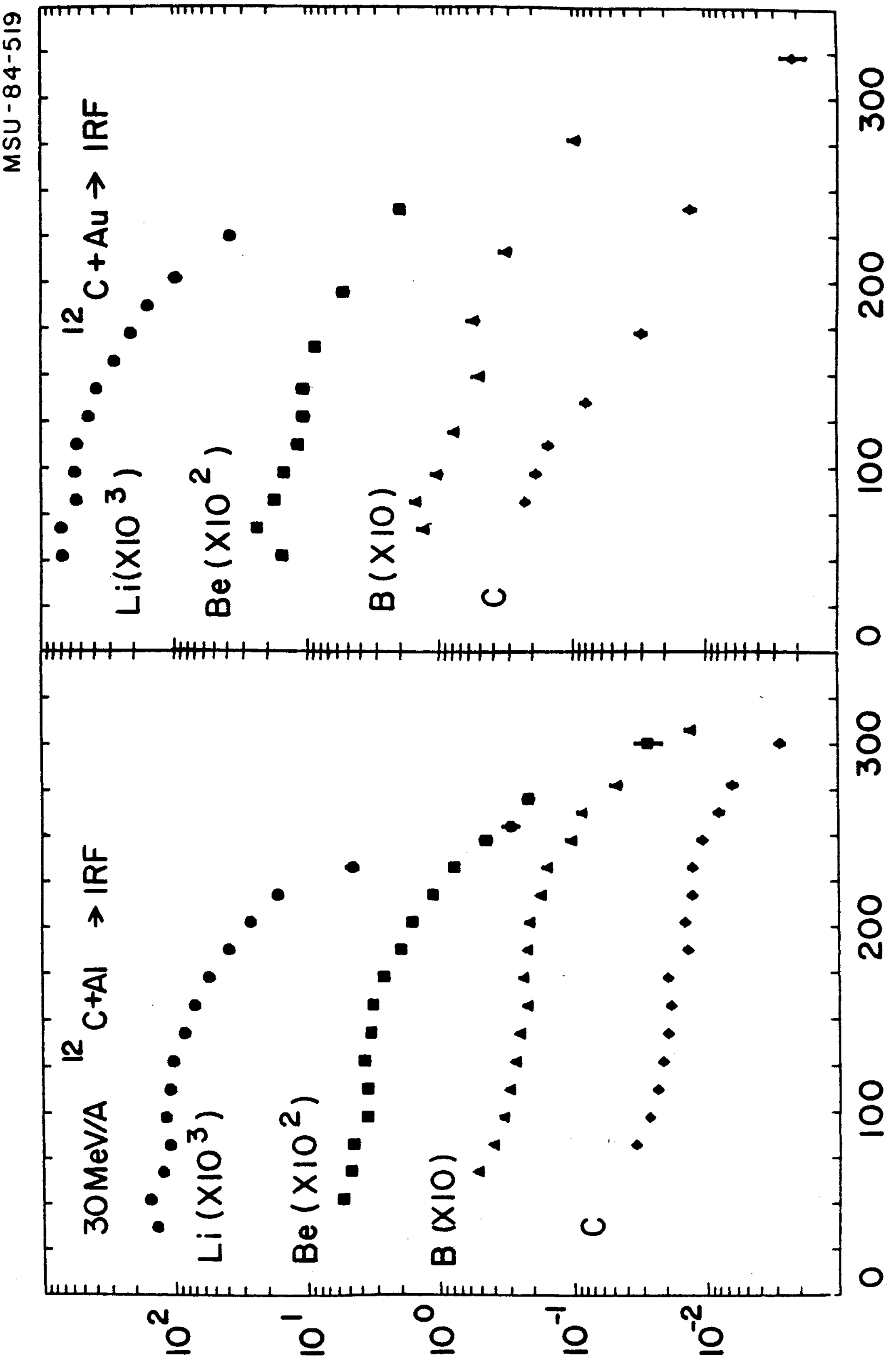
MSU-84-519
30MeV/A
^{12}C+Al → IRF
Li (X10^3)
Be (X10^2)
B (X10)
C
^{12}C+Au → IRF
Li(X10^3)
Be(X10^2)
B(X10)
C
0
100
200
300
0
100
200
300
10^2
10^1
10^0
10^{-1}
10^{-2}
$d^2\sigma/dE\,d\Omega$ (mb/MeV·sr)

Figure V-21

the reaction, whereas the heavier fragments were more favorably emitted from the cooler, later stages of the reaction. These trends may be evident in the coincidence spectra.

3. Projectile-Rapidity Fragment Inclusive Spectra

The inclusive fragment spectra ($3 \leq Z \leq 6$) for the PLF trigger at -13 degrees are shown in Figures V-22;a&b for the Al and Au targets, respectively. The spectra have been plotted as a function of the ratio of the detected fragment velocity over the incident projectile velocity. The fragment spectra at 30 MeV/A do not show the different reaction mechanisms described in section A.5. of this chapter as clearly as the 92 MeV/A spectra. The statistics of the coincidence data limited the fragment analysis to separation by Z leaving four fragment types with which to study three phenomena. The range of measured fragment energies shown in Figure V-22 have low energy experimental cuts which make it difficult to determine if fragmentation peaks exist in the spectra. This limited range is especially a problem for the Li and Be fragment spectra. Figure V-23 shows a more complete range of energies for the same fragments at 15 degrees in the reaction 25 MeV/A ^{12}C+Au [Ja 84]. The existence of a gaussian shaped peak in the boron fragment spectrum of Figure V-23 may be an indication of projectile fragmentation. The carbon spectrum appears to be dominated by elastic scattering. The laboratory grazing

Figure V-22. Inclusive cross sections for fragments in the PLF trigger at an angle of -13° with $3 \leq Z \leq 6$ from the reactions (a) 30 MeV/A ^{12}C+Al and (b) 30 MeV/A ^{12}C+Au (b) plotted versus the ratio of the fragment velocity over the projectile velocity.

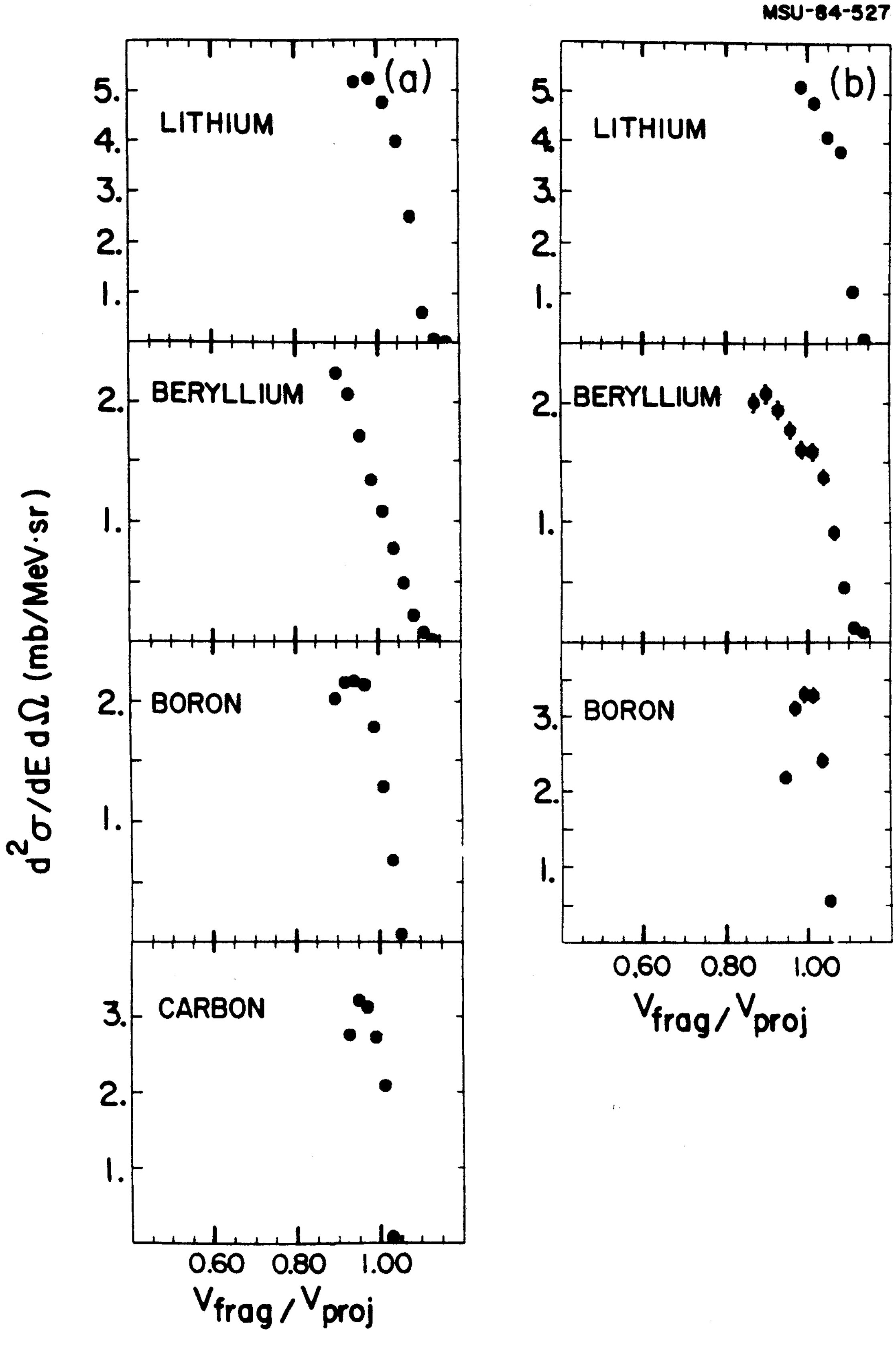
MSU-84-527
(a)
(b)
LITHIUM
BERYLLIUM
BORON
CARBON
5.
4.
3.
2.
1.
$d^2\sigma/dE\,d\Omega$ (mb/MeV·sr)
0.60
0.80
1.00
V_{frag}/V_{proj}

Figure V-22

Figure V-23. Unnormalized inclusive distributions for intermediate mass fragments with $3 \leq Z \leq 6$ from the reaction 25 MeV/A ^{12}C+Au at an angle of 15° plotted versus the ratio of the fragment velocity over the projectile velocity [Ja 84].

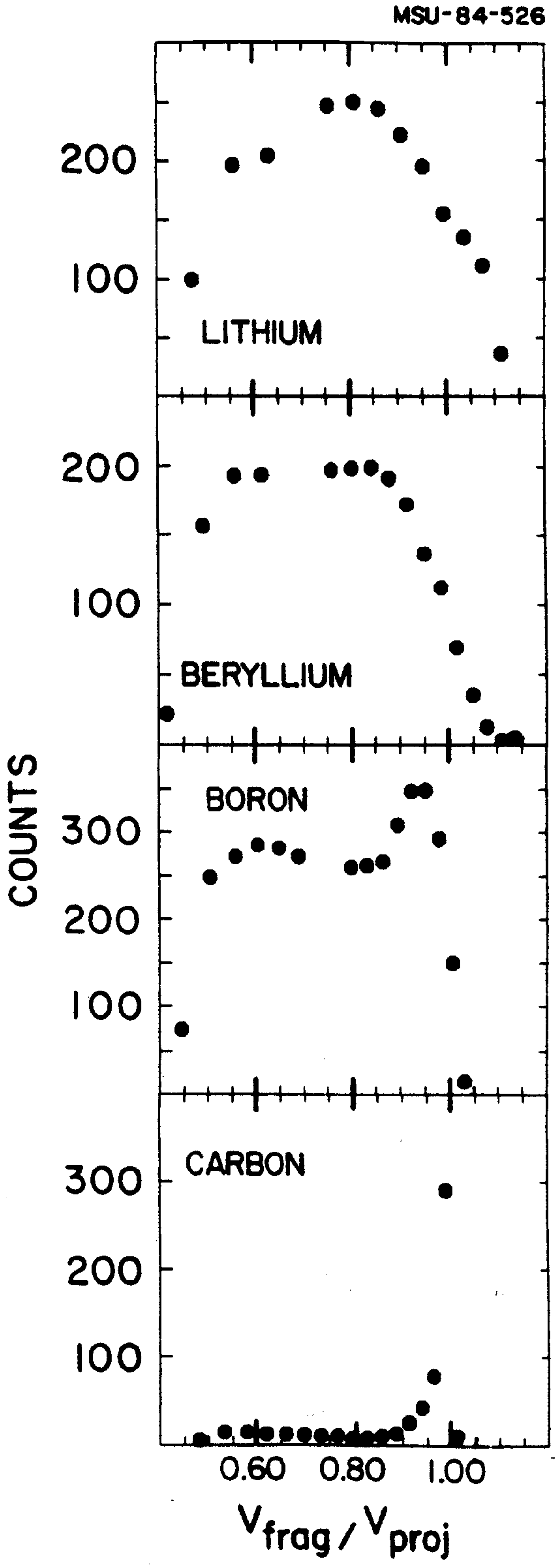
MSU-84-526
COUNTS
LITHIUM
200
100
BERYLLIUM
200
100
BORON
300
200
100
CARBON
300
200
100
0.60
0.80
1.00
V_{frag} / V_{proj}

Figure V-23

angle for the C+Al,(Au) reaction is approximately 2.4,(10.4) degrees. Projectile fragmentation may be more easily observed for the Al target carbon spectrum, since the projectile velocity fragments were detected well outside the grazing angle where the contributions to the spectra from elastic scattering are greatly reduced.

4. Light Particle (LP) Inclusive Spectra

The inclusive light particle spectra (Z=1,2) for the LP trigger at -45 degrees are shown in Figure V-24. The LP trigger data were available only for the Al target. The spectra are plotted as invariant cross sections as a function of the total particle momentum. The lines are to guide the eye. For the light particle - LP coincidence spectra, a cut at an energy of 20 MeV/A was imposed on the LP trigger spectra to eliminate contributions from target evaporation.

D. 30 MeV/A ^{12}C+Al Coincidence Spectra

1. Light Particle - IRF Coincidence Spectra

Light particle spectra for coincidences between protons and deuterons at 45, 56, 71, and 90 degrees and intermediate rapidity fragments ($3 \leq Z \leq 6$) at -25 degrees are shown in Figures V-25 and V-26. It is interesting to note that, although the 45 degree angle was not included in the fits, the moving source does not underestimate the forward

Figure V-24. Invariant cross section plots versus total momentum for p (circles), d (squares), t (triangles), ^{3}He (diamonds), and ^{4}He (double triangles) in the LP trigger at -45° from the reaction 30 MeV/A ^{12}C+Al. The lines are to guide the eye.

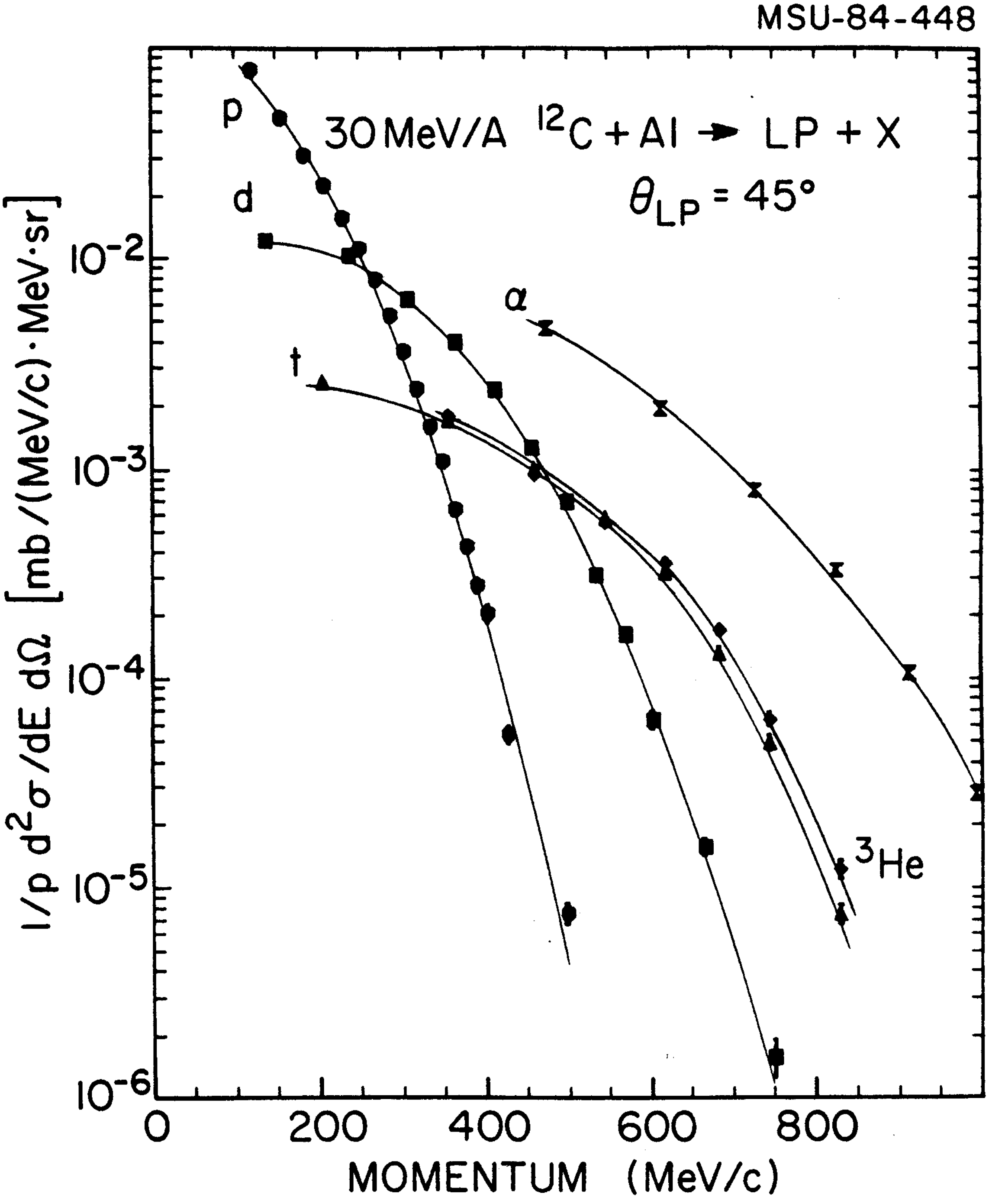
MSU-84-448
30 MeV/A ^{12}C + Al → LP + X
θ_{LP} = 45°
p
d
t
α
^3He
$1/p\ d^2\sigma/dE\ d\Omega$ [mb/(MeV/c)·MeV·sr]
10^{-2}
10^{-3}
10^{-4}
10^{-5}
10^{-6}
0
200
400
600
800
MOMENTUM (MeV/c)

Figure V-24

Figure V-25. Proton coincidence energy spectra for IRF trigger fragments (a)lithium, (b)beryllium, (c)boron, and (d)carbon from the reaction 30 MeV/A ^{12}C+Al. The trigger fragment angle was -25°. The solid and dot-dashed lines are moving source fits and momentum conservation calculations, respectively, as described in the text.

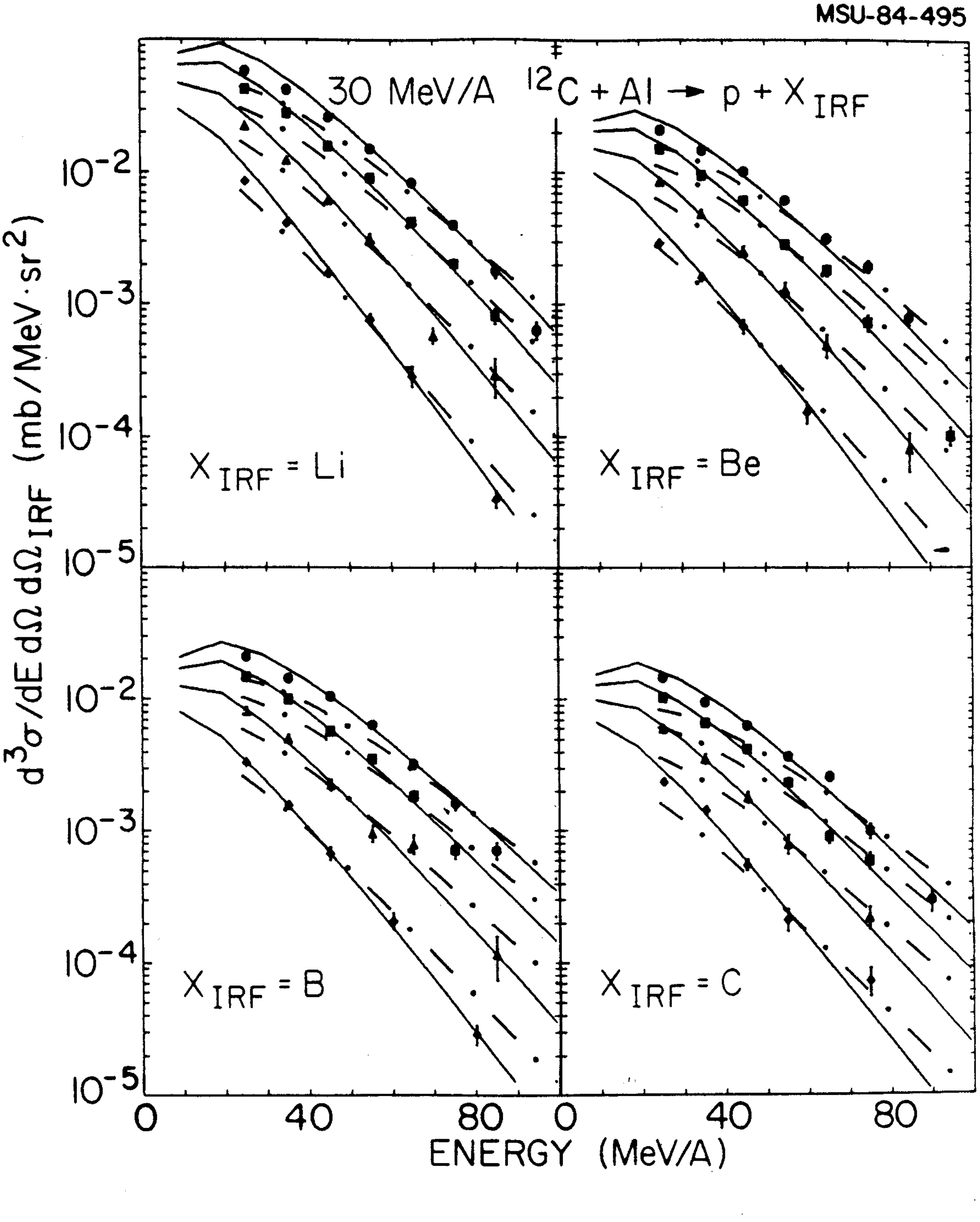
MSU-84-495
30 MeV/A ^{12}C + Al → p + X_{IRF}
X_{IRF} = Li
X_{IRF} = Be
X_{IRF} = B
X_{IRF} = C
$d^3\sigma/dE\,d\Omega\,d\Omega_{IRF}$ (mb/MeV·sr^2)
10^{-2}
10^{-3}
10^{-4}
10^{-5}
0
40
80
ENERGY (MeV/A)

Figure V-25

Figure V-26. Same as Figure V-25 for deuterons.

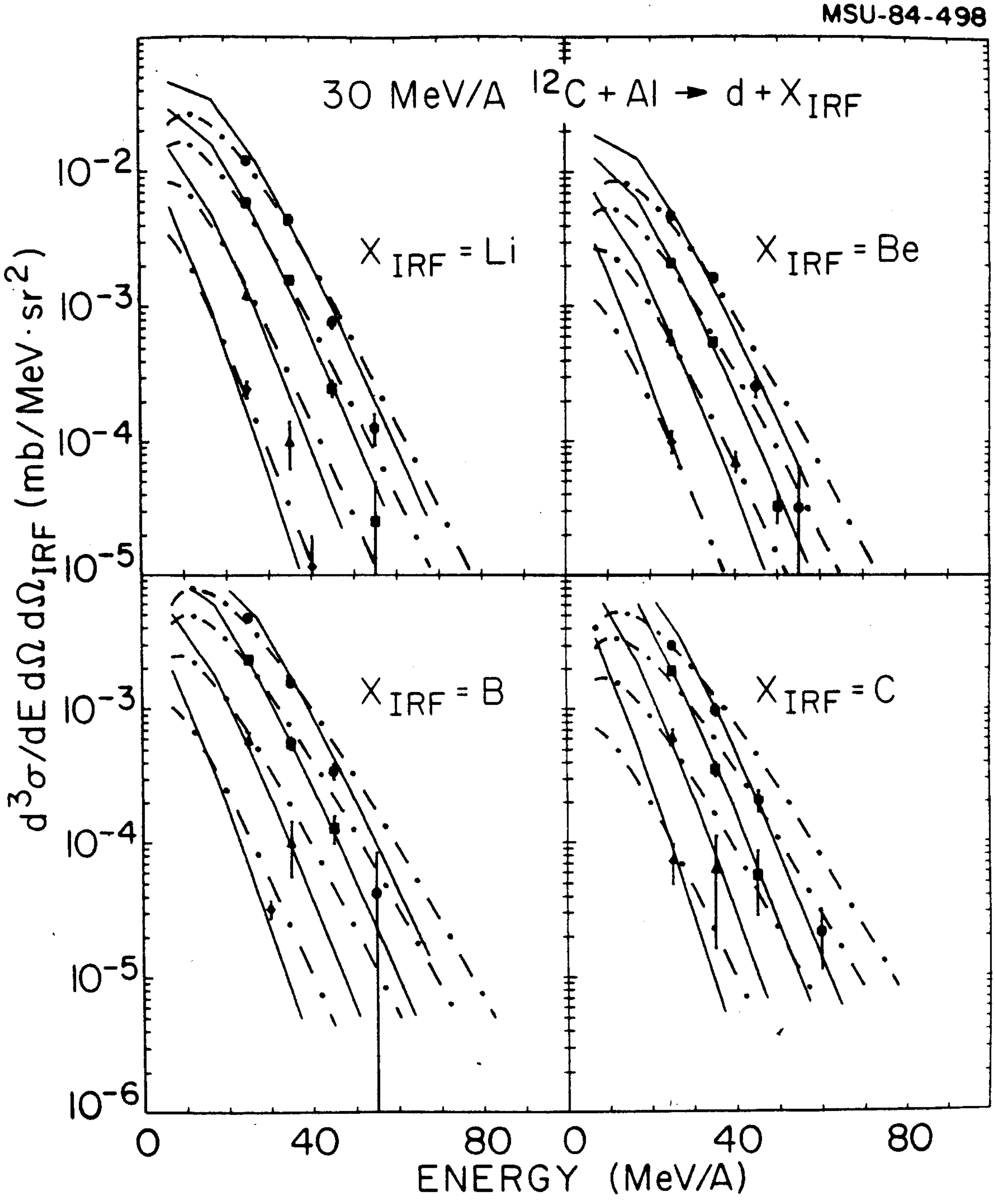
MSU-84-498
30 MeV/A $^{12}C + Al \rightarrow d + X_{IRF}$
X_{IRF} = Li
X_{IRF} = Be
X_{IRF} = B
X_{IRF} = C
$d^3\sigma/dE\,d\Omega\,d\Omega_{IRF}$ (mb/MeV·sr^2)
10^{-2}
10^{-3}
10^{-4}
10^{-5}
10^{-6}
0
40
80
ENERGY (MeV/A)

Figure V-26

angle as it did for the inclusive spectra (Figure V-19). This is another indication that the enhancements observed in the inclusive spectra are due to projectile evaporation.

For the ^{12}C+Al reaction, the fireball formalism predicts a source size of 18 nucleons for the impact parameter with the maximum weight. A preliminary calculation with N=18 gave spectra with slopes much flatter than the experimental results. Because of the relatively small source size compared to the emitted fragment, there is a large transverse velocity imparted to the source upon emission of the fragment. This recoil shows up in the light particle spectra as an enhancement of the higher energy cross sections. The effect becomes more pronounced for the heavier fragments as would be expected. The poor agreement with the experimental results for a source size of N=18 indicates that a larger source size is needed to take up the recoil momentum. If one considers that the source is probably not spatially separated from the remainder of the target, then the recoil momentum would be taken up by the entire projectile-target system, minus the emitted fragment. For example, for a coincident fragment with A=12, the source size becomes N=27 nucleons instead of 18. Calculations with a source size of N=27 nucleons are shown in Figures V-25 and 26 (dot-dashed lines). This calculation is in fair agreement with the data, although, there is still a flatter slope for the proton spectra with heavier IRF trigger fragments and for the deuteron spectra.

TABLE V-7

MOVING SOURCE PARAMETERS FOR 30 MeV/A C+Al,Au (IRF TRIGGER)

Particle	Trigger IRF	Temperature τ (MeV)	Cross section σ_0 (mb)	Velocity β (c)
30 MeV/A C+Al				
PROTON	LITHIUM	9.4 ±0.2	17.± 1.	0.130±0.004
	BERYLLIUM	9.6 ±0.2	6.± 0.	0.127±0.002
	BORON	10.1 ±0.2	5.± 0.	0.141±0.004
	CARBON	10.2 ±0.2	4.± 0.	0.125±0.002
DEUTERON	LITHIUM	8.4 ±0.7	10.± 3.	0.130±0.017
	BERYLLIUM	8.6 ±0.4	4.± 0.	0.117±0.007
	BORON	8.6 ±0.4	4.± 0.	0.133±0.003
	CARBON	8.1 ±0.4	4.± 1.	0.109±0.005
30 MeV/A C+Au				
PROTON	LITH-CARB	10.1 ±0.09	50.± 4.	0.142±0.009
DEUTERON	LITH-CARB	10.0 ±0.8	37.± 6.	0.128±0.009

Figure V-27. [(a) and (c)] Coincidence spectra moving source fit temperatures and velocities for the LP and IRF triggers and [(b) and (d)] for the PLF trigger from the reaction 30 MeV/A ^{12}C+Al. The parameters for protons (circles), and deuterons (squares) are plotted as ratios of the coincident spectrum value over the inclusive spectrum value as a function of trigger particle mass.

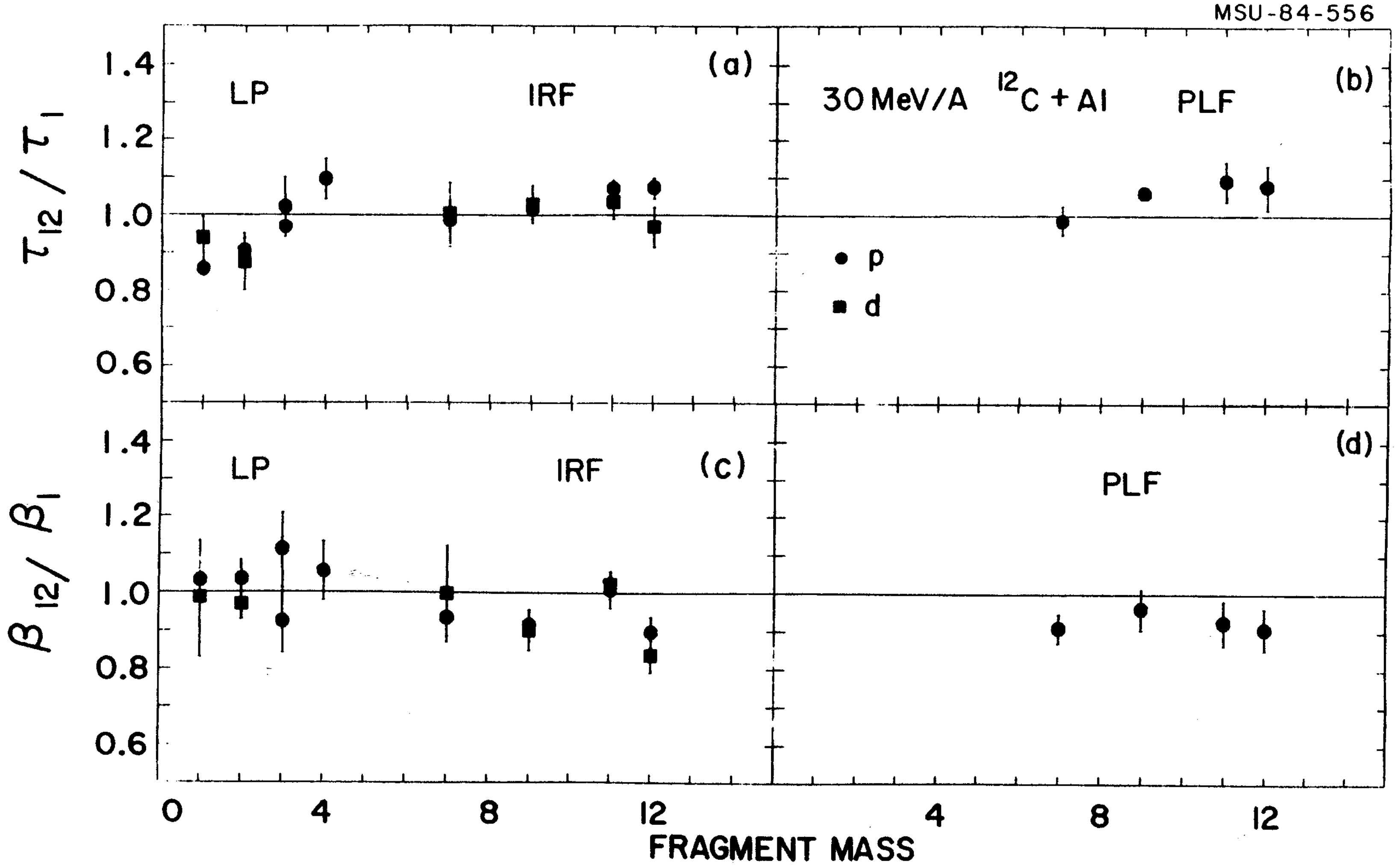
MSU-84-556
(a)
(b)
(c)
(d)
LP
IRF
PLF
30 MeV/A ^{12}C + Al
● p
■ d
τ_{12} / τ_1
β_{12} / β_1
1.4
1.2
1.0
0.8
0.6
0
4
8
12
FRAGMENT MASS

Figure V-27

The extracted moving source fit parameters are given in Table V-7. The temperatures and velocities are shown in Figures V-27;a&c as ratios to the inclusive values. The LP trigger parameters are included in the figure and will be discussed separately. The apparent source temperatures are constant and approximately 5 percent higher than the inclusive temperature, indicating that there is no dependence on the coincident fragment mass for this parameter. The apparent source velocity is also constant with coincident fragment mass and slightly lower than the inclusive velocity. The trends in these parameters are similar to those observed for the 92 MeV/A Ar+Au reaction.

2. Light Particle - PLF Coincidence Spectra

Light particle spectra for coincidences between protons at 45, 56, 71, and 90 degrees and projectile velocity fragments ($3 \leq Z \leq 6$) at -13 degrees are shown in Figure V-28.

The 45 and 56 degree spectra are nearly identical in both shape and magnitude. A comparison of the PLF triggered spectra with the IRF triggered proton spectra of Figure V-25 indicated that the 56 degree cross sections were unusually high. The moving source fits (solid lines), therefore, include the 45 degree spectra and not the 56 degree spectra.

A source size of N=27 nucleons was again adopted for the momentum conservation calculation (dot-dashed lines). The calculation gives good agreement for the Li trigger

Figure V-28. Proton coincidence energy spectra for PLF trigger fragments (a)lithium, (b)beryllium, (c)boron, and (d)carbon from the reaction 30 MeV/A ^{12}C+Al. The trigger fragment angle was -13°. The solid and dot-dashed lines are moving source fits and momentum conservation calculations, respectively, as described in the text.

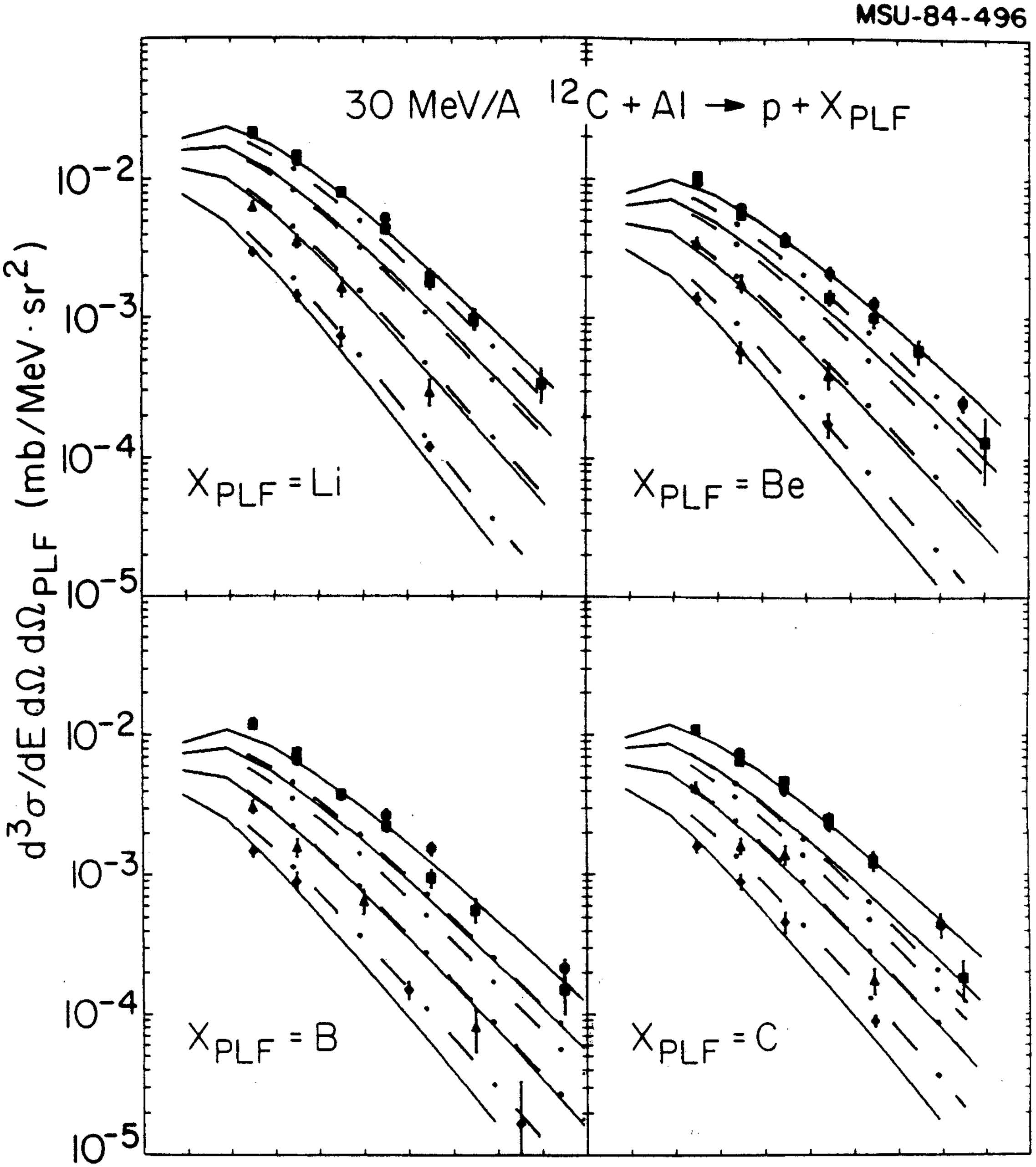
MSU-84-496
30 MeV/A ^{12}C + Al → p + X$_{PLF}$
$d^3\sigma/dE\,d\Omega\,d\Omega_{PLF}$ (mb/MeV·sr^2)
10^{-2}
10^{-3}
10^{-4}
10^{-5}
X$_{PLF}$ = Li
X$_{PLF}$ = Be
X$_{PLF}$ = B
X$_{PLF}$ = C
0
40
80
ENERGY (MeV/A)

Figure V-28

fragment but underpredicts the velocities for the heavier fragment triggers. The slopes of the spectra remain relatively constant since very little transverse momentum is imparted to the source for a fragment emitted to 13 degrees. The effect of the recoil is primarily to reduce the velocity of the source.

The extracted moving source parameters are given in Table V-8. The temperatures and velocities are plotted in Figures V-27;b&d as ratios to the inclusive values. The temperatures and velocities are constant as a function of the coincident fragment mass and reflect the same trends as the IRF parameters. No reasonable conclusion can be drawn from the moving source fits as to the origin of the apparent enhancement at 56 degrees. The data were checked for possible systematic errors which might lead to the enhancement at 56 degrees. No errors were found in the experiment itself or in the data reduction.

3. Light Particle - LP Coincidence Spectra

Light particle spectra for coincidences between protons at 45, 56, 71, and 90 degrees and light particles (p, d, t, ^{3}He, and ^{4}He) at -45 degrees in the LP trigger are shown in Figure V-29. The LP trigger spectra were integrated using the energy cuts given in section V.C.4.

A source size of N=18 nucleons was used for the momentum conservation calculation for the LP triggered spectra. The shapes of the calculated spectra are in

TABLE V-8

MOVING SOURCE PARAMETERS FOR 30 MeV/A C+Al,Au (PLF TRIGGER)

Particle	Trigger PLF	Temperature τ (MeV)	Cross section σ_0 (mb)	Velocity β (c)
30 MeV/A C+Al				
PROTON	LITHIUM	9.4±0.4	46.± 3.	0.127±0.002
	BERYLLIUM	10.1±0.1	21.± 1.	0.134±0.005
	BORON	10.4±0.5	22.± 2.	0.129±0.006
	CARBON	10.2±0.6	24.± 2.	0.126±0.006
30 MeV/A C+Au				
PROTON	LITH-BORON	9.7±0.4	94.± 8.	0.100±0.008
DEUTERON	LITH-BORON	12.4±0.7	29.± 6.	0.095±0.028

Figure V-29. Proton coincidence energy spectra for LP trigger particles (a)p, (b)d, (c)t, and (d)^{4}He from the reaction 30 MeV/A ^{12}C+Al. The trigger particle angle was -45°. The solid and dot-dashed lines are moving source fits and momentum conservation calculations, respectively, as described in the text.

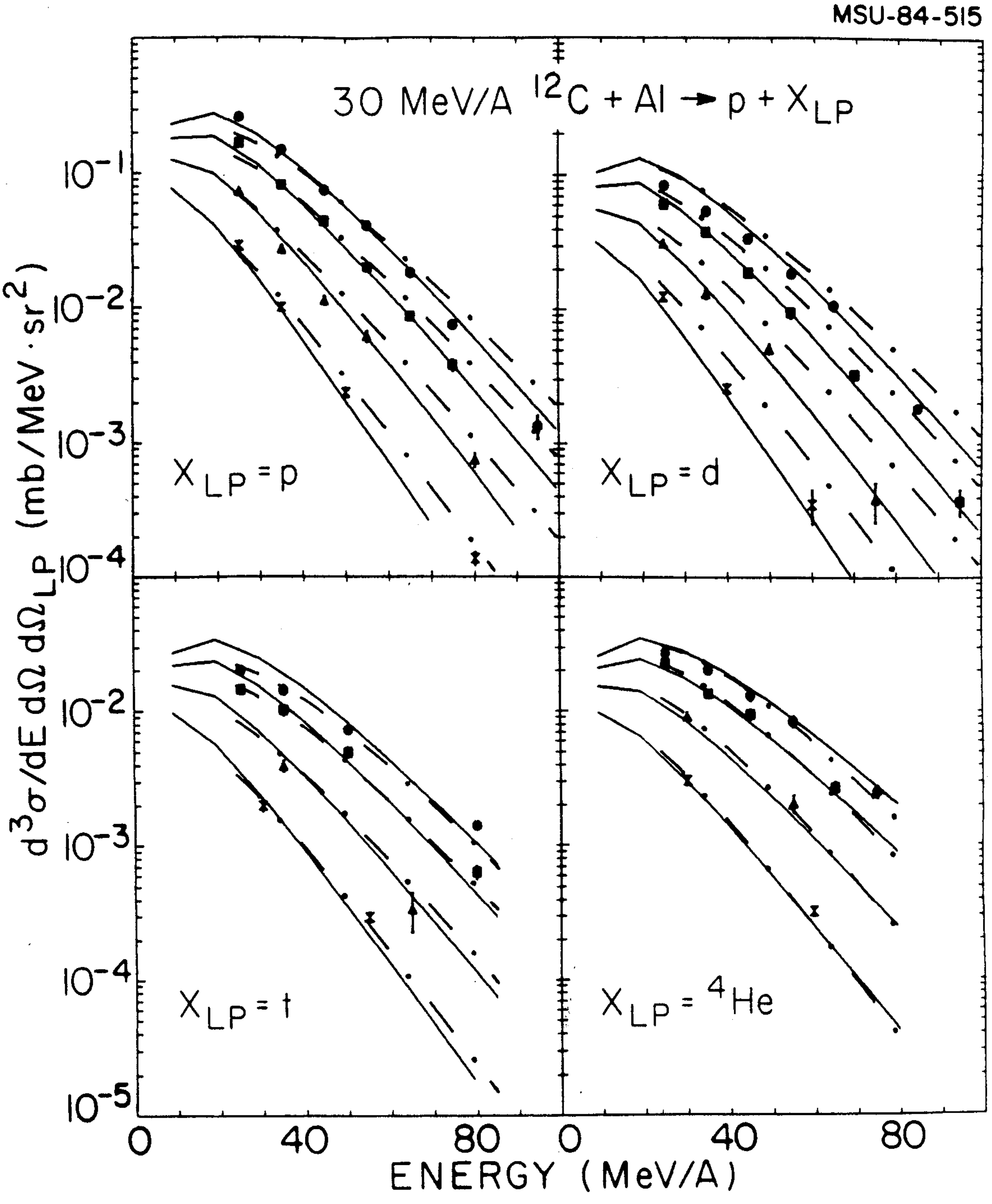
MSU-84-515
30 MeV/A ^{12}C + Al → p + X_{LP}
X_{LP} = p
X_{LP} = d
X_{LP} = t
X_{LP} = ^{4}He
$d^3\sigma/dE\,d\Omega\,d\Omega_{LP}$ (mb/MeV·sr^2)
10^{-1}
10^{-2}
10^{-3}
10^{-4}
10^{-5}
0
40
80
ENERGY (MeV/A)

Figure V-29

general agreement with the data. Little effect was seen due to the recoil momentum of the source for the light trigger particles.

The extracted moving source fit parameters are given in Table V-9. The temperatures and velocities are shown in Figures V-27;a&c along with the IRF parameters as ratios to the inclusive values. The proton temperature ratios increase smoothly with increasing coincident light particle mass from about 10 percent below the inclusive temperature for A=1 coincidences to about 10 percent above for A=4 coincidences. The ratios for A=3 and 4 are similar to those for the light particle - intermediate rapidity fragment coincidences. The velocities do not show any significant variation as a function of the coincident light particle mass and are approximately equal to the inclusive value.

E. 30 MeV/A ^{12}C+Au Coincidence Spectra

1. Light Particle - IRF Coincidence Spectra

Light particle spectra for coincidences between protons and deuterons at 47, 56, 71, and 90 degrees and intermediate rapidity fragments ($3 \leq Z \leq 6$) at -25 degrees are shown in Figures V-30;a&c. The spectra for all trigger fragments have been summed together to obtain satisfactory statistics.

The dot-dashed lines in Figure V-28 are the momentum conservation calculations based on a source size of 38

TABLE V-9

MOVING SOURCE PARAMETERS FOR 30 MeV/A C+Al (LP TRIGGER)

Particle	Trigger LP	Temperature τ (MeV)	Cross section σ_0 (mb)	Velocity β (c)
PROTON	PROTON	8.2±0.2	35.± 2.	0.144±0.002
	DEUTERON	8.6±0.3	15.± 1.	0.144±0.004
	TRITON	9.2±0.3	4.± 0.	0.155±0.012
	^{3}He	9.7±0.8	4.± 1.	0.128±0.010
	^{4}He	10.4±0.5	7.± 1.	0.147±0.009
DEUTERON	PROTON	7.9±0.5	42.± 9.	0.128±0.020
	DEUTERON	7.3±0.6	20.± 5.	0.126±0.005

Figure V-30. [(a) and (c)] Proton, deuteron coincidence energy spectra for the IRF trigger summed fragments Li, Be, B, and C at -25° from the reaction 30 MeV/A $^{12}C+Au$. [(b) and (d)] Proton, deuteron coincidence energy spectra for the PLF trigger summed fragments Li, Be, and B at -13° from the reaction 30 MeV/A $^{12}C+Au$. The solid and dot-dashed lines are moving source fits and momentum conservation calculations, respectively, as described in the text.

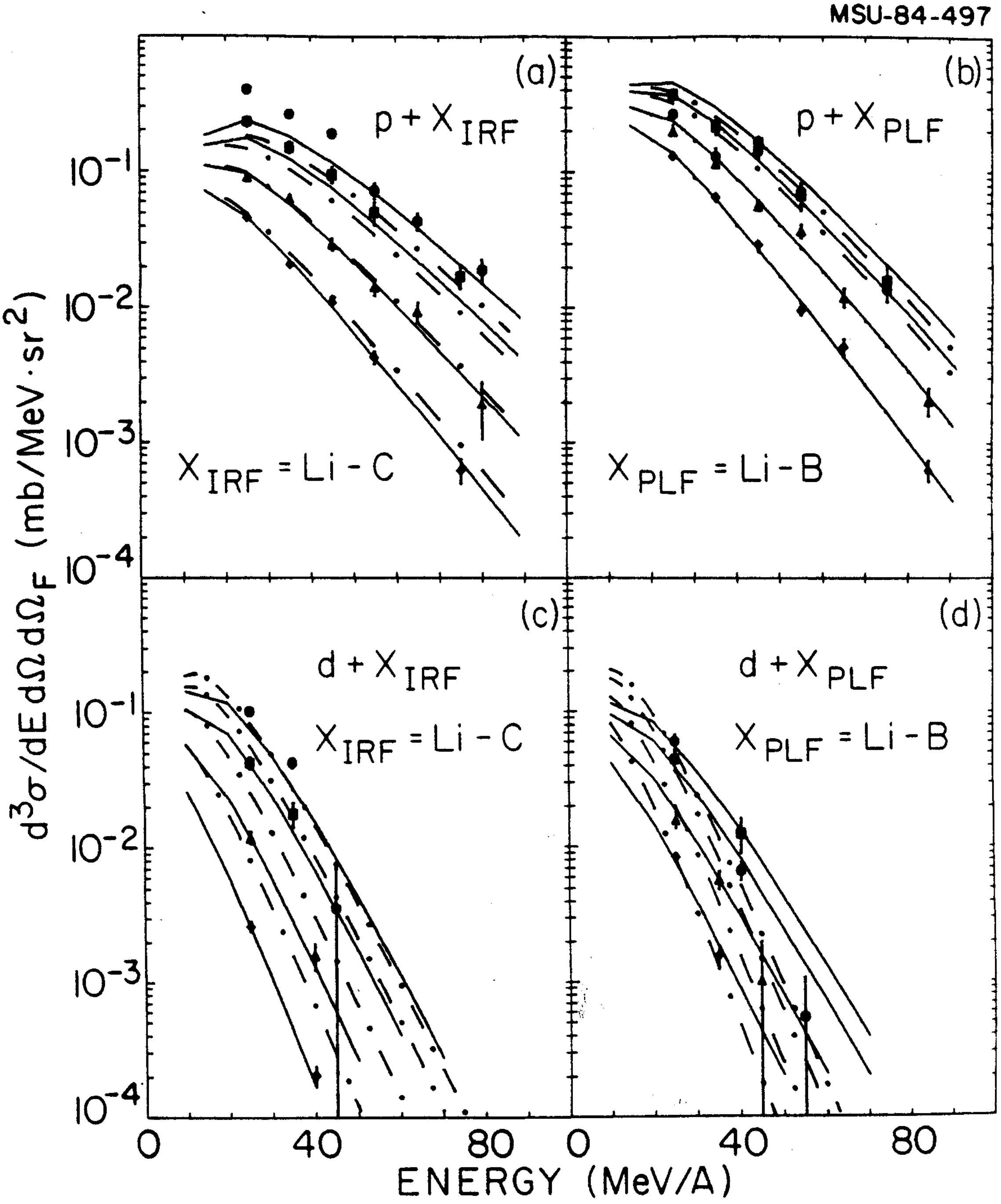
MSU-84-497
(a)
p + X_{IRF}
X_{IRF} = Li - C
(b)
p + X_{PLF}
X_{PLF} = Li - B
(c)
d + X_{IRF}
X_{IRF} = Li - C
(d)
d + X_{PLF}
X_{PLF} = Li - B
$d^3\sigma/dE\,d\Omega\,d\Omega_F$ (mb/MeV·sr^2)
10^{-1}
10^{-2}
10^{-3}
10^{-4}
0
40
80
ENERGY (MeV/A)

Figure V-30

nucleons, corresponding to a fireball at the impact parameter with the maximum weight. A fragment mass of A=10 was used for the calculation. The calculated spectra were arbitrarily normalized to the data. The agreement between the shapes of the calculated proton spectra and the data is quite good. The deuteron spectra do not have sufficient statistics to draw any firm conclusions from them.

The extracted moving source parameters are given in Table V-7. The 47 degree spectra were not included in the fits. The proton temperature is approximately 5 percent higher than for the inclusive spectra which is consistent with the Al target proton temperatures. The proton velocity is about 15 percent higher than the inclusive velocity.

2. Light Particle - PLF Coincidence Spectra

Light particle spectra for coincidences between protons and deuterons at 47, 56, 71, and 90 degrees and projectile rapidity fragments ($3 \leq Z \leq 5$) at -13 degrees are shown in Figures V-30;b&d. The spectra for all trigger fragments have been summed together to obtain satisfactory statistics. A comparison of the PLF triggered spectra with the IRF triggered spectra in the same figure shows a marked contrast in the cross sections. The PLF triggered spectra appear to be much more isotropic in the lab frame, as seen by the smaller change in cross section as a function of angle. The slopes of the spectra are similar to those of the IRF triggered spectra.

The momentum conservation calculation (dot-dashed lines) used an approximate average mass of A=9 for the trigger fragment and a source size of 38 nucleons. The calculation is in excellent agreement with the proton spectra. The predicted shape of the proton spectra is a result of the slowing down of the source due to its recoil after emission of the trigger fragment. Because of the very forward angle of emission (-13 degrees), almost all of the recoil momentum is in the direction opposite the beam direction. The moving source fits (solid lines) did not include the 47 degree spectra. The source parameters are given in Table V-8. The source temperature for the proton coincidence spectra is approximately the same as the inclusive temperature and is consistent with the Al target results. The source velocity is almost 20 percent lower than the inclusive result.

CHAPTER VI

SUMMARY

Heavy ion beams from the Lawrence Berkeley Laboratory BEVALAC and the National Superconducting Cyclotron Laboratory K500 cyclotron were used to study light particle ($Z \leq 2$) production from the reactions 92 MeV/A ^{40}Ar+Au and 30 MeV/A ^{12}C+Al,Au, respectively. Inclusive p, d, t, ^{3}He, and ^{4}He double differential cross sections were obtained and found to be in agreement with previous measurements in the intermediate energy regime. Coincidence spectra for p, d, t, ^{3}He, and ^{4}He were obtained for intermediate mass fragment triggers at forward and intermediate angles. Contributions from projectile evaporation seen in the inclusive light particle spectra were found to be diminished in coincidence spectra measured on the opposite side of the reaction plane from the trigger fragment. Light particle coincidence spectra were also measured for light particle triggers ($Z \leq 2$) on the opposite side of the reaction plane.

Double differential cross sections predicted by hydrodynamics, the firestreak model, and the coalescence model were compared to the inclusive 92 MeV/A Ar+Au data. Arbitrary normalizations were required to compare the hydrodynamics model predictions to the data. Coalescence radii and fireball model freeze-out radii were extracted from the data using the coalescence model and were found to be in agreement with radii obtained for similar systems. While neither hydrodynamics nor the firestreak model agree with the proton spectra, both models are able to describe some of the features of the other light particle spectra. The best agreement for all three models occurs for the deuteron spectra.

Triple differential, ie. reaction plane selected, cross sections predicted by hydrodynamics were compared to the p, d, t, ^{3}He, and ^{4}He coincidence spectra for the intermediate rapidity lithium fragment trigger on the opposite side of the reaction plane. The data is in disagreement with the model prediction for the $\Omega=180°$ azimuthal angle (side of the reaction plane opposite the incident projectile trajectory) as well as for the $\Omega=0°$ azimuthal angle. The data shows only small effects from the inclusion of the coincidence requirement, whereas, hydrodynamics predicts a large enhancement of the forward angle $\Omega=0°$ spectra and suppression of the forward angle $\Omega=180°$ spectra. The poor agreement is attributed to inadequate reaction plane selection for the experimental data.

The inclusive light particle spectra were fit with a single moving source parameterization. The extracted source parameters (τ-temperature, β-velocity, and σ_0-cross section) are in agreement with the systematics of previous data. The coincidence spectra were also fit with a single moving source parameterization and the extracted parameters compared to the inclusive parameters. In general, the coincidence parameters were constant and approximately the same as the inclusive values as a function of trigger fragment mass. Exceptions were noted for near projectile velocity fragment triggers at -13° from reactions with the Au target. The extracted velocities for the 92 MeV/A Ar+Au coincidence spectra showed a definite decrease as a function of increasing PLF trigger fragment mass. The decrease in the velocity parameter is associated with the apparent change in the trigger fragment reaction mechanism from intermediate velocity source emission to projectile fragmentation between carbon and oxygen. The extracted velocity for the 30 MeV/A C+Au PLF triggered proton spectra was also found to be lower than the inclusive velocity by 20 percent.

A comparison of the coincidence spectra to a conservation of momentum calculation, assuming particle emission from a single thermal moving source, showed that the effect of the source recoil momentum was small for the Ar+Au reaction. This was in part due to the large source size (N=82) used in the calculation, as obtained from the fireball model. It was possible to obtain normalizations accurate to 20 percent using moving source normalizations obtained for the inclusive spectra. For the C+Al reaction, a source size of N=27 nucleons was used instead of the fireball prediction of N=18. A larger source size was needed to reduce the effect of the source recoil momentum on the calculated light particle spectra. For the C+Au reaction, the fireball prediction of N=38 was used for the source size. The momentum conservation calculation was able to account for the lower observed moving source velocity of the light particle coincidence spectra for the near projectile velocity fragment trigger.

Overall, it was found that the measured light particle coincidence spectra could be satisfactorily explained with the assumption of sequential emission from a thermal source moving with approximately the center of mass velocity. A new cascade calculation by Kruse, et al. [Kr 84] has recently been shown to reproduce experimental data for Ar induced reactions on Ca at 42, 92, and 137 MeV/A. This calculation incorporates features found to be necessary at energies above 200 MeV/A and below 20 MeV/A such as the nuclear mean field, two-body collisions, and Pauli blocking. Extension of this model to other systems and to coincidence events may provide an entirely different understanding of the relevent reaction mechanisms than is currently possible.

One of the underlying problems associated with comparing the light particle coincidence data to the theories is the determination of the reaction plane. It would be of interest to measure light particle spectra out-of-plane and also in-plane near the trigger fragment trajectory, as well as on the opposite side of the reaction plane. The out-of-plane spectra should be greatly suppressed for events where the reaction plane is well defined, while the near fragment trajectory spectra should be greatly enhanced. A projectile-like fragment trigger would be likely to give the best reaction plane selection due to the larger impact parameters associated with projectile fragmentation. The current ultimate goal in heavy ion physics at NSCL is full event reconstruction, ie. detection of all charged particles created in an event using a 4π array.

APPENDIX

APPENDIX A

MOMENTUM CONSERVATION MODEL

The momentum conservation calculation discussed in Chapter V.B.1 is based on a treatment by Lynch, et al. [Ly 82]. The calculation assumes that particles are emitted isotropically, ie. with equal probability at all angles, in the rest frame of a moving thermal source with A nucleons. The energy distribution is also assumed to be isotropic in the source rest frame, ie. the energy spectra are the same at all angles and are given by the relativistic Maxwell-Boltzmann distribution. The source rest frame differential cross section is then given by

$$\frac{d^2\sigma}{p^2 dp d\Omega} = \frac{\sigma_0}{4\pi m^3} \frac{e^{-E/\tau}}{2(\tau/m)^2 K_1(m/\tau)+(\tau/m)K_0(m/\tau)}, \qquad (A-1)$$

where σ_0 is a normalization constant (treated as the total integrated cross section), m is the mass of the emitted particle, τ is the temperature of the source (related to the excitation energy), and p and E are the momentum and total energy, respectively, of the emitted particle in the source rest frame. K_0 and K_1 are MacDonald functions, also known as modified Bessel functions of the second kind [Ab 72]. The emission of a particle of lab momentum $p_{1_{lab}}$ and mass m_1 ($m_1=A_1m_0$, where m_0=931.5 MeV) at an angle $\theta_{1_{lab}}$ changes the values of both the temperature and the momentum of the remaining ensemble. The Lorentz transformations to the source rest frame for an initial laboratory source velocity β are given by

$$p_{1xs}=\gamma(p_{1lab}\cos\theta_{1lab}-\beta E_{1lab}/c) \ , \qquad \text{(A-2)}$$

$$p_{1ys}=p_{1ylab}=p_{1lab}\sin\theta_{1lab} \ , \qquad \text{(A-3)}$$

$$E_{1s}=\gamma(E_{1lab}-p_{1lab}\cos\theta_{1lab}\beta c) \ , \qquad \text{(A-4)}$$

where

$$\gamma=(1-\beta^2)^{-1/2}, \qquad \text{(A-5)}$$

the x (y) subscript denotes the parallel (transverse) component of the particle momentum, and the s subscript denotes the moving source frame.

The cross section in the moving frame is then given by

$$\frac{d^2\sigma_1}{p_{1s}^2 dp_{1s} d\Omega_{1s}} = \frac{\sigma_{01}}{4\pi m_1{}^3} \ \frac{e^{-E_{1s}/\tau}}{\kappa(m_1/\tau)} \ , \qquad \text{(A-6)}$$

where

$$\kappa(m_1/\tau)=2(\tau/m_1)^2K_1(m_1/\tau)+(\tau/m_1)K_0(m_1/\tau). \qquad \text{(A-7)}$$

The cross section is transformed to the laboratory frame as

$$\frac{d^2\sigma_{1lab}}{dE_{1lab}d\Omega_{1lab}} = \frac{p_{1lab}E_{1s}\sigma_0}{4\pi m_1{}^3} \ \frac{e^{-E_{1s}/\tau}}{\kappa(m_1/\tau)} \qquad \text{(A-8)}$$

The new laboratory source velocity parallel to the initial direction is given by

$$\beta_x' = \frac{\beta-p_{1xs}/m_0A}{1-\beta p_{1xs}/m_0A'}, \qquad \text{(A-9)}$$

and perpendicular to the initial direction by

$$\beta_y' = -p_{1ys}/m_0A', \qquad \text{(A-10)}$$

where $A'=A-m_1/m_0$. The energies E_x and E'_x of the original and residual sources are related by

$$E'_x = E_x-(E_{1s}-m_1)-(p_{1s})^2/2m_0A', \qquad (A-11)$$

where

$$p_{1s}^2 = p_{1xs}^2 + p_{1ys}^2. \qquad (A-12)$$

The last term in Eqn. A-11 accounts for the recoil energy of the residual source. Using the empirical relation between excitation energy and temperature

$$E_x = A\tau^2/(8\ \mathrm{MeV}), \qquad (A-13)$$

gives the temperature parameter of the recoiling source as

$$\tau' = (E'_x{*}8\ \mathrm{MeV}/A')^{1/2}. \qquad (A-14)$$

The emission of a second particle of lab momentum p_{2lab} and mass m_2 at an angle θ_{2lab} has Lorentz transformations to the residual source rest frame given by

$$p_{2xs}=\gamma'(p_{2lab}\cos\theta_{2lab}-\beta'_xE_{2lab}/c)\ , \qquad (A-15)$$

$$p_{2ys}=p_{2ylab}-m_2\beta'_yc = p_{2lab}\sin\theta_{2lab}-m_2\beta'_y \qquad (A-16)$$

$$E_{2s}= c\surd(p_{2xs}^2 + p_{2ys}^2 + m_0^2c^4). \qquad (A-17)$$

The source rest frame cross section for emission of the second particle is then given by

$$\frac{d^2\sigma_2}{p_{2s}^2dp_{2s}d\Omega_{2s}} = \frac{\sigma_{02}}{4\pi m_2^3}\ \frac{e^{-E_2/\tau'}}{\kappa(m_2/\tau')}\ , \qquad (A-18)$$

which transforms to the laboratory frame as

$$\frac{d^2\sigma_{2lab}}{dE_{2lab}d\Omega_{2lab}} = \frac{p_{2lab}E_{2s}\sigma_0}{4\pi m_2^3}\ \frac{e^{-E_{2s}/\tau'}}{\kappa(m_2/\tau')}. \qquad (A-19)$$

The coincidence cross section for the emission of particle 1 of momentum $\mathbf{p}_1$ followed by the emission of particle 2 of momentum $\mathbf{p}_2$ is then proportional to the product

$$P(\mathbf{p}_1,\mathbf{p}_2)=\frac{d^2\sigma_{1lab}(\mathbf{p}_1,\beta,\tau,m_1)}{dE_{1lab}\;d\Omega_{1lab}} \times \frac{d^2\sigma_{2lab}(\mathbf{p}_2,\beta',\tau',m_2)}{dE_{2lab}\;d\Omega_{2lab}}. \qquad \text{(A-20)}$$

Since we cannot distinguish the reverse time sequence experimentally, we also have

$$P(\mathbf{p}_2,\mathbf{p}_1)=\frac{d^2\sigma_{2lab}(\mathbf{p}_2,\beta,\tau,m_2)}{dE_{2lab}\;d\Omega_{2lab}} \times \frac{d^2\sigma_{1lab}(\mathbf{p}_1,\beta'',\tau'',m_1)}{dE_{1lab}\;d\Omega_{1lab}}. \qquad \text{(V-21)}$$

The parameters β'',τ'' are defined in the same manner as eqs. (A-9) through (A-14). The cross section for the emission of particles 1 and 2 is now given by

$$\frac{d^4\sigma}{dE_1 d\Omega_1 dE_2 d\Omega_2} = C_0[P(\mathbf{p}_1,\mathbf{p}_2)+P(\mathbf{p}_2,\mathbf{p}_1)], \qquad \text{(A-22)}$$

where C_0 is a normalization constant taken to be equal to

$$C_0 = 1/\sqrt{2}\ \sigma_R, \qquad \text{(A-23)}$$

with σ_R equal to the total reaction cross section. The factor $1\sqrt{2}$ is takes into account the normalization for the two possible time sequences.

In order to compare the calculation to the experimental spectra, the differential cross section of eqn. (A-22) is integrated numerically over dE_1, ie. particle 1 is defined as the coincidence trigger. A step size of $\Delta E_1=5$ MeV was used for the integration. The initial values of β and τ are the moving source fit parameters obtained for the singles spectra of particle 2. The values of σ_{01} and σ_{02}

are the total cross sections obtained with moving source fits to the singles spectra of particles 1 and 2. Since the parameters reflect a negative coulomb shift as a result of the data fitting procedure, a positive coulomb energy shift is applied to the calculated coincidence spectra. Figure A-1;a shows the results of the calculation for a trigger particle of mass $m_1=10m_0$ emitted at -45° in the laboratory frame. The mass of particle 2 is $m_2=1m_0$, ie. a proton, with the spectra shown for angles from +10° to +90° (solid lines) and -10° to -90° (dotted lines) in 20° steps. The source size is A=30 nucleons. The other parameters are as follows:

$\sigma_{01}=\sigma_{02}=20000.$ mb

$\beta=0.20$ c

$\tau=20$ MeV

Lower limit for integration of particle 1=100 MeV

Upper limit for integration of particle 1=500 MeV

Coulomb shift = 10 MeV

It can be seen from Figure A-1;a that the spectra for emission of particle 2 on the same side as the trigger particle are suppressed relative to the spectra for emission on the opposite side. The suppression/enhancement is a direct result of the recoil velocity of the source in the direction opposite the trigger particle. The difference in the spectra for opposite sides is quite striking for the source size of A=30. Figure A-1;b shows the same calculation done for a source size of A=82 nucleons. All of the other parameters are the same. The difference in the

Figure A-1. Sample conservation of momentum model calculations for source sizes of (a) A=30 and (b) A=82. The trigger particle angle is -45 degrees. The spectra are shown for angles from +10° to +90° (solid lines) and -10° to -90° (dotted lines) in 20° steps.

MSU-84-528

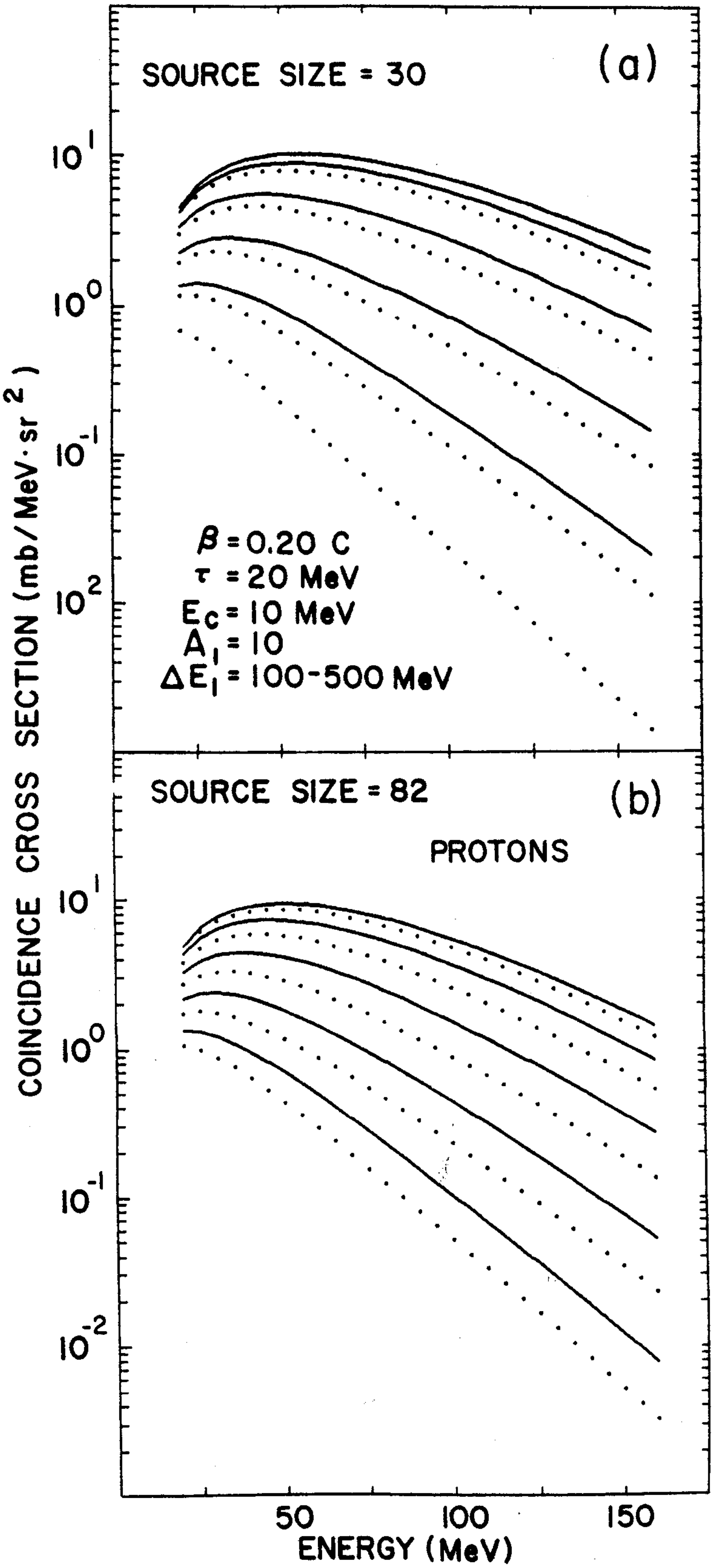

Figure A-1

spectra for opposite sides is now much less, reflecting the slower recoil velocity of the heavier source. If one can reasonably apply the concept of a distinct moving thermal source to a given type of reaction, then this calculation is a useful tool for the identification of significant differences in coincidence spectra.

REFERENCES

REFERENCES

A

[Ab 72] M. Abramowitz and I. A. Stegun, *Handbook of Mathematical Functions*, Dover Publications, Inc. (1972)p.374.

[Ab 83] R. L. Auble, J. B. Ball, F. E. Bertrand, C. B. Fulmer, D. C. Hensley, I. Y. Lee, R. L. Robinson, P. H. Stelson, C. Y. Wong, D. L. Hendrie, H. D. Holmgren, and J. D. Silk, Phys. Rev. C**28**(1983)1552.

[Aj 75] Ajzenberg-Selove, Nucl. Phys. A**248**(1975)1.

[Au 83] R. Au, R. Fox, D. Notman, and B. Sherrill, MSU Cyclotron Annual Report, 1982-1983, p.87

[Aw 80] T. C. Awes, C. K. Gelbke, G. Poggi, B. B. Back, B. Glagola, H. Breuer, V. E. Viola, Jr., and T. J. M. Symons, Phys. Rev. Lett. **45**(1980)513.

[Aw 81] T. C. Awes, G. Poggi, C. K. Gelbke, B. B. Back, B. G. Glagola, H. Breuer, and V. E. Viola, Jr., Phys. Rev. C**24**(1981)89.

B

[Ba 82] A. Baden, H. H. Gutbrod, H. Löhner, M. R. Maier, A. M. Poskanzer, T. Renner, H. Riedesel, H. G. Ritter, H. Spieler, A. Warwick, F. Weik and H. Wieman, Nucl. Instr. and Meth. **203**(1982)189.

[Bc 84] G. Buchwald, G. Graebner, J. Theis, J. Maruhn, W. Greiner, and H. Stöcker, Phys. Rev. Lett. **18**(1984)1594.

[Be 79] Bevatron/Bevalac User's Guide, Lawrence Berkeley Laboratory, Berkeley, CA 1979

[Bi 67] J B. Birks, *Theory and Practice of Scintillation Counting* (Pergamon Press, London 1967)p.100

[Bi 80] Brookhaven Instruments Corporation, Model 1000 Current Integrator, Austin, TX, 1980

[Bo 83] V. Borrel, D. Guerreau, J. Galin, B. Gatty, D. Jacquet, and X. Tarrago, Z. Phys. A**314**(1983)191.

[Bo 84] D. H. Boal, MSU Preprint MSUCL-451 (1984).

[Br 83] B. Borderie, M. F. Rivet, I. Forest, J. Galin, D. Guerreau, R. Bimbot, D. Gardès, B. Gatty, M. Lefort, H. Oeschler, S. Song, B. Tamain, and X. Tarrago, Nucl. Phys. A402(1983)57.

[Bu 80] G. Buchwald, L. P. Csernai, J. A. Maruhn, W. Greiner, and H. Stöcker, Phys. Rev. C24(1981)135.

[Bu 84] G. Buchwald, private communication

C

[Ch 70] Charpak, Ann. Rev. Nucl. Sci. 20(1970)195

[Cu 81] J. Cugnon, T. Mizutani and J. Vandermeulen, Nucl. Phys. A352(1981)505.

[Cu82] J. Cugnon, Nucl.Phys. A387(1982)102c.

E

[Em 79] EMI Gencom, Inc., Plainview, New York

F

[Fi 84] D. J. Fields, W. G. Lynch, C. B. Chitwood, C. K. Gelbke, M. B. Tsang, H. Utsunomiya, and J. Aichelin, MSU Cyclotron Laboratory Preprint MSUCL 471, (1984).

G

[Gi 84] D. Guinet, R. Billerey, C. Cerruti, S. Chiodelli, and A. Demeyer, Phys. Lett. 137B(1984)318.

[Go 60] T. J. Gooding and H. G. Pugh, Nucl. Instr. and Meth. 7(1960)189.

[Go 74] A. S. Goldhaber, Phys. Lett. 53B(1974)306.

[Go 77] J. Gosset, H. H. Gutbrod, W. G. Meyer, A. M. Poskanzer, A. Sandoval, R. Stock, and G. D. Westfall, Phys. Rev. C16(1977)629.

[Go 78] J. Gosset, J. I. Kapusta, and G. D. Westfall, Phys. Rev. C18(1978)844.

[Gu 76] H. H. Gutbrod, A. Sandoval, P. J. Johansen, A. M. Poskanzer, J. Gosset, W. G. Meyer, G. D. Westfall, and R. Stock, Phys. Rev. Lett. 37(1976)667.

[Gu 84] H. A. Gustafsson, H. H. Gutbrod, B. Kolb, H. Löhner, B. Ludewigt, A. M. Poskanzer, T. Renner, H. Riedesel, H. G. Ritter, A. Warwick, F. Weik, and H. Wieman, LBL Preprint LBL-17678, (1984) and Phys. Rev. Lett. 18 (1984)1590.

H

[Ha 80] Harshaw Chemical Company, Solon, Ohio, Datasheet (1980)

[Ha 82] B. E. Hasselquist, G. M. Crawley, R. S. Tickle, L. Richardson, and G. D. Westfall, MSU Cyclotron Annual Report 1981-1982, p.78

[Ha 83] B. E. Hasselquist, G. D. Westfall, L. H. Harwood, R. S. Tickle, B. V. Jacak, Z. M. Koenig, G. M. Crawley, T. J. M. Symons, and J. P. Dufour, MSU Cyclotron Annual Report 1982-1983, p.7

[Hi 77] R. D. Hiebert, H. A. Thiesssen, and A. W. Obst, Nucl. Instr. and Meth., 142(1977)467.

J

[Ja 66] J. F. Janni, Kirtland Air Force Base Technical Report AFWL-TR-65-150(1966)

[Ja 81] B. Jakobsson, L. Carlen, P. Kristiansson, J. Krumlinde, A. Oskarsson, I. Otterlund, B. Schrøder, H.-A. Gustafsson, T. Johansson, H. Ryde, G. Tibell, J. P. Bondorf, G. Fài, A. O. T. Karvinen, PO. B. Nielsen, M. Buenern, J. Cole, D. Lebrun, J. M. Loiseaux, P. Martin, R. Ost, P. de Saintignon, C. Guet, E. Monnand, J. Mougey, H. Nifenecker, P. Perrin, J. Pinston, C. Ristori, and F. Schussler, Phys. Lett. 102B(1981)121.

[Ja 83] B. V. Jacak, G. D. Westfall, C. K. Gelbke, L. H. Harwood, W. G. Lynch, D. K. Scott, H. Stöcker, M. B. Tsang, and T. J. M. Symons, Phys. Rev. Lett. 51(1983)1846.

[Ja 84] B. V. Jacak, private communication.

[Jc 84] B. V. Jacak, to be published.

K

[Ke 76] C. R. Kearns,IEEE Trans. on Nucl. Sci., Vol. NS-24 (1977)353.

[Ki 84] Y. Kitazoe, M. Sano, Y. Yamamura, H. Furutani, and K. Yamamoto, Phys. Rev. C 29(1984)828.

[Kl 79] H. Klein and H. Schölermann, IEEE Trans. on Nucl. Sci., Vol. NS-26 (1979)373.

[Kr 84] H. Kruse, B. V. Jacak, H. Stöcker, and G. D. Westfall, MSU Cyclotron Laboratory preprint MSUCL-478 (1984).

L

[La 69] L. D. Landau and E. M. Lifshitz, Statistical Physics (Addison-Wesley, New York, 1969), p. 109.

[Le 79] M. C. Lemaire, S. Nagamiya, S. Schnetzer, H. Steiner, and I. Tanihata, Phys. Lett. 85B(1979)38.

[Le 81] LeCroy Research Systems Corporation, Spring Valley, New York, PCOS III Technical Manual (1981)

[Ly 82] W. G. Lynch, L. W. Richardson, M. B. Tsang, R. E. Ellis, C. K. Gelbke, and R. E. Warner, Phys. Lett. 108B(1982)274.

[Ly 83] W. G. Lynch, C. B. Chitwood, M. B. Tsang, D. J. Fields, D. R. Klesch, C. K. Gelbke, G. R. Young, T. C. Awes, R. L. Ferguson, F. E. Obenshain, F. Plasil, R. L. Robinson, and A. D. Panagiotou, MSU Preprint MSUCL-#432 (1983)

M

[Ma 68] M. Q. Makino, C. N. Waddell and R. M. Eisberg, Nucl. Instr. and Meth. 60(1968)109.

[Ma 80] M. R. Maier, H. G. Ritter, and H. H. Gutbrod, IEEE Transactions on Nuclear Science, Vol. NS-27, 42 (1980).

[Me 69] D. F. Measday and C. Richard-Serre, Nucl. Instr. and Meth. 76(1969)45.

[Me 80] W. G. Meyer, H. H. Gutbrod, Ch. Lukner, and A. Sandoval, Phys. Rev. C 22(1980)179.

[Mo 81] J. Mougey, R. Ost, M. Buenerd, J. Cole, C. Guet, D. Lebrun, J. M. Loiseaux, P. Martin, M. Maurel, E. Monnand, H. Nifenecker, P. Perrin, J. Pinston, C. Ristori, P. de Saintignon, F. Schussler, L. Carlen, B. Jakobsson, A. Oskarsson, I. Otterlund, B. Schrøder, H.-A. Gustafsson, T. Johansson, H. Ryde, J. P. Bondorf, O. B. Nielsen, and G. Tybell, Phys. Lett. 105B(1981)25.

[My 78] W. D. Myers, Nucl. Phys. A296(1978)177.

N

[Ns 81] NSCL User's Manual, Cyclotron Lab, Michigan State University, East Lansing, MI, 1981

[Nu 80] Nuclear Enterprises, Inc., San Carlos, CA Datasheet (1980)

P

[Pa 84] Particle Data Group, Rev. Mod. Phys. 56(1984)S51

R

[Ra 83] F. Rami, J. P. Coffin, G. Guillaume, B. Heusch, P. Wagner, A. Fahli, and P. Fintz, report CRN/PN.8407 (1984).

S

[Sa 81] H. Sato and K. Yazaki, Phys. Lett. 95B(1981)153.

[Sc 79] D. K. Scott, LBL Preprint LBL-8931 (1979).

[Sc 80] H. Schölermann and H. Klein, Nucl. Instr. and Meth., 169(1980)25.

[Sc 81] D. K. Scott, Nucl. Phys. A354(1981)375c and MSU Preprint MSUCL-359 (1981).

[So 81] H. Stöcker, R. Y Cusson, J. A. Maruhn, and W. Greiner, Phys. Lett. 101B(1981)379 and Z. Phys. A294(1980)125.

[St 68] J. D. Stevenson, Phys. Rev. Lett. 41(1968)1702.

[St 79] H. Stöcker, J. A. Maruhn, and W. Greiner, Z. Phys. A293(1979)173.

[St 80] H. Stöcker, J. A. Maruhn, and W. Greiner, Phys. Rev. Lett. 44 (1980)725.

[St 81] H. Stöcker, M. Gyulassy, and J. Boguta, LBL Preprint LBL-12095 (1981)

[St 82] H. Stöcker, C. Riedel, Y. Yariv, L. P. Csernai, g. Buchwald, G. Graebner, J. A. Maruhn, W. Greiner, K. Frankel, M. Gyulassy, B. Schurmann, G. Westfall, J. D. Stevenson, J. R. Nix, and D. Strottman, LBL Preprint LBL-12634 (1982)

[St 83] H. Stocker, G. Buchwald, G. Graebner, P. Subramanian, J. A. Maruhn, W. Greiner, B. V. Jacak, and G. D. Westfall, Nucl. Phys. A400(1983)63.

T

[Ti 81] R. S. Tickle, G. M. Crawley, W. G. Lynch, M. B. Tsang, and J. Yurkon, MSU Cyclotron Annual Report 1980-1981, p.86

[Ti 82] R. S. Tickle, B. E. Hasselquist, G. M. Crawley, and J. Yurkon, MSU Cyclotron Annual Report 1981-1982, p.77

[Ts 74] Y. S. Tsai, Rev. Mod. Phys. 46(1974)815.

V

[Va 79] K. Van Bibber, D. L. Hendrie, D. K. Scott, H. H. Weiman, L. S. Schroeder, J. V. Geaga, S. A. Cessin, R. Treuhaft, Y. J. Grossiord, J. O. Rasmussen, and C. Y. Wong, Phys. Rev. Lett. 43(1979)840.

[Vi 79] Y. P. Viyogi, T. J. M. Symons, P. Doll, D. E. Greiner, H. H. Heckman, D. L. Hendrie, P. J. Lindstrom, J. Mahoney, D. K. Scott, K. Van Bibber, G. D. Westfall, H. Wieman, H. J. Crawford, C. McParland, C. K. Gelbke, Phys. Rev. Lett. 42(1979)33.

W

[Wa 83] A. I. Warwick, H. H. Wieman, H. H. Gutbrod, M. R. Maier, J. Peter, H. G. Ritter, H. Stelzer, F. Weik, M. Freedman, D. J. Henderson, S. B. Kaufman, E. P. Steinberg, and B. D. Wilkins, Phys. Rev. C27(1983)1083.

[We 76] G. D. Westfall, J. Gosset, P. J. Johansen, A. M. Poskanzer, W. G. Meyer, H. H. Gutbrod, A. Sandoval, and R. Stock, Phys. Rev. Lett. 37(1976)1202.

[We 82] G. D. Westfall, B. V. Jacak, N. Anantaraman, M. W. Curtin, G. M. Crawley, C. K. Gelbke, B. Hasselquist, W. G. Lynch, D. K. Scott, B. M. Tsang, M. J. Murphy, T. J. M. Symons, R. Legrain, T. J. Majors, Phys. Lett. 116B(1982)118.

[We 84] G. D. Westfall, Z. M. Koenig, B. V. Jacak. L. H. Harwood, G. M. Crawley, M. W. Curtin, C. K. Gelbke, B. Hasselquist, W. G. Lynch, A. D. Panagiotou, D. K. Scott, H. Stöcker, and M. B. Tsang, Phys. Rev. C <u>29</u>(1984)861.

[Ws 84] G. D. Westfall, private communication.

Y

[Ya 79] Y. Yariv and Z. Fraenkel, Phys. Rev. C<u>20</u>(1979)2227.